A

Dissertation

Entitled

Photodegradation of Methylene Blue dye by porous Manganese dioxide (MnO_2)

Submitted in partial fulfillment of the requirement for the award of the

degree of

MASTER OF SCIENCE
in
Physics

under the supervision of

Dr. O.P. Pandey
(Senior Professor)

THAPAR INSTITUTE
OF ENGINEERING & TECHNOLOGY
(Deemed to be University)

submitted by
Kajal
(301704015)

School of Physics & Materials Science

Thapar Institute of Engineering and Technology (TIET),
Patiala – 147004

June, 2019

CERTIFICATE

This is to certify that this dissertation entitled **'Photodegradation of Methylene Blue dye by porous Manganese dioxide (MnO_2)'** is submitted by **Ms. Kajal (301704015)** in fulfilment of requirement for the award of degree of Master of Science in Physics from School of Physics and Materials Science, Thapar Institute of Engineering and Technology, Patiala, India. It is an exclusive record of candidate's own research work under the supervision of Dr. O. P. Pandey. The dissertation in part or in full has not been submitted in any other university or institute for the award of any degree.

Dr. O. P. Pandey
(Supervisor)
Senior Professor
School of Physics and Materials Science,
Thapar Institute of Engineering and Technology, Patiala

DECLARATION

I hereby declare that the work been presented in this thesis report entitled **'Photodegradation of Methylene Blue dye by porous Manganese dioxide (MnO_2)'** by me in partial fulfilment of the requirements for the award of degree of Masters of Science in Physics, Thapar Institute of Engineering and Technology, Patiala is an authentic award record on my work carried out under the supervision of Dr. O. P. Pandey (Senior Professor), School of Physics and Materials Science, Thapar Institute of Engineering and Technology, Patiala. The work presented here has not been submitted for any degree or examination in any other university/institute, and that all the sources that I have used or quoted have been indicated and acknowledged by complete references.

Kajal
(301704015)

ACKNOWLEDGEMENT

First and foremost, I would like to express my gratitude to my M.Sc. dissertation thesis supervisor **Dr. O. P. Pandey** (Senior Professor & Head, School of Physics and Materials Science); who has an attitude and substance of a genius; who has continually and convincingly conveyed a spirit of adventure in regard to research. I would also like to thank him for his useful comments, remarks, motivation and constant support provided throughout this course work.

It is my privilege to express my heartiest gratitude to **Prof. Prakash Gopalan**, Director, Thapar Institute of Engineering and Technology, Patiala, for providing the resources for my research work. My deepest gratitude to **Mr. Aayush Gupta** for guiding and embarking on this journey with me and staying with me till the end. In my difficult times during the duration of this course work, he is the one who helped to surmount the problems with such ease. Without his guidance and persistent help, this project would not have been possible. I am thankful for his valuable engagement and encouragement. A warm thanks to my lab mates who have supported me through thick and thin **Mr. Rameez Ahmad Mir**, **Mr. Piyush Sharma**, **Ms. Ruby Priya**, **Ms. Damandeep Kaur**, **Ms. Gurwinder Kaur**, **Ms. Shweta Chalotra** and **Ms. Ishita Khurana**; thank you for your guidance, friendliness and encouragement.

Greatest appreciation goes to my parents, **Mr. Baljeet Singh** and **Mrs. Santosh** for their unconditional love and their support throughout my life. Not forgetting my siblings and all members of my extended family, without their blessings I wouldn't have completed this project.

This acknowledgment is incomplete without thanking the people, I was around during this particular period of time, for hearing me out and keeping me harmonious. And above all I express my indebtness to the almighty for all his blessings.

Kajal

ABSTRACT

The fast advancement of industry has led to many ecological, environmental, social and biological problems. In order to resolve some of these problems, it is necessary to find suitable highly efficient techniques to resolve them. One of them is the waste water treatment and removing harmful the organic pollutants to make them reusable. Semiconductor nanomaterials are used as photocatalyst due to their potential application for degradation of harmful organic pollutants. Mn-oxides catalysts has been found to be highly effective for the adsorption and photocatalytic degradation of many organic dyes due to their high surface area and multiple oxidation states. In this work, the MnO_2 nanopowder has been synthesized through sonochemical route using $KMnO_4$ and poly-ethylene glycol as the reducing agent. Structural and optical analysis (XRD, TEM, FTIR, BET and UV–visible) confirmed the formation of nanocrystalline MnO_2 network. The adsorption and photocatalytic performance of synthesized MnO_2 was tested for degradation of methylene blue dye and p nitrophenol (2.0 mg/L) under dark chamber and household CFL lamp exposure, respectively. Further, the adsorption and degradation of methylene blue dye has been studied with varying concentration (3.0, 4.0, 5.0, 6.0, 7.0, 8.0, 9.0, 10.0 mg/L) and also at different pH values (2.0, 5.0, 7.0, 10.0 mg/L at 2.0 and 10.0 pH) of the dye solution.

Table of Contents

List of Figures **Page**

List of Tables **Page**

Chapter 1

Chapter 4

List of Publications:

1. K. Rajrana, Aayush Gupta, R.A. Mir and O.P. Pandey, Facile sono-chemical synthesis of nanocrystalline MnO2 for catalytic and capacitive applications, Physica B: Condensed Matter (2019). DOI: 10.1016/j.physb.2019.04.002

1. Introduction

Water, which is indispensable in every life has become a matter of concern in modern times. Mark Twain said **"Whisky is to drink, Water is to fight"** which seems to become realistic within few years. The polluters cannot release the waste water containing contaminants in natural water resources. Water is being contaminated by variety of waste such as agricultural waste, discharge of harmful chemicals from pharmaceutical industries and organic pollutants like dyes, phenols from textile industries. These organic pollutants and chemicals are stable in ambient condition and act as a seed to many ecological problems for example indirect greenhouse effect, acid rain etc. [1]. The most common water pollutants are the dyes which have various applications in different types of industries like paper, leather, cosmetics, drugs, electronics, plastics and printing and textile industries consumed approximately 80% of the synthetic dyes. These synthetic organic dyes are the major cause of water pollution which makes very serious environmental issues due to its high aromaticity, toxicity, chemical stability, large-scale production, carcinogenic in nature and low biodegradability. This is becoming a vital threat to both aquatic and human lives.

1.1. Need for wastewater treatment

According to the recent survey due to the industrial revolution, the contamination of water due to toxic organic compounds has increased. Considering the requirement of fresh water which is depleting these days, there is need to purify the contaminated water. Although many physical and chemical processes such as adsorption, precipitation, ultra-filtration, flocculation, anaerobic treatment, fenton's reagent and reverse osmosis are being applied to treat the contaminated water by removing the toxic organic substances [2–5]. But these treatments result in the amendment of other toxic byproduct which are also non-self-degradable in ambient conditions and also these conventional methods are not economic, difficult to handle and non-destructive [6]. Each of these methods have many disadvantages such as specific treatment condition requirement of specific designed tool etc. However, photocatalytic degradation is becoming the center of focus for the wastewater treatment due to its low cost, reusability and high efficiency of the catalyst [7]. It is capable of degrading vast number of organic effluents by converting into harmless substance. For the decomposition of organic effluents, metal-oxide nanoparticles exhibit magnificent photocatalytic activity. This chapter includes a brief discussion about photocatalytic process and need for selecting MnO_2 to study its photocatalytic activity over other catalyst.

1.2. Photocatalysis

Prior to understand photocatalysis, it is necessary to describe catalysis under which the chemical reaction rate gets modified due to the presence of an additional substance known as catalyst and these substances are not consumed in that reaction. Commonly, the presence of the catalyst enhances the rate of chemical reaction by providing additional reaction platform with alternate pathway at lower activation energy [8]. Based on the phase of catalyst and reactants, catalysis can be categorized into two basic categories such as 1) homogenous and 2) heterogeneous catalysis.

Broadly, the definition of the photocatalysis - the change in the chemical reaction rate by the action of electromagnetic radiation under the presence of substances which absorb light (called photocatalyst) that is also involved in chemical transformation of the reactants [9]. In photocatalysis, photon facilitates the generation of reactive radicals that produces non-toxic byproducts as a result of chemical reaction between radicals and effluent [10]. Depending upon the necessity of the chemical reactions, variety of compounds (metals, insulators and semiconductors) can be used as photocatalyst. Mostly, semiconductors are preferred much as catalyst due to its performance as sensitizer for light irradiation. [9]. So, in comparison with homogeneous photocatalysis, heterogeneous photocatalysis is preferred due to the easy extraction of catalyst from the reaction mixture [11].

1.3. Mechanism

When semi conducting compound is exposed to light (photons) having energy equivalent or more than the energy gap of the semiconducting compounds due to which the electrons get excited to the conduction band (CB) from the valence band (VB) resulting the generation of holes in VB of the semiconductor material. The photogenerated holes in VB can either oxidize effluent molecules or react with water molecules to generate hydroxyl radicals ($\cdot OH$) that further decompose the effluents molecule to form water and CO_2 as a result of photo-oxidation reaction [12,13]. Simultaneously, superoxide anions (O_2^-) are formed by the reaction between the dissolved oxygen and the CB electrons. The redox reactions are induce by these electrons to produce superoxide anion radical ($\cdot O_2^-$) resulting H_2O_2 supported photo-oxidation reaction [13–15]. The whole photochemical reaction process is shown in figure 1.1.

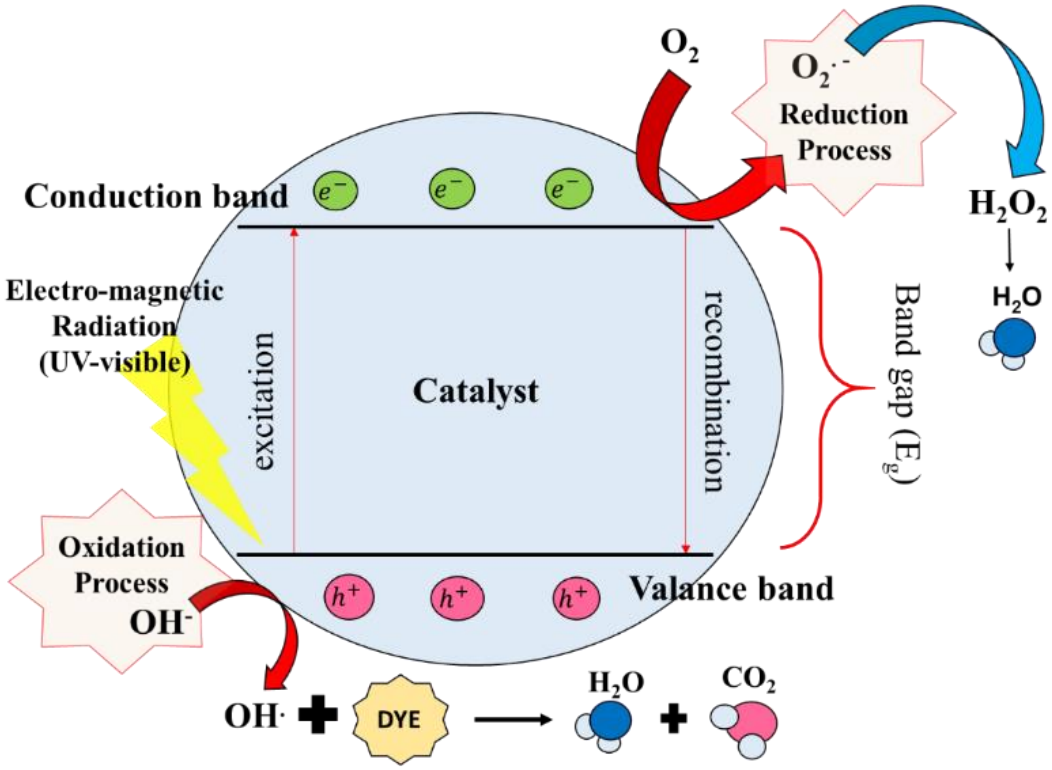

Figure 1.1: Schematic representation of semiconductor photocatalytic process.

The energy gap between the conduction band and valance band of semiconductors is nearly 1.0 - 3.8eV. However, primarily requirement for a semiconductor to be a good photocatalyst are mentioned in figure 1.2. Various semiconductors such as metal oxides, sulphides and selenides are used for photocatalyst. Among them, metal oxides (ZnO, MnO_2, TiO_2, Nb_2O_5, CeO_2 and $NaNbO_3$ etc.) are preferable over sulphides and selenides due to their stability and non-toxic nature [12]. Some of the semiconducting photocatalysts are listed in Table-1.1 along with their optical bandgap energies.

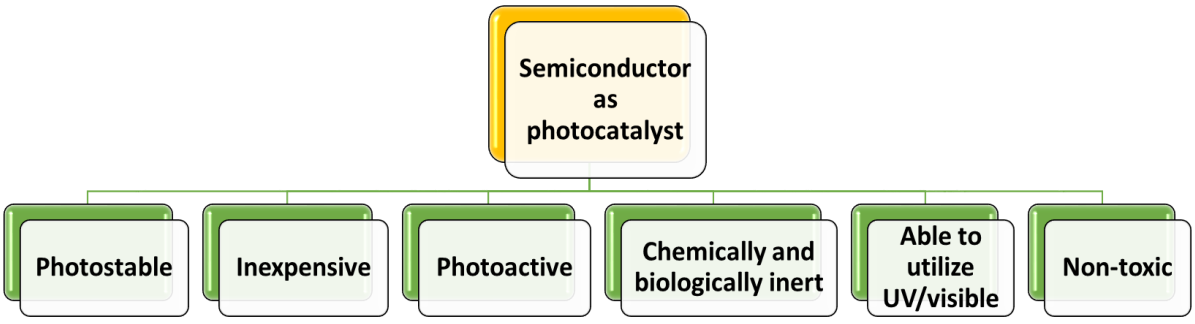

Figure 1.2: Primarily requirement for a good semiconductor to be considered as photocatalyst.

Table 1.1: Band gap energies of some commonly used photocatalyst:

Photocatalyst	Chemical formula	Band gap (eV)	Radiation for activation
Titanium-oxide	TiO_2	3.02	UV
Zinc-oxide	ZnO	3.20	UV
Manganese-oxide	MnO_2	2.54	Visible
Tungsten-oxide	WO_3	2.76	Visible
Vanadium-oxide	V_2O_5	2.70	Visible
Copper-sulfide	CuS	2.5	Visible
Zinc-sulfide	ZnS	3.70	UV
Cadmium-sulfide	CdS	2.58	Visible
Zinc-selenide	ZnSe	2.70	Visible
Gallium-selenide	GaSe	2.1	Visible
Cadmium-selenide	CdSe	1.7	Visible

The photocatalytic reaction is a very complex process including attachment of effluent on catalyst's surface and decomposition of dye through radicals. Some of the parameters which affect the rate of mineralization (formation of CO_2 + H_2O) of organic pollutants by photocatalysis are shown in figure1.3.

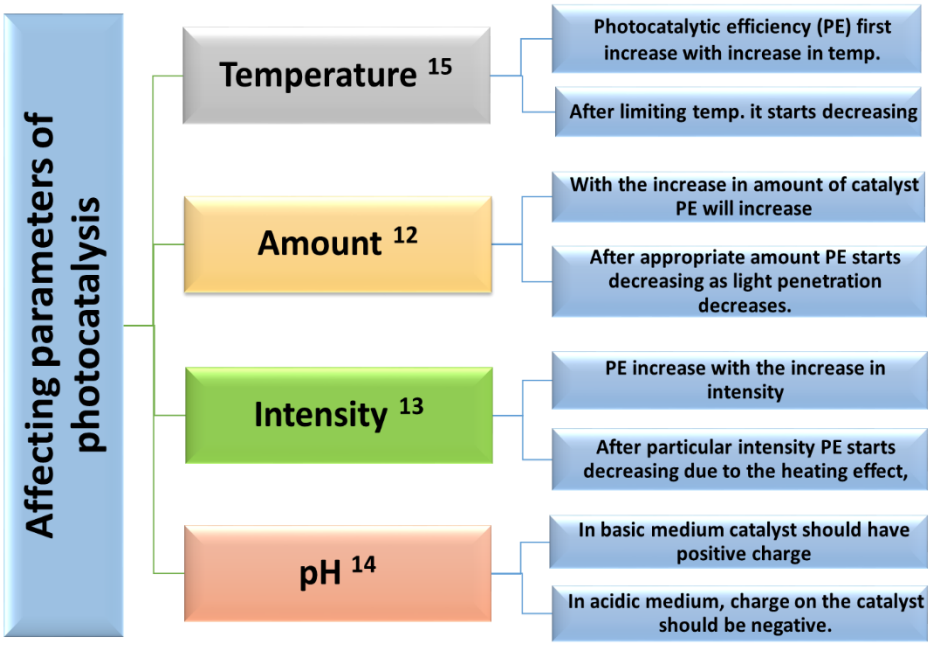

Figure 1.3: Affecting parameters of photocatalysis.

Out of the these discussed parameters, photocatalysis is also being affected by the crystal size, shape, structure and surface area of the catalyst [16,17]. Further, there are several methods that has been studied for enhancing the photocatalytic activity of a material such as composite

system, cationic or anionic doping, heterostructure (schemes) and core-shell morophology [18–20]. Further, photocatalytic processes are being considered as viable solution to environmental problems and have wide range of applications. Figure 1.4 show some of the basic applications of the photocatalysis.

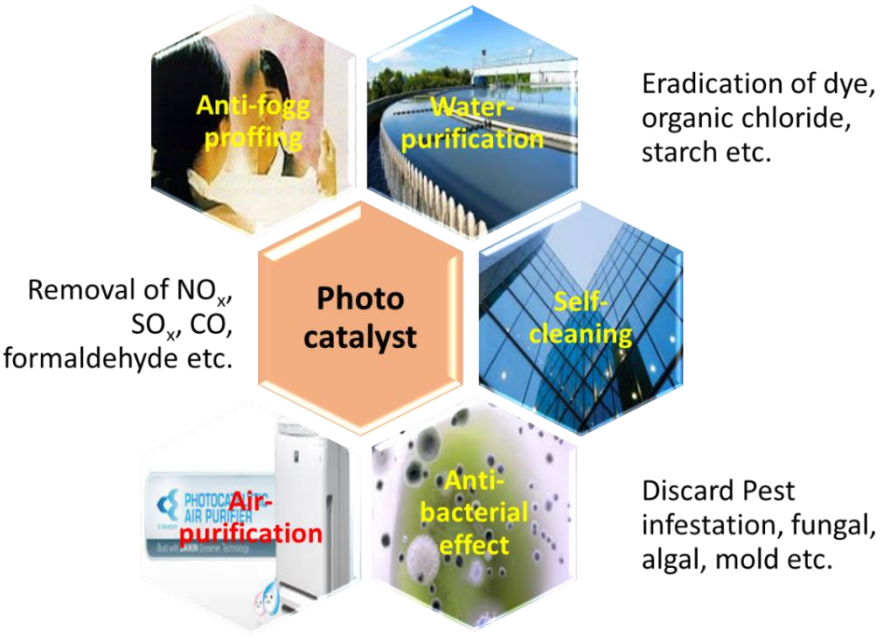

Figure 1.4: Applications of photocatalysis.

1.4. Manganese dioxide (MnO_2) - Need of the hour

A wide range of photocatalysts has been used to examine the photodegradation of different types of dyes. TiO_2 [21], WO_3 [22], RuO_2, ZnO [23] and Bi-compounds [24] are some of the compounds used for the photodegradation of dyes. In the process of photo degradation of organic pollutants, TiO_2 is the most preferring photocatalyst but due to its wide band gap energy approximately, 3.2 eV and due to large band gap it does not exhibits the catalytic activity in visible region [25]. Moreover, the efficiency of conversion of solar energy by the photocatalyst is more fisible in visible region as compared to UV region (only 3-4%). Therefore, the photocatalysts that works under visible light with high photocatalytic activity and lower band gap are prominent material for the photocatalytic applications. In the midst of all these photocatalysts, MnO_2 is of great practical application and has become centre of attraction due to its composition in earth-abundant, considerable redox activity, environmental friendliness and low cost. MnO_2 is a well-known semiconductor which exhibits high absorbance capacity in visible region (400-800 nm) with a band gap of 2.3 eV due to which it is very active in visible light and can easily degrade the organic effluents in visible region by oxidizing or by reducing them.

MnO_x are compounds having berthollide structure which contain lattice oxygen. Because of its labile oxidation state, Mn can effectively play the role of oxidatizing agent as well as reducing agent, Mn is active element of redox reaction in both of the cases as shown below;

Mn as reducing agent $Mn^{+2} - e^- \rightarrow Mn^{+3}$

$Mn^{+3} - e^- \rightarrow Mn^{+4}$

Mn as oxidizing agent $Mn^{+4} + e^- \rightarrow Mn^{+3}$

$Mn^{+3} + e^- \rightarrow Mn^{+2}$

Due to different oxidation states of Mn (3+, 4+, 5+ and 7+), many different oxide systems such as Mn_2O_3, MnO_2 and Mn_2O_7 exist in nature. MnO_2 is considered as one of the stable oxides with interesting physical, optical and chemical properties under ambient conditions. Moreover, MnO_2 exhibited largest number of polymorphs structures in comparision with the serials of manganese oxides which also enhance its uses as a photocatalyst. Due to different oxidation state and low band gap of manganese dioxide, it can be widely used as the inexpensive metal catalytic material for the degradation of many organic pollutants and several kind of dyes.

1.4.1 Introduction to MnO_2

Manganese (IV) oxide exhibits different polymorphs influenced by the alignment of the basic MnO_6 octahedral structure. The catalytic oxidation processes are also influenced by the multiple oxidation states of Mn atoms. The polymorphic property of MnO_2 originates the various applications, which permit the subsistance of non-identical structural forms. As such, they holds tunnels or interlayers with gaps of dissimilar sizes. All the MnO_2 polymorphs share a fundamental atomic structural unit i.e. Mn^{4+} ions in a spin-polarized $3d^3$ configuration and highly polarizable O^{2-} ions in a spin-unpolarized $2p^6$ configuration which are arranged in corner- and edge-sharing MnO_6 octahedral [26]. A variety of polymorphic structures which have been studied significantly for various applications in pigmentation and energy storage are formed by the different packing arrangement of these octahedral structure[27–30] . The different polymorphs of MnO_2 are as follow [31]:

1) Hollandite (α-MnO_2)
2) Intergrowth (γ MnO_2)
3) Pyrolusite (β MnO_2)
4) Ramsdellite (R MnO_2)
5) Spinel (λ MnO_2)
6) Layered (δ MnO_2)

α-, β- and γ-MnO_2 exhibits 1D tunnel in the structure and λ possess 3D layer. While δ-MnO_2 has a 2D layer unique tunnel structure with edge-shared MnO_6 octahedral [32] which also contains the huge amount of lattice oxygen species and active oxygen species on the surface.

Due to the facile preparation process and high catalytic performance, δ-MnO_2 has high potential which support it in the applications of catalyst support [33]. By taking the advantage of layered structure, δ-MnO_2 has been widely used in rechargeable lithium ion batteries [34]. Further, the relationship between electrochemical performance and structure difference of MnO_2 have been explored by many researchers. Devaraj *et al*. [32] studied the electrochemical capacitance properties of five major MnO_2 structures in which he found that the value of specific capacitance follow the order: $\alpha \equiv \delta > \gamma > \lambda > \beta$.

Moreover, MnO_2 is continuously converted into lower oxides under a suitable partial pressure and temperature. MnO_2 and Mn_2O_3 were reported as the catalytically active components whereas the proportion between these two oxides is the results of Mn dispersion, method of preparation, temperature of catalyst process throughout preparation and Mn salts [35,36]. Further, the low calcination temperature and low Mn loading directed towards the MnO_2 formation while Mn_2O_3 phases are formed with high calcination temperature and high Mn loading [36,37].

1.4.2 Properties of MnO_2 over other metal-oxides

In comparision to nobel metals, transition metal oxide have gained much attention due to its plentiful, cheap and good thermal stabilities. These particles have characteristics of electrical, magnetic, thermal, mechanical, dielectric, physicochemical, biological and optical confidants. Among other materials MnO_2 show tremendous photocatalytic properties because of its low band gap, high surface energy, low cost, nontoxicity, high specific capacitance and spatial confinement. MnO_2 acts as a good photocatalyst which can absorb and degrade a wide range of organic pollutents which include organic dyes and many polymers. MnO_2 with high specific surface area show better catalytic performance. Due to high specific surface area it can easily oxidize and adsorb the other phase components and it also contain multi-holes by which oxygen can eventually spread on the surface at their active site, giving almost complete conversion of organic compounds.

As far as capacitance behavior is concerned transition metal oxides and conducting polymers are selected as electroactive electrode materials for pseudo-capacitors [38]. In the application in the military field, RuO_2 is one of the promising element because of its high specific capacitance (SC) of >600 F/g [39]. But due to its high cost and toxic nature RuO_2 restrict its day-to-day application. Therefore, enormous work have been done on different metal-oxides to instigate the reasonable and ecofriendly substitutes, such as MnO_2, CoO_4, Fe_3O_4, NiO [40–43]. In the middle of all these compounds, MnO_2 exhibits high theoretical SC of 1370 F/g^{-1}, which based on the calculation of redox reaction of one-electron per Mn atom [44] and a broad

electrochemical potential of about 0.9–1.0 V. MnO_2 also results in less chemical corrosion by using mild aqueous electrolytes. These unique features of MnO_2 nanoparticles will eventually enables by providing a high-performance, safe, and low cost alternative for all those high-tech carbon-based electrochemical double layered capacitors and many other catalysts. MnO_2 can be used in highly acidic solutions with wide range of pH, while the acidic corrosion cannot be fetched by other transition metal oxides, except for TiO_2. For electrode materials, different forms of MnO_2 have been examined for various energy storage systems, such as alkaline batteries, lithium ion batteries and supercapacitors. MnO_2 is also known as an predominant functional metal oxide in the area of biosensor, ion exchange reactions, catalysis, molecular adsorption and particularly energy storage applications [45]. From the above illustration it can be concluded that MnO_2 is considered as a dependable material with high performance.

References

[1] M.N. Chong, B. Jin, C.W.K. Chow, C. Saint, Recent developments in photocatalytic water treatment technology: A review, Water Res. 44 (2010) 2997–3027. doi:10.1016/j.watres.2010.02.039.

[2] H. Huang, J. Liu, P. Zhang, D. Zhang, F. Gao, Investigation on the simultaneous removal of fluoride, ammonia nitrogen and phosphate from semiconductor wastewater using chemical precipitation, Chem. Eng. J. 08 (2016) 1–32. doi:10.1016/j.cej.2016.08.134.

[3] V. Colla, T. Annunziata, F. Rosito, C. Lucca, Sustainable Reverse Osmosis application for wastewater treatment in the steel industry, J. Clean. Prod. 09 (2015) 1–13. doi:10.1016/j.jclepro.2015.09.025.

[4] S. De Gisi, G. Lofrano, M. Grassi, M. Notarnicola, Characteristics and adsorption capacities of low-cost sorbents for wastewater treatment : A review, Sustain. Mater. Technol. 9 (2016) 10–40. doi:10.1016/j.susmat.2016.06.002.

[5] J.L. and B.E.L. Yujie Feng, Lisha Yang, Electrochemical Technologies for Wastewater Treatment and Resource Reclamation, Environ. Sci. Res. &Technology Rev. 2 (2016) 800–831. doi:10.1039/C5EW00289C.

[6] N.L. Stock, J. Peller, K. Vinodgopal, P. V. Kamat, Combinative sonolysis and photocatalysis for textile dye degradation, Environ. Sci. Technol. 34 (2000) 1747–1750. doi:10.1021/es991231c.

[7] N. Kislov, J. Lahiri, H. Verma, D.Y. Goswami, E. Stefanakos, M. Batzill, Photocatalytic degradation of methyl orange over single crystalline ZnO: Orientation dependence of photoactivity and photostability of ZnO, Langmuir. 25 (2009) 3310–3315. doi:10.1021/la803845f.

[8] IUPAC, Coprecipitation, in: Compend. Chem. Terminol. (the “Gold Book”), 1997: p. 336. doi:10.1351/goldbook.I03352.

[9] C. Materials, Nanocomposites for Visible Light-induced Photocatalysis, first, springer international publishing AG, Dehradun, 2017. doi:10.1007/978-3-319-62446-4.

[10] R. Saravanan, F. Gracia, A. Stephen, Nanocomposites for Visible Light-induced Photocatalysis, in: Springer Int. Publ. AG 2017, 2017: pp. 19–41. doi:10.1007/978-3-319-62446-4.

[11] S.N. Ahmed, W. Haider, Heterogeneous photocatalysis and its potential applications in water and wastewater treatment : a review, Nanotechnology. 29 (2018) 1361–6528. doi:https://doi.org/10.1088/1361-6528/aac6ea.

[12] M.M. Khan, S.F. Adil, A. Al-Mayouf, Metal oxides as photocatalysts, J. Saudi Chem. Soc. 19 (2015) 462–464. doi:10.1016/j.jscs.2015.04.003.

[13] K. Rajeshwar, M.E. Osugi, W. Chanmanee, C.R. Chenthamarakshan, M.V.B. Zanoni, P. Kajitvichyanukul, R. Krishnan-Ayer, Heterogeneous photocatalytic treatment of organic dyes in air and aqueous media, J. Photochem. Photobiol. C Photochem. Rev. 9 (2008) 171–192. doi:10.1016/j.jphotochemrev.2008.09.001.

[14] S. Rehman, R. Ullah, A.M. Butt, N.D. Gohar, Strategies of making TiO2and ZnO visible light active, J. Hazard. Mater. 170 (2009) 560–569. doi:10.1016/j.jhazmat.2009.05.064.

[15] M. Lazar, S. Varghese, S. Nair, Photocatalytic Water Treatment by Titanium Dioxide: Recent Updates, Catalysts. 2 (2012) 572–601. doi:10.3390/catal2040572.

[16] G. Leofanti, M. Padovan, G. Tozzola, B. Venturelli, Surface area and pore texture of catalysts, Catal. Today. 41 (1998) 207–219. doi:0920-5861/98/$32.00.

[17] S. Cao, F. Tao, Y. Tang, J. Yu, Size- and shape-dependent catalytic performances of oxidation and reduction reactions on nanocatalysts Shaowen, Chem. Soc. Rev. 45 (2016) 4747–4765. doi:10.1039/C6CS00094K.

[18] H. Zhao, G. Zhang, Q. Zhang, MnO2/CeO2 for catalytic ultrasonic degradation of methyl orange, Ultrason. Sonochem. 21 (2014) 991–996. doi:10.1016/j.ultsonch.2013.12.002.

[19] A.E. Fischer, K.A. Pettigrew, D.R. Rolison, R.M. Stroud, J.W. Long, Incorporation of homogeneous, nanoscale MnO2 within ultraporous carbon structures via self-limiting electroless deposition: Implications for electrochemical capacitors, Nano Lett. 7 (2007) 281–286. doi:10.1021/nl062263i.

[20] K. Wang, X. Zhang, J. Han, X. Zhang, X. Sun, C. Li, W. Liu, Q. Li, Y. Ma, High-Performance Cable-Type Flexible Rechargeable Zn Battery Based on MnO2@CNT Fiber Microelectrode, ACS Appl. Mater. Interfaces. 10 (2018) 24573–24582. doi:10.1021/acsami.8b07756.

[21] A.R. Khataee, M.B. Kasiri, Photocatalytic degradation of organic dyes in the presence of nanostructured titanium dioxide: Influence of the chemical structure of dyes, J. Mol. Catal. A Chem. 328 (2010) 8–26. doi:10.1016/j.molcata.2010.05.023.

[22] H. Hu, C. Deng, J. Xu, Q. Zheng, G. Chen, X. Ge, Facile synthesis of hierarchical WO3 nanocakes displaying the excellent visible light photocatalytic performance, Mater. Lett. 161 (2015) 17–19. doi:10.1016/j.matlet.2015.07.103.

[23] S. Sakthivel, B. Neppolian, M. V Shankar, B. Arabindoo, M. Palanichamy, V. Murugesan, Solar photocatalytic degradation of azo dye: comparison of photocatalytic efficiency of ZnO and TiO2, Sol. Energy Mater. Sol. Cells. 77 (2003) 65–82. doi:10.1016/j.jid.2015.11.011.

[24] K. Yu, S. Yang, C. Liu, H. Chen, H. Li, C. Sun, S.A. Boyd, Degradation of organic dyes via bismuth silver oxide initiated direct oxidation coupled with sodium bismuthate based

visible light photocatalysis, Environ. Sci. Technol. 46 (2012) 7318–7326. doi:10.1021/es3001954.

[25] Y. Liu, X. Chen, Y. Liu, Black Titanium Dioxide for Photocatalysis, 1st ed., Elsevier Inc., 2017. doi:10.1016/bs.semsem.2017.04.001.

[26] D.A. Kitchaev, H. Peng, Y. Liu, J. Sun, J.P. Perdew, G. Ceder, Energetics of MnO2 polymorphs in density functional theory, Phys. Rev. B. 93 (2016) 1–5. doi:10.1103/PhysRevB.93.045132.

[27] H. Guan, J. Xie, G. Chen, Y. Wang, Facile synthesis of α-MnO2nanorods at low temperature and their microwave absorption properties, Mater. Chem. Phys. 143 (2014) 1061–1068. doi:10.1016/j.matchemphys.2013.11.005.

[28] C.S. Johnson, D.W. Dees, M.F. Mansuetto, M.M. Thackeray, D.R. Vissers, D. Argyriou, C.-K. Loong, L. Christensen, Structural and electrochemical studies of α-manganese dioxide (α-MnO2), J. Power Sources. 68 (1997) 570–577. doi:10.1016/S0378-7753(96)02633-X.

[29] L. Jin, C. hu Chen, V.M.B. Crisostomo, L. Xu, Y.C. Son, S.L. Suib, g-MnO2 octahedral molecular sieve: Preparation, characterization, and catalytic activity in the atmospheric oxidation of toluene, Appl. Catal. A Gen. 355 (2009) 169–175. doi:10.1016/j.apcata.2008.12.012.

[30] M.R. Bailey, S.W. Donne, Structural effects on the cyclability of the alkaline γ-MnO2electrode, Electrochim. Acta. 56 (2011) 5037–5045. doi:10.1016/j.electacta.2011.03.095.

[31] M.M. Thackeray, Manganese oxides for lithium batteries, Prog. Solid State Chem. 25 (1997) 1–71. doi:10.1016/S0079-6786(97)81003-5.

[32] S. Devaraj, N. Munichandraiah, Effect of crystallographic structure of MnO2 on its electrochemical capacitance properties, J. Phys. Chem. C. 112 (2008) 4406–4417. doi:10.1021/jp7108785.

[33] J. Zhang, Y. Li, L. Wang, C. Zhang, H. He, Catalytic oxidation of formaldehyde over manganese oxides with different crystal structures, Catal. Sci. Technol. 5 (2015) 2305–2313. doi:10.1039/C4CY01461H.

[34] S.H. Kim, S.J. Kim, S.M. Oh, Preparation of Layered MnO2 via Thermal Decomposition of KMnO4 and Its Electrochemical Characterizations, Chem. Mater. 11 (1999) 557–563. doi:10.1021/cm9801643.

[35] B.R. Strohmeier, D.M. Hercules, Surface spectroscopic characterization of manganese/aluminum oxide catalysts, J. Phys. Chem. 88 (1984) 4922–4929. doi:10.1021/j150665a026.

[36] S. Imamura, M. Shono, N. Okamoto, A. Hamada, S. Ishida, Effect of cerium on the mobility of oxygen on manganese oxides, Appl. Catal. A Gen. 142 (1996) 279–288. doi:10.1016/0926-860X(96)00095-6.

[37] S. Cavallaro, N. Bertuccio, P. Antonucci, N. Giordano, J.C.J. Bart, Mercury removal from waste gases by manganese oxide acceptors, J. Catal. 73 (1982) 337–348. doi:10.1016/0021-9517(82)90105-1.

[38] G.A. Snook, P. Kao, A.S. Best, Conducting-polymer-based supercapacitor devices and electrodes, J. Power Sources. 196 (2011) 1–12. doi:10.1016/j.jpowsour.2010.06.084.

[39] Chi Chang Hu, Kuo Hsin Chang, Ming Champ Lin, Yung Tai Wu, Design and tailoring

of the nanotubular arrayed architecture of hydrous RuO2 for next generation supercapacitors, Nano Lett. 6 (2006) 2690–2695. doi:10.1021/nl061576a.

[40] D.P. Dubal, R. Holze, Synthesis, properties, and performance of nanostructured metal oxides for supercapacitors, Pure Appl. Chem. 86 (2014) 611–632. doi:10.1515/pac-2013-1021.

[41] T. Cottineau, M. Toupin, T. Delahaye, T. Brousse, D. Bélanger, Nanostructured transition metal oxides for aqueous hybrid electrochemical supercapacitors, Appl. Phys. A Mater. Sci. Process. 82 (2006) 599–606. doi:10.1007/s00339-005-3401-3.

[42] S. Xiong, C. Yuan, X. Zhang, B. Xi, Y. Qian, Controllable synthesis of mesoporous Co3O4 nanostructures with tunable morphology for application in supercapacitors, Chem. - A Eur. J. 15 (2009) 5320–5326. doi:10.1002/chem.200802671.

[43] W. Deng, X. Ji, Q. Chen, C.E. Banks, Electrochemical capacitors utilising transition metal oxides: An update of recent developments, RSC Adv. 1 (2011) 1171–1178. doi:10.1039/c1ra00664a.

[44] M. Toupin, T. Brousse, D. Bélanger, Charge storage mechanism of MnO2 electrode used in aqueous electrochemical capacitor, Chem. Mater. 16 (2004) 3184–3190. doi:10.1021/cm049649j.

[45] Y. Hou, Y. Cheng, T. Hobson, J. Liu, Design and synthesis of hierarchical MnO2 nanospheres/carbon nanotubes/conducting polymer ternary composite for high performance electrochemical electrodes, Nano Lett. 10 (2010) 2727–2733. doi:10.1021/nl101723g.

2. Literature review

The properties and applications of MnO_2 are greatly influenced by its composition, size and morphology. Many research effort have focused on the balanced control of composition and dimensionality of nanomaterials [1]. Based on the desired optical and structural properties of MnO_2, it has become necessary to review the available literature regarding the synthesis of MnO_2. Till date, various morphologies of MnO_2 have been examined such as nanosheets, nanoflower, nanotubes, nanorods, sandwich structure and honeycomb structure etc. Numerous methods have been purposed for the preparation different crystallographic forms of MnO_2 such as sol-gel method, micro-emulsion method, reflux, hydrothermal, rheological phase reaction method, thermal, chemical co-precipitation method, template method and solid-phase synthesis etc. [2–6]. The recent development in the synthesis of MnO_2 has been described below:

Wang *et al.* (2012) [7] have prepared mesoporous MnO_2/polyaniline composite for which aniline monomer (5mmol) was liquefied in trichloromethane ($CHCl_3$) solution. A solution $KMnO_4$ (5mmol/50mL DW) was prepared with the addition of HCl till pH=1. Both the solution were cooled at 0-5°C and then solutions were mixed slowly into the organic solution and placed at 0-5°C in refrigerator for 6 h. Obtained precipitates were filtered and dried overnight at 60°C. In comparison, chemical co-precipitation method was used for the preparation of MnO_2/polyaniline composite (MP-C) in which 0.1M $KMnO_4$ and 0.1M aniline monomers were dissolved in DW and 0.1M HCl solution, respectively. After that $KMnO_4$ solution was enumerated into aniline solution with 15 min stirring then the solution was put into refrigerator for 6 h at 0-5°C. Obtained precipitates were filtered and dried at 60°C for 12 h. XRD results for the MP-I showed amorphous nature and hexagonal birnessite-type MnO_2 while, MP-C exhibited certain degree of crystallinity for both compounds. In electrochemical study, MP-I showed higher specific capacitance of 262 Fg^{-1} which is almost twice to that of MP-C. Therefore, MP-I holds good applications in high-performance electrochemical capacitors.

Kumar *et al.* (2013) [8] synthesized MnO_2 nanoparticles using co-precipitation method. Manganese (II) sulphate and manganese oxalate were used as Mn salts, both of these salts with equal concentration (0.2M) were stirred at 60°C for 1 h and NaOH was added till pH 12 has obtained. Obtained precipitates were dried overnight at 100°C and calcined for 4 h at 500°C. XRD results revealed that the prepared sample was purely crystalline in nature having average particle size 25-30 nm. The broad bands in FTIR spectra at 515 and 480 cm^{-1} are associated with Mn-O which indicated the presence of MnO_2. Further, the sharp absorption at 339.60 nm in UV-visible absorption is also due to MnO_2 nanoparticles. The prepared sample find large number of applications in the field of biosensors, biogenic and bioscience because of its

different physical and chemical properties like energy storage, ion exchange, molecular adsorption etc.

Saputra *et al.* (2013) [9] synthesized three different phases (α, β, γ) of one –dimensional MnO_2 using hydrothermal method. For the preparation of different phases, $MnSO_4.H_2O$ and $(NH_4)_2S_2O_8$ both with equal amount (0.008 mol) were dissolved in distilled water (DW) then put into an autoclave for 12 h at different temperatures (α and β-MnO_2 at 140ºC ,γ-MnO_2 at 90ºC). Afterwards, resultant wet powder was washed and filtered and dried in air. XRD results revealed the different patterns for three different MnO_2 particles and no other phase was observed. Morphologies of the prepared sample were scanned by SEM which revealed the ribbon-like nanowires for α-MnO_2, nanorods for β-MnO_2 and nanofiber like morphology for γ-MnO_2. Absorption spectra of all the three phases show strong absorption in visible region (400-800 nm). BET study revealed that the β-MnO_2 have large surface area while γ-MnO_2 lowest. Further, photodegradation study was also being performed with phenol in which α-MnO_2 exhibted the highest activity for phenol degradation and β-MnO_2 exhibited the lowest degradation activity. Because of the low activation energy and high activity, the prepared α-MnO_2 exhibits excellent catalytic performance and can be used as as alternate to $Co_3O_{4.qw}$

Raj *et al*. (2013) [10] prepared MnO_2 nanoparticles from sonochemical reduction using $KMnO_4$ and a reducing agent polyethylene glycol (PEG) at room temperature. XRD results indicated the short-range crystallinity of 10-20nm sized nanoparticles as observed from electron microscopy. The electrochemical performance of MnO_2 suggested the specific capacitance of $282Fg^{-1}$ at a current density of $0.5mA.cm^{-2}$ in 1M $Ca(NO_3)_2$ electrolyte enabling it's usage in electrochemical supercapacitors as a appropriate electrode material.

Toufiq *et al*. (2013) [11] synthesized 1D single-crystal MnO_2 nanowires by hydrothermal method. Primarily, 1.0 g $(NH_4)_2S_2O_8$ and HNO_3 (0.5 mL) were added to $KMnO_4$ solution (2 g in 40 mL of DW) and sonicated for 15 min, followed by calcination (in stainless steel autoclave) at 180°C for 15 h. The resultant precipitates were filtered and dried at 90 °C for 5 h. XRD and SEM confirmed the crystalline nature of even and high-quality of MnO_2 nanowires with diameter of 15–20 nm. The optical studies of the prepared sample suggested a strong UV emission band, blue emission band and a weak defect-related green emission band at 380, 452, 542 nm respectively, with 2.5 eV optical band gap.

Toufiq *et al*. (2013) [12] have also synthesized hexagonal MnO_2 shrimps like nanostructure by facile hydrothermal method. Typically, 3.0 g $KMnO_4$ was added in 40 mL of DW with continuous stirring for 45 min. Meanwhile HNO_3 was added in the solution drop by drop and then solution was calcined for three days at 175°C in autoclave. The resultant powder was

centrifuged, filtered and dried in an oven for 6 h at 90°C. XRD results of the prepared sample matches with single crystal hexagonal phase MnO_2 having 24 nm crystallite size. FESEM and HRTEM results show smooth shrimps like single crystalline structure. Moreover, prepared MnO_2 showed 90% absorption of visible radiation with 1.65 eV direct band gap which assured its solar cell application.

Ma *et al.*(2014) [13] synthesized nanocomposite of Ag/MnO_2/RGO by sonochemical method to study its application as electrode material as supercapacitors. Initially, MnO_2 altered graphene oxide (GO) sheets were synthesized by using graphite oxide and $KMnO_4$. Then Ag/MnO_2/RGO composite was synthesized by using as-prepared MnO_2/GO and silver nitrate. Basically, MnO_2/GO (20 mg) was dissolved in DW (40 mL) and sonicated for 1 h, then appropriate amount of silver nitrate was added to the solution after that NaOH (0.25 mL) was added with continuous stirring for 3 h, then the mixture was put into flask with round-bottom and was refluxed for 1 h at 90°C. The obtained powder was centrifuged, washed and dried for 24 h at 45°C. The electrochemical study revealed that the prepared composite exhibited high capacitance (467.5 Fg^{-1}) and good recycling stabilities.

Li *et al* (2014) [14] synthesized MnO_2 nanoflowers by electrochemical deposition. For the preparation of MnO_2 nanoflowers, particles were electrodeposited in the solution of $Mn(AC_2)$ (0.1 M), NH_4Ac (0.02 M) and 10 % dimethylsulfoxide, when the particles were deposited then the electrodes were washed, dried at 60°C for 2 h and annealed at 200°C for 3 h. In electrochemical study the prepared sample exhibited high specific capacitance about 314 Fg^{-1} at current density 1 Ag^{-1}.

Abulizi *et al*. (2014) [15] prepared MnO_2 nanoparticles by sonochemical reduction of MnO_4^-. For the preparation of MnO_2, $KMnO_4$ (0.1 mM) with aqueous argon (60 mL) solution was kept at 20°C in the water bath. Further, H_2SO_4 or NaOH was used to control the pH (2.2 or 9.0-9.4). UV-vis spectrophotometer was performed to measure the spectra of absorption for the concentration of MnO_4^- in irradiated solution. All the pattern in XRD results confirmed that the prepared nanoparticles show δ-MnO_2 phase having low crystallinity. The SEM results showed that the size shape and morphology of prepared sample was clearly affected by the pH of the solution. TEM images show that the morphology of the sample was changed to needle or sheet-like nanostructure to spherical nanoparticles and then large polyhedron nanoparticles at 2.2, 6.0 and 9.3 pH, respectively. From all the results it was concluded that the irradiation time was one of the essential reason for the preparation of the sample.

Li *et al.* (2014) [16] synthesized MnO_2/carbon nanotubes (CNTs) composite using one-pot reaction process. Basically for the preparation of MnO_2/CNTs composite commercial

multiwalled CNTs (100 mg) and $KMnO_4$ (2.5 g) were grind together and dissolved in 100mL DW with 10 min stirring, after that H_2SO_4 (0.5mL) was added to the solution and the solution was kept at 80°C in oil bath with stirring for 1 h. The resultant powder was washed, filtered and dried for 12 h at 60 °C. XRD, TG, XPS, TEM, SEM, FESEM and Raman were used to analyze the composition, microstructure, morphology and oxidation state of the product. Moreover, pure MnO_2 was also synthesized through same process for comparison. Electrochemical study revealed the high specific capacitance around 201 F g^{-1}, good cycle stability and also markable rate capability of composite sample.

Xiong *et al*. (2015) [17] synthesized MnO_2 honeycomb nanospheres/carbon nanoparticles/graphene (MnO_2/C/G) composite by freeze-drying method. For the preparation of honeycomb MnO_2 nanospheres, $KMnO_4$ (1.0 g) was added into DW (500 mL) with 30 min stirring. Later on oleic acid (10 mL) was added into the solution to form steady emulsion. Thereafter, brown-black colored precipitates were collected and washed with DW and alcohol and then finally dried under vacuum for 12 h at 80 °C. Further, MnO_2/C/G composite were produced by freeze and drying. Raman spectra showed a peak at 645 cm^{-1} that recognized with Mn-O stretching. TEM, FE-SEM and EDX were executed to confirm the morphology and structure of prepared sample. MnO_2/C/G composite showed better electrochemical performance (255 Fg^{-1} at of 0.5 Ag^{-1}). All the results indicated that the composite have great potential in supercapacitors like applications.

Sagadevan S (2015) [18] fabricated MnO_2 nanoparticles by co-precipitation method. For the synthesis of the sample $MnSO_4.H_2O$ and manganese oxalate were dissolved in DW and stirring for 30 min at 50 °C then drop wise NaOH was added into the solution and the solution was again stirred for 1h at 60 °C. To obtain precipitates, ethanol was added to the solution and dried overnight at 100 °C. Finally, the prepared sample was heated at 500 °C for 3 h. XRD revealed the crystallite size about 22 nm. The morphology of the sample was studied using SEM which indicated the smaller size of randomly distributed grains and high agglomeration in the nature of particles. Absorption spectra results showed absorption between 200-600 nm wavelength range. The dielectric study revealed that the dielectric loss and dielectric constant decreased when the frequency was increased and get constant at high frequency.

Bai *et al.*(2015) [19] synthesized three-dimensional Ag/MnO_2 catalyst by impregnation method for catalytic removal of formaldehyde. Firstly, to synthesize 3D-MnO_2, KIT-6 Silica was synthesized then a solution of as-synthesized KIT-6 silica (4.0 g) and $Mn(NO_3)_2.4H_2O$ was prepared and calcined at 400 °C for 6 h to obtain the final product. Ag/MnO_2 was prepared using appropriate amount of $AgNO_3$ and as-synthesized MnO_2 which was then calcined at 400 °C for 5 h. XRD results

revealed the β-MnO_2 crystalline phase. From TEM micrographs it was very clear that the 4.3 % Ag/MnO_2 has smaller Ag nanoparticle (3 nm) then the 8.9 % Ag/MnO_2 (5 nm). Raman pattern of the prepared samples indicated that the peak width and intensity of 8.9 % Ag/MnO_2 are larger than that of 4.3 % Ag/MnO_2. And from the catalytic study it was concluded that 8.9 % Ag/MnO_2 catalyst was stable and highly active for the removal of formaldehyde.

Srither *et al*. (2016) [20] synthesized porous MnO_2 by sonochemical and soft template method. In sonochemical method (sample A) $KMnO_4$ (0.5 g) and PEG (5 mL in 50 mL DD water) are used as precursors while in soft template method (sample B) $Mn(CH_3COO)_2$ and $KMnO_4$ were used. XRD results revealed the amorphous nature of both the prepared samples. In EDX study negligible amount of impurities were seen in sample A while sample B shows higher purity (Mn and O elements). SEM/TEM study shows the rod-shapedfor sample A and flake-like morphology for sample B. Sample B exhibited higher specific surface area of 1559m^2g^{-1} as compared to A in BET analysis. Li_2SO_4 and Na_2SO_4 electrolytes were used for the investigation of electrochemical capacitor behavior of both the samples which indicated the high specific capacitance value about 280 F g^{-1} and good capacity retention (92.31%) in Na_2SO_4 electrolyte for sample B in comparison with Li_2SO_4 electrolyte.

Zhao *et al.*(2016) [21] synthesized MnO_2/polyaniline (MP) composites by a simple reaction between $KMnO_4$ and aniline to study its electrochemical properties for supercapacitor. For the synthesis of MP composite, $KMnO_4$ (3.16 g) was dissolved in DW (150 mL). Further different amount of aniline (0.5, 1, 1.5, 2.0, 2.5 mL) was added into $KMnO_4$ solution in 5 separate solutions (MP 0.5, MP 1.0, MP 1.5, MP 2.0 and MP 2.5). Lastly, the powder was washed and dried for 3 h at 70 °C. XRD results revealed the amorphous nature of the prepared sample. FTIR spectra showed broad bands associated with the various functionalities present in the composite. TEM micrographs showed the poriferous structures and indicated the amorphous nature of the prepared composites which give high specific surface area. Moreover, in electrochemical study MP1.5 composite showed the best electrochemical properties with good specific capacitance (497 F/g), high surface area (480 m^2g^{-1}) and good cycling performance (88.2%) at current density about 10 Ag^{-1}.

Manganese-oxide-coated diatomite was synthesized by **Dang *et al* (2016)** [22] using wet-chemical procedure. For catalyst preparation $KMnO_4$ (0.1M) was dissolved in DW and a solution of 6.0 M HCl was prepared separately. Diatomite (1 g) was dissolved in 10 mL $KMnO_4$ solution, dropwise 6.0 M HCl was then added to the above solution followed by 4 h stirring. Finally, the precipitates were washed and dried for 48 h at room temperature. SEM micrographs showed that the diatomite and MnO_2 were uniformly distributed with high porosity. BET

results revealed the high surface area (126.28 m^2/g) for the prepared sample. XRD results also showed the uniform distribution and layered structure of birnessite MnO_2. The photocatalytic study indicated that the prepared sample was a good catalyst which degraded the methylene blue (MB) and methyl orange (MO) in short duration of time (30 min).

Yu *et al.*(2017) [23] synthesized CuO_x/MnO_2 heterostructures by using hydrothermal method to study its photocatalytic activity for poisonous wastewater treatment. For the preparation of MnO_2 nanowires, $KMnO_4$ (1.715 g) was dissolved in DW (25mL) and 2.5 mL HCl was added into the solution with 1 h stirring, then the solution was put into stainless autoclave and heated for 12 h at 180 °C in oven. Finally, the precipitates were washed, filtered, dried for 3 h at 80 °C and calcined under N_2 environment for 1 h at 500 °C. For the preparation of CuO_x/MnO_2, as-synthesized MnO_2 (0.174 g) was dispersed in 50 mL of DW, glucose (0.2 g) and $Cu(AC)_2.H_2O$ (0.2 g) were added into the solution while stirring for 10 min. Resultant product was heated in water bath at 90 °C for 1 h and then the powder was washed by filtration, dried overnight at 50°C. Finally, the product was heated at 150 °C for 180 min in tubular furnace under N_2 protection. Also by changing the amount of $Cu(AC)_2.H_2O$ (0.3 g, 0.4 g) two more sample were made. XRD, SEM, UV and PL characterization were performed for all the prepared samples. In the photocatalytic study of all the prepared composite sample show good photodegradation of MB dye which is about 96.1 % in 140 min.

Lin *et al,* (2017) [24] prepared a novel Al/MnO_2 composite through ball milling using zirconia balls (300 g). Aluminum powder (10 g) and MnO_2 ratio of $Al:MnO_2$, were 4.03 g (8:1), 3.22 g (10:1), 2.69 g (12:1), 2.30 g (14:1) with different milling durations (18, 24 and 30 h). XRD results confirmed the formation of composite including two phases MnO_2 and Al. The SEM/EDX confirmed the homogeneous distribution of MnO_2 particles on the aluminum surface. FTIR spectra of the sample revealed that the sample in which milling was done for 18 h exhibited maximal reflectivity and largest particle size i.e. with the increase in the milling time, the reflectivity of the sample decreases. The IR and vis–NIR reflectance spectra show that when Al: MnO_2 ratio down from 8: 1 to 14:1, the reflectivity of samples was increased. All the results indicated that the composite can be used to enhance the visible agility for the low infrared emission coating.

He *et al.* (2017) [25] used hydrothermal method to synthesize MnO_2 nanosheets and nanowires on montmorillonite (MMt). For the preparation of nanosheets, montmorillonite K 10 (100 mg) was added in $KMnO_4$ solution (0.05 mol-30 mL) followed by 10 min stirring and 15 min ultrasonic treatment and then the mixture kept in autoclave for 24 h at 160°C. Finally, the obtained powder was washed and dried at 60°C. For the preparation of nanowires, MMt (0.21

g) was dissolved in 30 mL DW and then $(NH_4)_2S_2O_8$ (2.212 g), $KMnO_4$ (1.85 g) were added into the solution while stirring. Resultant solution was put into autoclave for 12 h heat treatment at 90°C. Various diffraction peaks in XRD result show the formation of MnO_2 nanosheets and nanowires on MMt. FTIR results also indicated the formation of MnO_2 nanosheets and nanowire on MMt. Morphology of the prepared samples was being observed by SEM which clearly showed the nanosheet and nanowire like structure. Moreover, MB dye was used for the degradation study which results in 97.7 % removal in 5 min at pH = 2 and 92.8 % at pH = 11 for MnO_2 nanosheets on MMt which clearly indicated its application in wastewater treatment.

Gagrani *et al*. (2017) [26] synthesized MnO_2 nanorods by mechano-chemical processing and a study was done on the decolorization of rhodamine B (RB) at different pH levels for photocatalytic activity. The $KMnO_4$, $MnCl_2$ and KCl mixture was milled for 4h and then calcined at 350 °C for 1 h., afterwards the powder was washed to remove KCl and the remaining powder was dried for 9 h at 50 °C. XRD and TEM results revealed the formation of nonocrystalline α-MnO_2 with irregular surface. Moreover, absorbance spectroscopy indicated the band gap for amorphous is 2.54 eV and for crystalline MnO_2 band gap is around 2.33 eV. Amorphous MnO_2 showed good photocatalytic activity for large-scale industrial effluents as it can degrade the dye even when it is not expose to light in neutral pH state.

Selvakumar *et al.*(2017) [27] prepared birnessite type MnO_2 using $Mn(NO_3)_2$ and H_2O_2 in KOH solution. Firstly, a 200 mL solution of KOH (0.6 $molL^{-1}$) and 200 ml H_2O_2 (3 %) was prepared then the solution was added in 100 mL $Mn(NO_3)_2.xH_2O$ (0.2 $mol.L^{-1}$) followed by 2 h stirring and 24 h ageing. Finally, the precipitates were filtered out, washed, dried overnight at 100 °C and get calcined for 3 h at different temperatures (300, 450 and 600°C). In XRD study the sample which was calcined at 300 °C showed birnessite type structure. Surface area was calculated using BET study which was about 184 m^2g^{-1}. XPS and time-of-flight secondary ion mass spectroscopy (ToF-SIMS) analysis was performed for the prepared sample to know about the mechanism of catalyst deactivation. Moreover, catalytic performance was observed with formaldehyde (HCHO).

Wang *et al.* (2018) [28] prepared hollow capsules of nanosheet based MnO_2 by the hydrothermal method by using of pre-fabricated hollow SiO_2 capsules. 5 g of SiO_2 templates (capsule shaped) were dissolved in $KMnO_4$ (50 gL^{-1}, 60 mL) solution and then the prepared sample was heated at 150 °C for 48 h in stainless steel autoclave. NaOH (2 M) was used as etchant to eliminate SiO_2 templet. In the XRD results, the diffraction peaks of the prepared sample are matched with layered birnessite-type MnO_2 (δ- MnO_2). FESEM and TEM results

indicated the hollow interior MnO_2 capsules. Moreover, the synthesized capsules showed large discharge capacity which enable its use in Li-ion batteries.

Lia *et al*. (2018) [29] reaction of deep eutectic solvent (DES) of choline chloride-urea was used to synthesized ε- MnO_2 over Mn^{+2}/MnO_4^-. DES was prepared by choline chloride-urea (1:2). Further, 30 mL DES was prepared by dissolving $MnSO_4.H_2O$ and $KMnO_4$ with different molar ratios (5:3, 4.5:3 and 4:3) at different reaction time (8, 6, 4 and 2h). XRD results revealed that the prepared MnO_2 was pure ε-MnO_2 and the diffraction peaks (100) revealed that the prepared powder were crystalline in nature in (100) plane. Irregular blocky-shape of all the materials are revealed by the SEM images. The TEM images revealed that all the samples were formed by the accumulation of irregular and intersecting flakes. The band gap of samples were calculated in the range of 1.25-1.52 eV. In photocatalytic experiment, catalyst (40 mg) 5 ml 30 % H_2O_2 and RhB (50 mL) solution was prepared then placed in visible light irradiation and the RhB absorbance was observed at 553 nm. The photocatalytic experiment showed the high activity and good stability of prepared samples for photodegradation of RhB dye.

Xu *et al.* (2018) [30] fabricated MnO_2 nanorods by using hydrothermal method with microwave heating for the generation of more Mn^{4+} on MnO_2 surface to refine the oxygen electroreduction. Here $MnSO_4.H_2O$ (0.4 g) and $KMnO_4$ (1.0 g) were used as precursors. For making homogeneous solution both of the precursors were dissolved in 30 mL DW and kept in magnetic stirring, then put into an autoclave under 140 °C heating temperature for 12 h. Obtained solution was centrifuge, get washed with copious deionized water and dried at 50 °C. Lastly, 0.1 g of the prepared sample was kept in microwave for different heating time interval (0, 5, 10, 20, 30 and 40 min). Further, XRD, SEM, TEM, XPS, and electrochemical measurements were performed for the prepared sample. All the results indicated that the MnO_2 nanoroads which were heated for 30 min in microwave have more Mn^{4+} ions on the surface and showed good oxygen reduction reaction (ORR) which is comparable to Pt/C catalyst.

Hoseinpour *et al.* (2018) [31] adopted a green approach to synthesize MnO_2 nanoparticles by green method using curcumin as stabilizing agent and Y.gloriosa leaf extract as reducing agent with manganese acetate as Mn source. Manganese acetate (20 mL of 0.01Mm aqueous solution at pH 8) dissolved in leaf extract (180 ml) and curcumin extract solution (20 mL) with continuous stirring for 60 min and the solution was centrifuged and remaining precipitates were washed and dried. Broad diffraction hump in XRD pattern indicated the amorphous nature of MnO_2 nanoparticles. The bands at 650 and 520 cm^{-1} are related to bending and stretching of O-Mn-O bond in FTIR spectra confirmed the formation of MnO_2 nanoparticles. UV-vis spectroscopy of MnO_2 nanoparticles showed the absorbance at 410 nm. Broad distribution of

particles size (50-100 nm) has been observed through FESEM. The photocatalytic degradation of acid orange dye was performed with synthesized MnO_2 nanoparticles in which good photocatalytic activity was observed with 33 % degradation.

Shen *et al.* (2018)[32] used hydrothermal method to obtain α-MnO_2 and α-MnO_2/activated carbon (MAC) composite. For the preparation of activated carbon (AC) alkaline activation method was performed using rice husk. For the composition of composite, $MnSO_4.H_2O$ (0.676 g) and $KClO_3$ (0.980 g) were dissolved in DW (70 mL). Later, different mass ratio (MnO_2/AC = 1/9, 3/7, 5/5 or 7/3) of AC with MnO_2 was added to the solution with 15 min of ultrasonication treatment then drop wise 20 mL of HNO_3 was added into the solution and put the solution in autoclave and heated for 6 h at 120 °C. Lastly, by washing, centrifuging and dried the precipitates at 60 °C for 6 h MAC was obtained. MnO_2 was also prepared using same method without adding AC and calcined for different time (1, 3, 6, 9 and 12 h) at 120 °C. XRD results showed the α-MnO_2 phase and the SEM results indicated that the morphology change from nanorods to actiniaria like structure with the increase in heating time. The prepared sample with mass ratio 1:1 (MnO_2/AC) showed the largest discharge value (977.4 C/g), in Mott-Schottky and the EIS test this composite showed large carrier concentration and lower charge-transfer resistance than MnO_2 which indicated that the electrochemical performance of the supercapacitors could increase by the preparing composite.

Dai *et al.* (2018)[33] prepared α, β, and γ-MnO_2 nanoparticles for electrochemical analysis. α-MnO_2 was synthesized by grinding 2.206 g of $Mn(Ac)_2.4H_2O$ and 0.9482 g of $KMnO_4$ for 30 min, heated for 4 h at 120°C after that the solid was washed and dried overnight at 80 °C. For the fabrication of β-MnO_2, $MnSO_4.H_2O$ (0.008 mol) and $(NH_4)_2S_2O_8$ (0.008 mol) were dissolved in 35 ml of DW with continuous stirring then the solution was kept in autoclave and heated for 12 h at 140 °C. Finally, the product was washed and dried at 60 °C. Afterwards, the synthesized γ-MnO_2, $MnSO_4.H_2O$ (3.375 g) and $(NH_4)_2S_2O_8$ (4.575 g) were dissolved in 80 mL DW with stirring for half an hour and then the solution was kept in autoclave for heat treatment at 90 °C for 24 . The resultant powder was washed and dried overnight at 70 °C. XRD and SEM analysis was done for the prepared samples to understand the phase composition and morphologies for different MnO_2. Moreover in electrochemical study detection range of 10-800 μM was observed for nitrite using differential pulse voltammetry to know the electrochemical oxidation behavior to find its application as sensing devices.

Xiao *et al.* (2018)[34] synthesized MnO_2 nanosheets and microflowers using facile one-step process by hydrothermal method and photocatalytic activity for organic dyes was studied. Basically, 0.01 M of Na_2SO_4 and 0.01 M of $KMnO_4$ solution were prepared, respectively and

from it different molar ratio of $KMnO_4$: Na_2SO_4 (1:1, 2:1, 3:1) were prepared. Then the solution was put in autoclave for heat treatment at 140 °C for 10 h. Lastly, the powder was centrifuged, washed, dried for 12 h at 80 °C and calcined at 350 °C for 2 h. The morphology study revealed that the prepared sample showed variation in morphology. XRD analysis revealed the β-MnO_2 phase of the prepared samples. The surface area and pore size distribution of 31.38 m^2g^{-1} and 6.3 nm, respectively was analyzed from BET. Photocatalytic activity was performed with methylene blue (MB) and methyl orange (MO) under UV light irradiation which resulted in degradation about 91.1 % in 30 min of MB and 89.8 % in 120 min of MO. All the results of photocatalytic activity showed that the prepared samples have good application in the removal of organic effluents from water.

Facile synthetic method was adopted by **Lin *et al.*(2019)** [35] to synthesized Novel MnO_2-doped holey carbon (MnKACS) to study its electrochemical performance. To synthesize porous KOH-activated chitosan-derived carbon (KACS) solution appropriate amount of KOH and Chitosan was dissolved to make homogeneous mixture and proper heat treatment was given to the solution. For the preparation of MnKACS, 0.2 g of KACS was dissolved in DW (200 mL), and then $KMnO_4$ (0.01 g) was added into the solution with stirring at 75 °C. Obtained powder was centrifuged, washed and dried overnight at 85 °C. Two more samples were synthesized of $KMnO_4$/KACS (2: 20 and 3: 20 weight ratio) named as MnKACS-2 and MnKACS-3. The electrochemical performance of the synthesized samples indicated that the MnKACS-2 material exhibited the good gravimetric capacitance (460 Fg^{-1} at 0.2 Ag^{-1}) and capacitance reservation (91.67% at 10 Ag^{-1}over 10,000 cycles) suggesting that the sample could be used to manufacture the high-performance supercapacitor electrode materials.

Shimamura *et al.* (2019) [36] synthesized MnO_2 nanoparticles by breath figure method to analyze its application for hybrid capacitor electrodes. For the preparation of the MnO_2, $MnCl_2.4H_2O$ (450 mg) was dissolved in DW (45 mL) with stirring for 15 min, then dimethylformamide (150 μL) and NaOH (45 mL of 0.05 M) solution was added to the solution under slow stirring for 2 h. Finally the solution was centrifuged, washed, dried at 35 °C for 12 h and sintered for 2 h at 400 °C. XRD pattern of the sample matched with the α-MnO_2 phase. Round particles formation with diameter about 20 nm has been obtained in SEM & TEM results. The electrochemical study revealed that the MnO_2 nanoparticles with large mesoporous structure exhibited the increase in specific capacitance (37.0 to 100.5 Fg^{-1}) in comparisons to without structure control.

References

[1] C.N.R. Rao, S.R.C. Vivekchand, K. Biswas, A. Govindaraj, Synthesis of inorganic nanomaterials, J. Chem. Soc. Dalt. Trans. (2006) 3728–3749. doi:10.1039/b708342d.

[2] S. Ching, D.J. Petrovay, M.L. Jorgensen, S.L. Suib, Sol-Gel Synthesis of Layered Birnessite-Type Manganese Oxides Stanton, Inorg. Chem. 15 (1981) 289–290.

[3] P. Yu, X. Zhang, Y. Chen, Y. Ma, Z. Qi, Preparation and pseudo-capacitance of birnessite-type MnO2 nanostructures via microwave-assisted emulsion method, Mater. Chem. Phys. 118 (2009) 303–307. doi:10.1016/j.matchemphys.2009.07.057.

[4] X. Tang, Y. Li, X. Huang, Y. Xu, H. Zhu, J. Wang, W. Shen, MnOx-CeO2 mixed oxide catalysts for complete oxidation of formaldehyde: Effect of preparation method and calcination temperature, Appl. Catal. B Environ. 62 (2006) 265–273. doi:10.1016/j.apcatb.2005.08.004.

[5] A. Aprahamian, A. Teymurazyan, A. Susalla, N. Cuka, Preparation of ultrafine MnO2 powders by the solid state method reaction of KMnO4 with Mn(II) salts at room temperature, Hyperfine Interact. 132 (2001) 413–420. doi:10.1023/A:1011927825975.

[6] S. Chen, J. Zhu, X. Wu, Q. Han, X. Wang, Graphene oxide-Mno2 nanocomposites for supercapacitors, ACS Nano. 4 (2010) 2822–2830. doi:10.1021/nn901311t.

[7] J. Wang, Y. Yang, Z. Huang, F. Kang, Interfacial synthesis of mesoporous MnO2 / polyaniline hollow spheres and their application in electrochemical capacitors, J. Power Sources. 204 (2012) 236–243. doi:10.1016/j.jpowsour.2011.12.057.

[8] H. Kumar, P. Sangwan, v, Int. J. Chem. Chem. Eng. 3 (2013) 155–160. doi:ISSN 2248-9924.

[9] E. Saputra, S. Muhammad, H. Sun, H.M. Ang, M.O. Tade, S. Wang, Different Crystallographic One-dimensional MnO2 Nanomaterials and Their Superior Performance in Catalytic Phenol Degradation, Environ. Sci. Techonolgy. 47 (2013) 5882–5887. doi:10.1021/es400878c.

[10] B. Gnana Sundara Raj, A.M. Asiri, A.H. Qusti, J.J. Wu, S. Anandan, Sonochemically synthesized MnO2nanoparticles as electrode material for supercapacitors, Ultrason. Sonochem. 21 (2014) 1933–1938. doi:10.1016/j.ultsonch.2013.11.018.

[11] A.M. Toufiq, F. Wang, Q.U.A. Javed, Q. Li, Y. Li, Hydrothermal synthesis of MnO2 nanowires: Structural characterizations, optical and magnetic properties, Appl. Phys. A Mater. Sci. Process. 116 (2014) 1127–1132. doi:10.1007/s00339-013-8195-0.

[12] A.M. Toufiq, F. Wang, Q. Javed, Synthesis, Characterization and Optical Property of Shrimps-Like Nanostructures of MnO2 by Hydrothermal Route, J. Nanosci. Nanotechnol. 13 (2013) 2948–2952. doi:10.1166/jnn.2013.7408.

[13] L. Ma, X. Shen, Z. Ji, G. Zhu, H. Zhou, Ag nanoparticles decorated MnO2/reduced graphene oxide as advanced electrode materials for supercapacitors, Chem. Eng. J. 252 (2014) 95–103. doi:10.1016/j.cej.2014.04.093.

[14] W. Li, K. Xu, B. Li, J. Sun, F. Jiang, Z. Yu, R. Zou, Z. Chen, J. Hu, MnO2 Nanoflower Arrays with High Rate Capability for Flexible Supercapacitors, ChemElectroChem. 1 (2014) 1003–1008. doi:10.1002/celc.201400006.

[15] A. Abulizi, G.H. Yang, K. Okitsu, J.J. Zhu, Synthesis of MnO2nanoparticles from sonochemical reduction of MnO4Oin water under different pH conditions, Ultrason.

Sonochem. 21 (2014) 1629–1634. doi:10.1016/j.ultsonch.2014.03.030.

[16] L. Li, Z.A. Hu, N. An, Y.Y. Yang, Z.M. Li, H.Y. Wu, Facile synthesis of MnO2/CNTs composite for supercapacitor electrodes with long cycle stability, J. Phys. Chem. C. 118 (2014) 22865–22872. doi:10.1021/jp505744p.

[17] Y. Xiong, M. Zhou, H. Chen, L. Feng, Z. Wang, X. Yan, S. Guan, Synthesis of honeycomb MnO2nanospheres/carbon nanoparticles/graphene composites as electrode materials for supercapacitors, Appl. Surf. Sci. 357 (2015) 1024–1030. doi:10.1016/j.apsusc.2015.09.111.

[18] S. Sagadevan, Investigations on Synthesis , Structural , Morphological and Dielectric Properties of Manganese Oxides Nanoparticles, J. Mater. Sci. Eng. 4 (2015) 4–6. doi:10.4172/2169-0022.1000172.

[19] B. Bai, Q. Qiao, H. Arandiyan, J. Li, J. Hao, Three-Dimensional Ordered Mesoporous MnO2-Supported Ag Nanoparticles for Catalytic Removal of Formaldehyde, Environ. Sci. Technol. 50 (2015) 2635–2640. doi:10.1021/acs.est.5b03342.

[20] S.R. Srither, A. Karthik, S. Arunmetha, D. Murugesan, V. Rajendran, Electrochemical supercapacitor studies of porous MnO2 nanoparticles in neutral electrolytes, Mater. Chem. Phys. 183 (2016) 375–382. doi:10.1016/j.matchemphys.2016.08.041.

[21] Y. Zhao, C.A. Wang, Nano-network MnO2/polyaniline composites with enhanced electrochemical properties for supercapacitors, Mater. Des. 97 (2016) 512–518. doi:10.1016/j.matdes.2016.02.120.

[22] T. Dang, A. Narayan, Q. Tran, S. Roy, Fast degradation of dyes in water using manganese-oxide-coated diatomite for environmental remediation, J. Phys. Chem. Solids. 98 (2016) 50–58. doi:10.1016/j.jpcs.2016.06.006.

[23] T. Yu, Y. Sun, C. Zhe, W. Wang, P. Rao, Synthesis of CuOx/MnO 2 Heterostructures with Enhanced Visible Light-Driven Photocatalytic Activity, J. Mater. Sci. Eng. 5 (2017) 12–25. doi:10.4236/msce.2017.510002.

[24] Y. Liu, J. Xie, M. Luo, B. Peng, C. Xu, L. Deng, The synthesis and optical properties of Al/MnO2composite pigments by ball-milling for low infrared emissivity and low lightness, Prog. Org. Coatings. 108 (2017) 30–35. doi:10.1016/j.porgcoat.2017.03.019.

[25] Y. He, D. Bin Jiang, J. Chen, D.Y. Jiang, Y.X. Zhang, Synthesis of MnO2 nanosheets on montmorillonite for oxidative degradation and adsorption of methylene blue, J. Colloid Interface Sci. 510 (2018) 207–220. doi:10.1016/j.jcis.2017.09.066.

[26] A. Gagrani, J. Zhou, T. Tsuzuki, Solvent free mechanochemical synthesis of MnO2for the efficient degradation of Rhodamine-B, Ceram. Int. 44 (2018) 4694–4698. doi:10.1016/j.ceramint.2017.12.050.

[27] S. Selvakumar, N. Nuns, M. Trentesaux, V.S. Batra, J.M. Giraudon, J.F. Lamonier, Reaction of formaldehyde over birnessite catalyst: A combined XPS and ToF-SIMS study, Appl. Catal. B Environ. 223 (2017) 192–200. doi:10.1016/j.apcatb.2017.05.029.

[28] Y. Wang, P.-S. Ding, M.-G. Zou, W.-B. Guo, D.-X. Wang, F.-C. Zhang, Synthesis of nanosheet-based MnO<inf>2</inf>hollow capsules and their application in lithium batteries, Ferroelectrics. 522 (2018) 6. doi:10.1080/00150193.2018.1392209.

[29] X. Lai, Y. Cheng, C. Han, G. Luo, Synthesis of ε-MnO $_2$ in deep eutectic solvent for visible-light-driven photocatalytic activity, Mater. Res. Innov. 8917 (2018) 1–5. doi:10.1080/14328917.2018.1473991.

[30] K. Xu, X. Lin, X. Wang, L. Li, Z. Zhu, Y. Tian, Generating more Mn 4+ ions on surface of nonstoichiometric MnO2 nanorods via microwave heating for improved oxygen electroreduction, Appl. Surf. Sci. 459 (2018) 782–787. doi:10.1016/j.apsusc.2018.08.095.

[31] V. Hoseinpour, M. Souri, N. Ghaemi, Green synthesis , characterisation , and photocatalytic activity of manganese dioxide nanoparticles, (2018) 1–4. doi:10.1049/mnl.2018.5008.

[32] H. Shen, Y. Zhang, X. Song, Y. Liu, H. Wang, H. Duan, X. Kong, Facile hydrothermal synthesis of actiniaria-shaped α-MnO2/activated carbon and its electrochemical performances of supercapacitor, J. Alloys Compd. (2018). doi:10.1016/j.jallcom.2018.08.228.

[33] Y. Dai, J. Huang, H. Zhang, C. Chiun, Highly sensitive electrochemical analysis of tunnel structured MnO2 nanoparticle-based sensors on the oxidation of nitrite, Sensors Actuators B. Chem. 281 (2019) 746–750. doi:10.1016/j.snb.2018.11.014.

[34] L. Xiao, W. Sun, X. Zhou, Z. Cai, F. Hu, Facile synthesis of mesoporous MnO2 nanosheet and micro flower with efficient photocatalytic activities for organic dyes, Vacuum. 156 (2018) 291–297. doi:10.1016/j.vacuum.2018.07.045.

[35] Z. Lin, X. Xiang, K. Chen, S. Peng, X. Jiang, L. Hou, Facile synthesis of MnO2 nanorods grown on porous carbon for supercapacitor with enhanced electrochemical performance, J. Colloid Interface Sci. 540 (2019) 466–475. doi:10.1016/j.jcis.2019.01.053.

[36] N. Shimamura, R. Kanda, Y. Matsukubo, Y. Hirai, H. Abe, Y. Hirai, T. Yoshida, H. Yabu, A. Masuhara, Preparation of Hierarchic Porous Films of α - MnO2 Nanoparticles by Using the Breath Figure Technique and Application for Hybrid Capacitor Electrodes, ACS Omega. 4 (2019) 3827–3831. doi:10.1021/acsomega.8b03381.

Gaps in the study

Since, Mn exhibits multiple oxidation states which has induced the applicability of MnO_2 as capacitor to store charge. Several work have been done using of MnO_2 as an active material for electrochemical application. But it can also be used to alter the optical emission characteristics for better photocatalytic performance. Despite of being a visible active semiconductor, MnO_2 has not been explored for photocatalytic applications much.

Moreover, in photocatalytic study most of the researcher are focusing on the adsorption and degradation phenomenon, but the concept of dye sensitization was not focused much. Most of the adsorption and degradation studies were followed by pollutants which are visible active and the catalyst (MnO_2) was also visible active, so we cannot directly state that whether the dye itself being decomposed or it is adsorbed and degraded by the catalyst. So, it needs to be explored more about the photocatalytic performance of MnO_2 and associated reaction kinetics which could describe the overall process.

As discussed in the literature review, MnO_2 can be synthesized through different routes but sonochemical route is a facile and single-step process which is very beneficial to synthesize small nanoparticle. Raj *et al*. (2013) and Ma *et al.* (2014) have demonstrated sonochemical route to synthesize ultra-small sized MnO_2 with very high specific surface area for capacitive applications. Such facile technique can also provide better photocatalytic degradation of organic pollutants due to higher extent of adsorption on the surface of catalyst.

The objective of the present work is to understand structural, optical and morphological features of MnO_2 nanoparticles synthesized through sonochemical route. Further, the work proceed to understand the adsorption and photodegradation activity of synthesized MnO_2 and effect of concentration of dye and its detailed reaction kinetics will also be studied.

3. Experimental work

In this study, MnO_2 nanopowder has been successfully synthesized via sono-chemical method (co-precipitation method followed by ultrasonication) using potassium permanganate ($KMnO_4$, *SD-fine chem Ltd*) as manganese source and polyethylene glycol (PEG, *Lab. Reagents & Fine Chemicals*) as a reducing agent. All the precursors are of high purity with analytical grade and were used without any further purification. The detailed description followed for synthesis process is discussed below:

3.1. Methodology

For the synthesis of MnO_2 nanopowder two separate solution were prepared in which 0.5 g of potassium permanganate ($KMnO_4$) and 5.5 g of PEG were dissolved in 40 ml and 20 mL distilled H_2O, respectively. Both the solutions were allowed for continuous stirring of 30 min at 60 ºC. both of the reagents get dissolved in distilled water. Then, $KMnO_4$ solution was sonicated for 60 min and meanwhile, solution of PEG was added dropwise into it. Brown-colored precipitates were obtained after 60 min of sonication and then the solution was kept overnight. Obtained precipitates were then filtered using filter paper and washed a few times with distilled water and finally with ethanol. The obtained powder sample was dried at 70 ºC for 12 h and then the obtained powder was ground using mortal pestle. Moreover, stepwise methodology has also been represented in figure 3.1.

3.2 Characterization

3.2.1 X-ray diffraction (XRD)

X-ray diffraction (XRD) technique is used for identification of various phases synthesized material based on the diffraction pattern. The diffraction of X-rays as a result of chemical reaction or post heat treatment can be used to determine interplanar spacing of different atomic planes through constructive interference following Bragg's Law.

$$\boldsymbol{2d.\ sin\theta = n\lambda} \tag{3.1}$$

where, d = spacing between adjacent atomic planes, θ = diffraction angle (degrees), λ = wavelength of incident X-ray (nm), n equal to the order of the diffraction. In this study, XRD analysis was performed on *PANalytical X'Pert Pro* XRD diffractometer with Cu-Kα (λ=1.5418 Å) radiation in the range of 20–80° (2θ) with 0.013˚ as step size, current range of 40 mA and applied voltage of 45 kV. The nature of the synthesized powered sample was analyzed by

comparing the obtained XRD pattern in *X'pert Highscore plus* software with the International Centre of Diffraction Data (ICDD) cards.

Figure 3.1: Flow chart for the synthesis of MnO_2 nanopowder.

3.2.2 UV-vis spectroscopy

UV–visible spectroscopy is performed to analyze the optical properties of the prepared sample. UV–visible spectroscopy identify the absorption or reflectance characteristics of a material in

the UV and visible region. In this study, the spectra of UV-visible absorbance was recorded with *Hitachi U3900H spectrophotometer* instrument at room temperature in wavelength spectral range of 200-800 nm [1]. Calibration for wavelength and zero PMT function of the instrument was done before testing the sample. $BaSO_4$ tablets was used as reference for taking the baseline in case of solid sample and in case of liquid simple distilled water or ethanol is used as reference. The sample holder is used to place the sample and exposed to rays in UV-Vis range. Finally, the graph of transmittance (% T) vs wavelength was recorded.

3.2.3 Fourier transformation infrared spectroscopy (FTIR)

FTIR is an rigorous technique which is used to distinguish the functional groups and vibrational mode associated with molecule. In this technique, the wavelength that are absorbed by the material are characteristic of its molecular structure. In the present study, FTIR spectra was obtained from *Perkin Elmer-Spectrum-RF-1* in the range 400-2000 cm^{-1} at room temperature. For the sample preparation, 2 mg of prepared sample and 200 mg of KBr were mixed together. Then assemble the powder within the die to form pallet and then examine under microscope.

3.2.4 Transmission electron spectroscopy (TEM)

Transmission electron spectroscopy (TEM) is a very powerful technique used to study morphology of nanomaterials in material science and works on the same principles as that of light microscopy but instead of light, it uses electrons. The sample to be studied is exposed to very high energetic beam of electron and observed images or micrographs captured are analyzed computationally. Further, it can also be used to analyze the quality, size, shape and how densely the particles are packed [2]. In this study, as-prepared sample was scanned on *JEOL2100F* instrument with operating voltage about 200 kV. For the sample preparation, limited amount (0.1 mg) of sample was dispersed in ethanol and sonicated for 1 h to obtain homogeneous dispersed solution. Prior to examine under microscope, 30 µl solution was dropcasted on Cu grid coated with carbon and dried overnight.

3.2.5 Brunauer–Emmett–Teller (BET)

Brunauer–Emmett–Teller serves the basic analysis for the estimation of surface area of the material. Physical adsorption of gas molecules on a surface of the solid sample is explained by BET. The BET theory usually applies for multilayer adsorption and use probing gases that do not react chemically with material surfaces to have accurate results for specific surface area of the material. Generally, in BET methods nitrogen gas is used as adsorbate for probing the solid sample surface. In the present work, the N_2 adsorption-desorption analysis was observed on

Bel, Japan, Inc, Microtec BELSORP MINI-II to calculate BET specific surface area, pore volume and pore size.

3.2.6 Photocatalytic activity

A thorough analysis of photocatalytic reaction of as-synthesized MnO_2 was checked through absorption and degradation of methylene blue (MB) dye and N-phenol, which are considered as model organic pollutants. In both the cases, 100 ml of 2.0 mg/L solution was prepared. The 10 mg of the prepared catalyst was added into the above solution and kept in dark chamber with continuous stirring for 30 min to establish adsorption-desorption equilibrium. Thereafter, the solution was exposed to visible irradiation under household CFL lamp (85 W; 8900 lux) for 120 min. After each interval of 30 min, a 3 ml aliquant was taken out and centrifuged at 4500 RPM. The obtained supernatant was then analyzed under *Hitachi U3900H Spectrophotometer* to know about the concentration profile of MB dye. Further, the same experiment was repeated with different concentration (3.0, 4.0, 5.0, 6.0, 7.0, 8.0, 9.0 and 10.0 mg/L) and also at different pH (2.0, 5.0, 7.0, 10.0 mg/L at 2.0 and 10.0 pH) of MB dye to understand the photocatalytic performance of synthesized MnO_2 and its photo chemical kinetics.

Reference

[1] A. Gupta, O.P. Pandey, Visible irradiation induced photodegradation by NbC/C nanocomposite derived from smoked cigarette litter (filters), Sol. Energy. 163 (2018) 167–176. doi:10.1016/j.solener.2017.12.033.

[2] David B. Williams C. Barry carter, Transmission Electron Microscopy, springer, 2009.

4. Results and discussion

In the present work, the as-synthesized nanopowder was analyzed by various characterization techniques such as X-ray diffraction (XRD) technique. Absorption spectra was recorded to estimate the optical band gap of synthesized sample. Fourier transformation infrared spectroscopy (FTIR) was used to check the presence of different functional groups and to understand the morphology of the prepared sample transmission electron microscopy (TEM) and Brunauer–Emmett–Teller (BET) for surface area analysis was performed. Further, the photocatalytic study has been done with two organic pollutants (MB dye and N-phenol) and its reaction kinetics was also studied in the present work.

4.1. X-ray diffraction (XRD) analysis

Figure 4.1 represented the XRD diffraction pattern of synthesized sample in which less intense broad peaks indicated the presence of MnO_2 nano-crystallites embedded in amorphous network as reported by many research groups [1–5]. The diffraction pattern of the prepared sample was matches with the ICDD card no. 01-075-1560 which indicated the two broad peaks/humps at ~37º and ~60º which are associated with the (004) and (314) plane respectively.

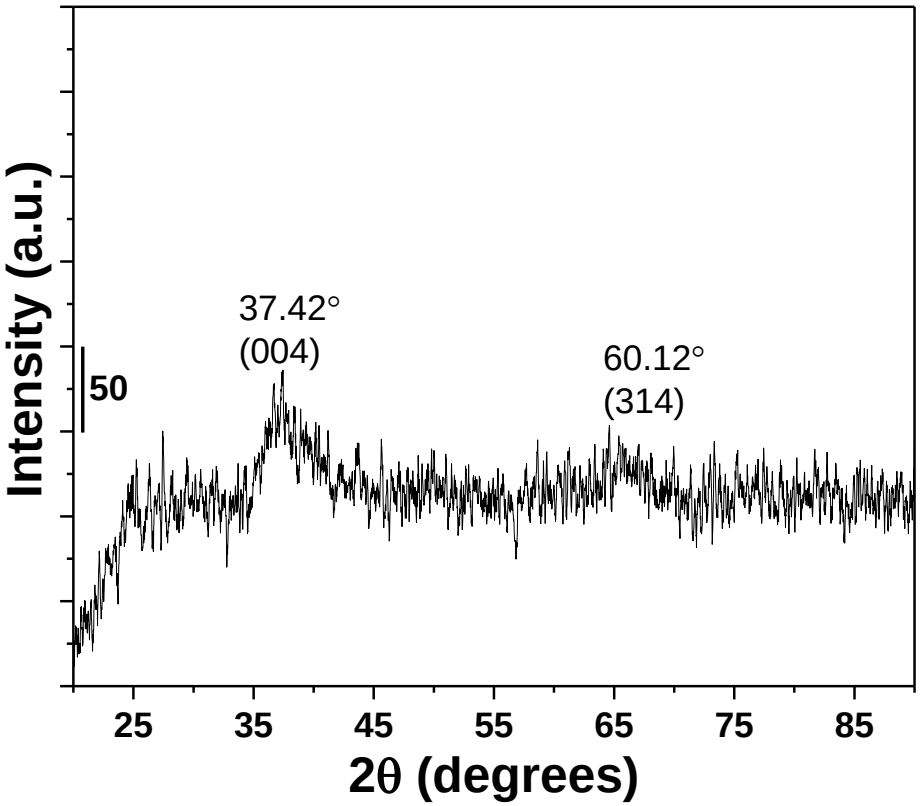

Figure 4.1: XRD diffraction pattern of synthesized sample

4.2. Microstructural analysis

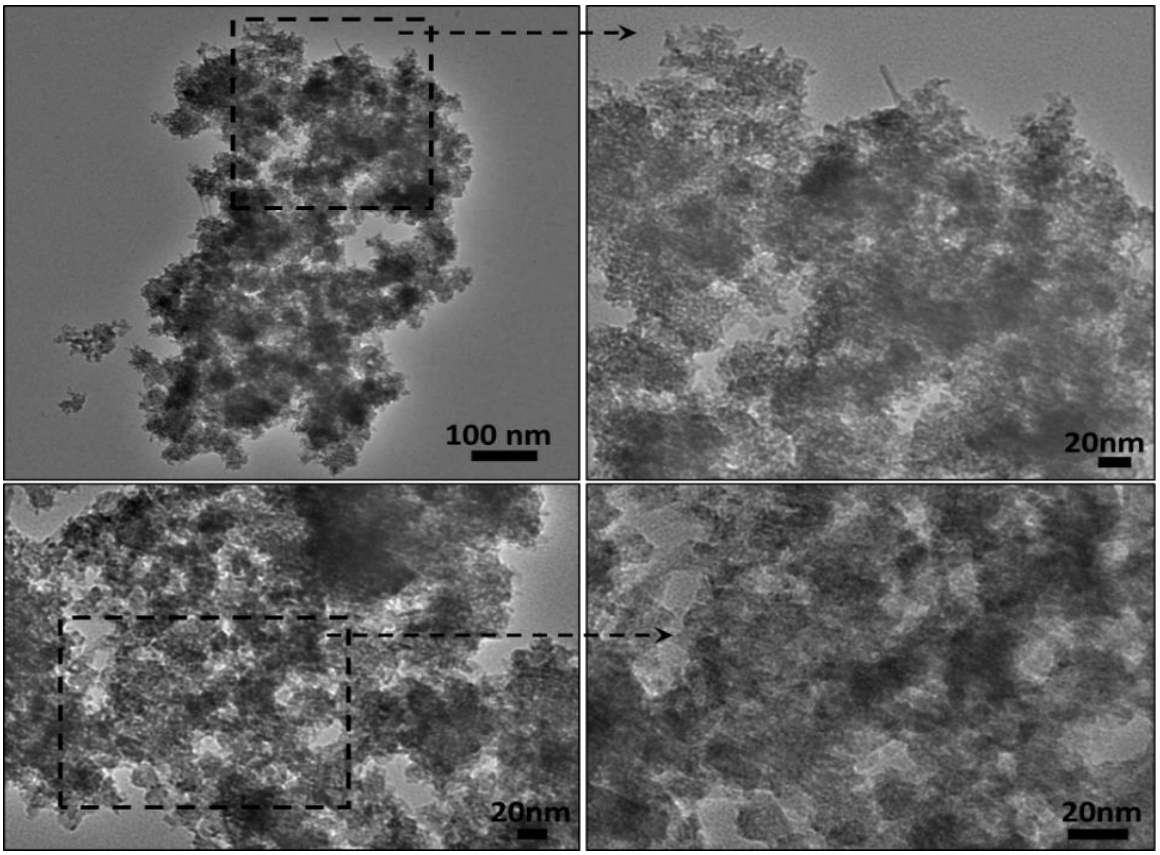

Figure 4.2: TEM graphs of prepared MnO_2 nanopowder.

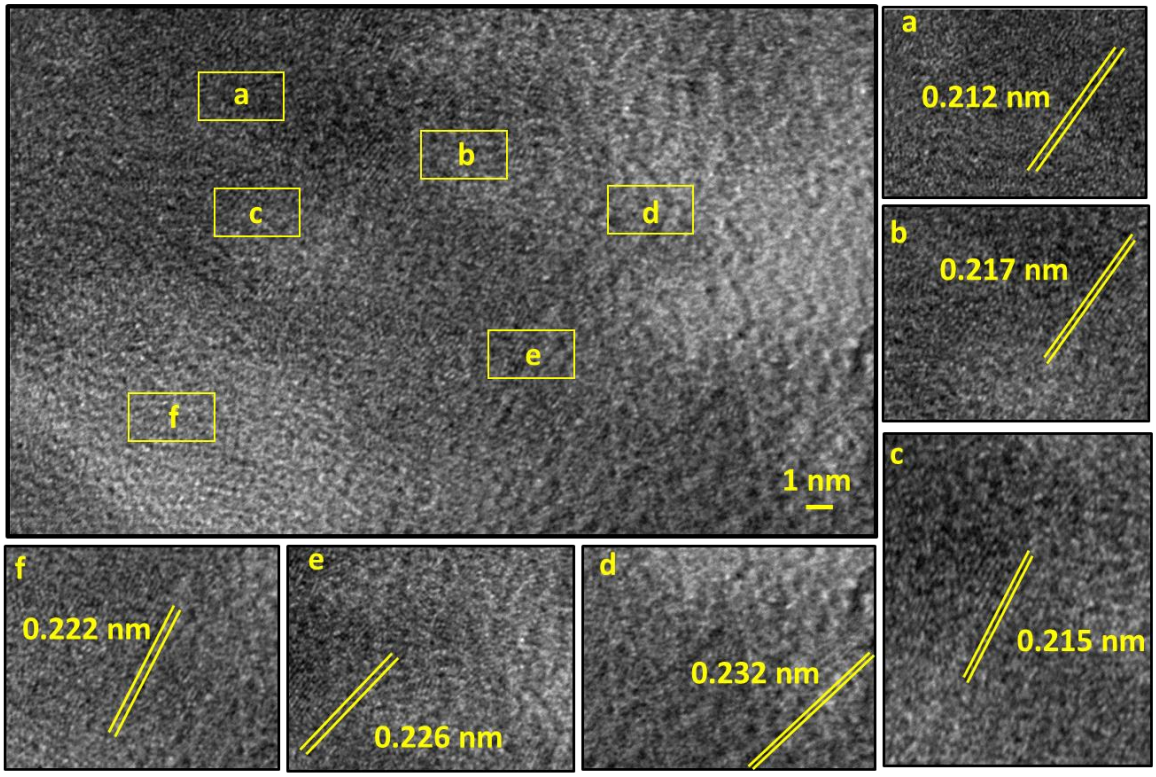

Figure 4.3: HR-TEM micrograph of MnO_2 nanopowder suggesting the presence of nano-crystallites network.

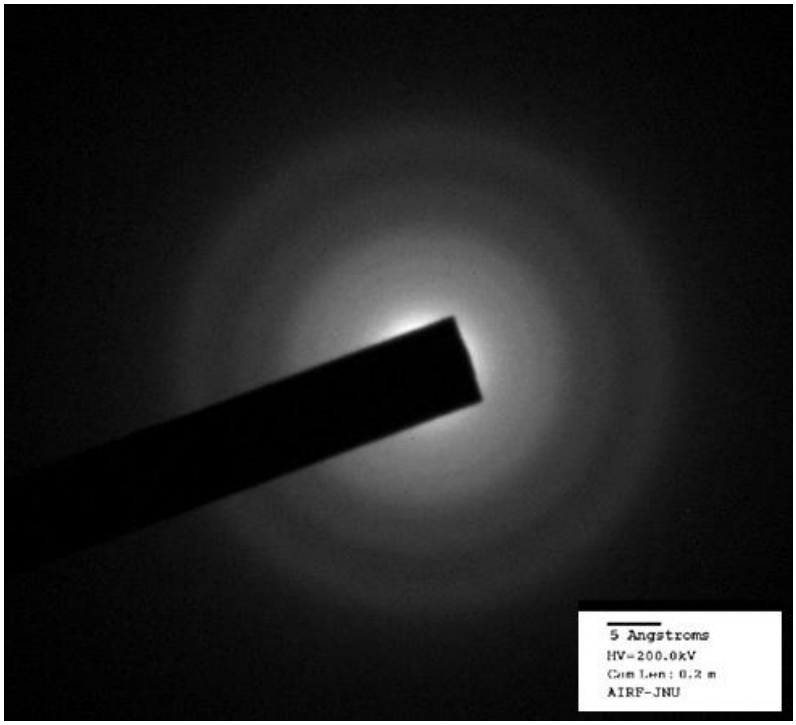

Figure 4.4: SAED pattern of prepared sample.

To observe the morphological features of the prepared sample, TEM has been carried out and some of the general scans are shown in figure 4.2. TEM micrographs have also supported the XRD results, which show a very large porous network like morphology consisting of very small crystallites of prepared sample without any specific directional growth feature as shown in Figure 4.3 [2]. HR-TEM images at different regions with lattice fringes where the fringe width about 0.212, 0.217, 0.215, 0.232, 0.226, 0.222 nm are correlated with the d-spacing in XRD pattern and confirmed the formation of nanocrystalline MnO_2 as shown in Figure 4.3 a-f. Further, SAED pattern also supported the XRD results with single ring (very dull) associated to ~37º (004) plane as shown in figure 4.4 [6].

4.3. Fourier transformation infrared spectroscopy (FTIR) analysis

Figure 4.5 represents the FTIR spectra of the prepared MnO_2 nanopowder. The transmittance bands in FTIR spectra of as-synthesized MnO_2 sample confirmed the formation of MnO_2 where the broad bands were observed at 500-650, 1000-1100, 1346 and 1413 cm^{-1} are related to the O-Mn-O, Mn-O (MnO_6 octahedra), Mn-OH, Mn=O and bending of Mn-OH, respectively and broad transmittance band near ~1585 cm^{-1} is associated to the weak stretching of -OH bond [7–10].

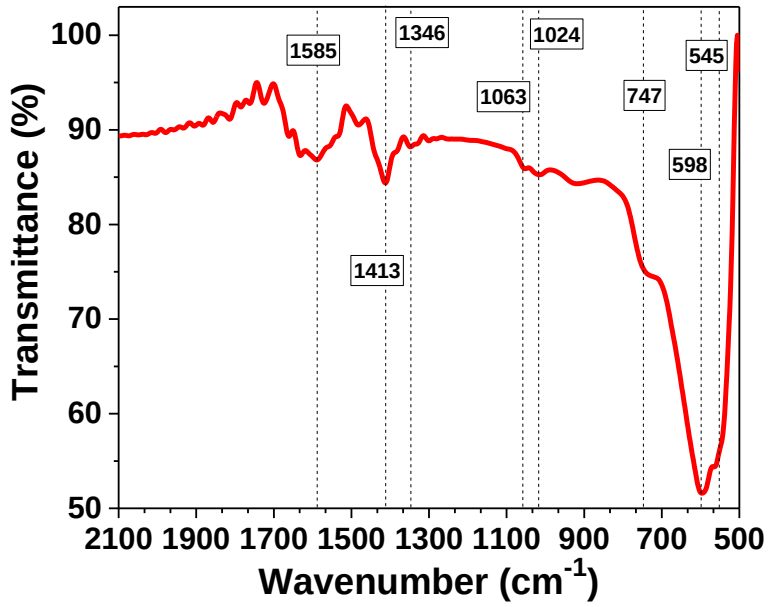

Figure 4.5: FTIR spectra of nanocrystalline MnO_2 representing the presence of different IR modes of Mn-O bond.

4.4. Optical analysis

The formation of MnO_2 has also been observed with optical absorbance spectroscopy. The absorbance spectroscopy revealed the visible absorption characteristics of as-synthesized sample at 345 nm as shown in figure 4.6(a). In case of semiconductors, the optical band gap is calculate by Tauc relation which is mainly used to illustrate the optical assets of amorphous materials:

$$(\alpha h\nu)^n = A\left(h\nu - E_g\right) \quad (4.1)$$

where, α is the absorption coefficient, hν is the energy of photon, A is a constant and n = 2 for direct inter-band transitions and n = 1/2 for indirect transitions [11]. The exact value of band gap was obtained by simply proposed interpolation and extrapolation the straight-line of the graph between $(\alpha h\upsilon)^2$ vs hυ and the intercept to x-axis that give the band gap value of the material. The calculated value of the band gap was 2.53 eV as shown in figure 4.6(b) [12].

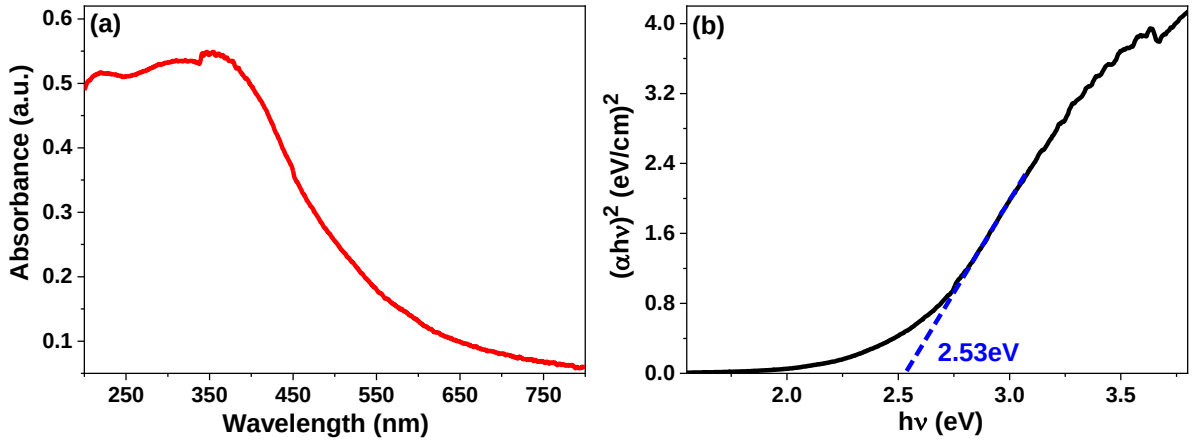

Figure 4.6: (a) UV-vis absorption spectra and (b) Tauc plot of MnO_2 samples.

4.5. Surface area analysis

N_2 adsorption-desorption was performed to analyze the surface features of the prepared MnO_2 nanoparticles. Figure 4.7 (a) represents the N_2 adsorption-desorption isotherm plot showing IV type isotherm with H_3-type hysteresis loop and the range of P/P_0 is in between 0.3 and 1.0 such kind of results show mesoporous characteristics of the sample [13–15]. Figure 4.7 (b) represents the Barrett-Joyner-Halenda (BJH) pore size distribution which confirmed the presence of mesoporicity with great range of distribution. Furthermore, specific surface area and total pore volume of as-synthesized MnO_2 was determined by BET analysis which resukted out to be 104 m^2/g and 0.3901 cm^3/g (respectively) with the average pore diameter 14.96 nm.

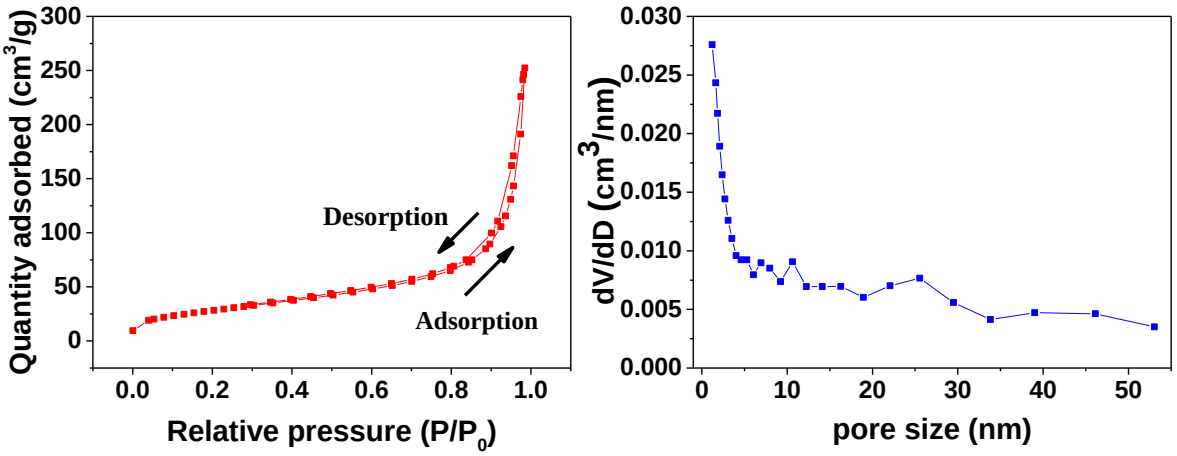

Figure 4.7: (a) N_2 adsorption-desorption curve (BET), (b) the BJH desorption (dV/dD) plot.

4.6. Adsorption and photocatalysis study

The adsorption and photocatalytic study of synthesized MnO_2 nanopowder was evaluated by two different organic effluents (MB dye and N-phenol) which were excited in visible and UV region (respectively) to eliminate the effect of dye sensitization. The UV-visible spectra was measured for both of the effluents which gave maximum absorbance peak at 664 and 405 nm, respectively. Before light-irradiation, photocatalyst was dispersed in the both solutions for 30 min and kept in dark chamber with continues stirring and UV-vis spectra of the absorbed solution was taken. The establishment of adsorption-desorption equilibrium was carried out by decrease in the concentration of solution which has been plotted in the gap of 2 min as shown in Figure 4.8. Figure 4.8 suggested the saturation of adsorption of MB and N-phenol molecules on the surface of catalyst. The adsorption efficiency (A%) of the effluents on the surface of the photocatalyst was calculated using (1):

$$Ads(\%) = \left(\frac{C - C_0}{C}\right) \times 100 \quad (4.2)$$

Where, C_0 represent the concentration of the dye at any time t and C is the initial concentration. As a result of adsorption study, 96.2% and 86.9% adsorption of MB dye and N-phenol (respectively) has been observed on the surface of synthesized MnO_2 nanopowder.

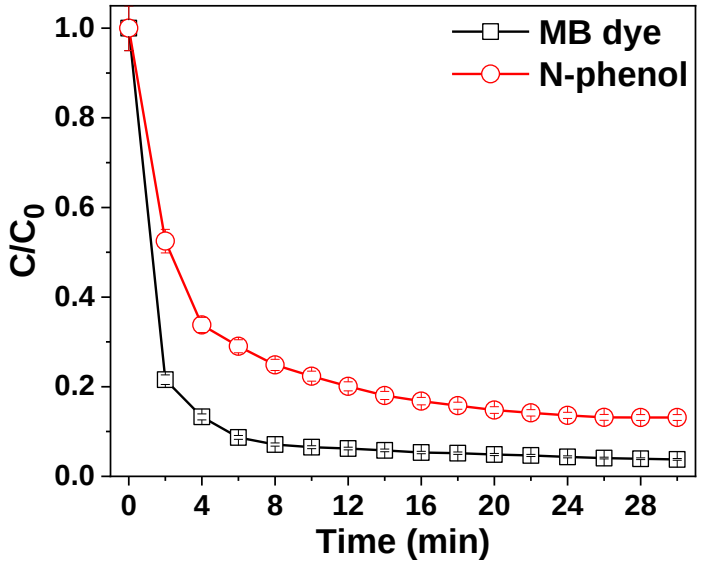

Figure 4.8: Adsorption of MB dye and N-phenol: C/C_0 vs. time.

To understand the adsorption process of MB dye and N-phenol by our photocatalyst more effectively, the experimental data were compared with different kinetic model: the pseudo first and second order reaction kinetics model.

The pseudo first-order kinetics curves were generated by the $\ln(C/C_0)$ v/s irradiation time (t) graph. The first order rate constant (K_1) was obtained by the slope of each linear fitted line from the data points by the blew relation:

$$-\ln\left(\frac{C_0}{C}\right) = K_1\, t \quad (4.3)$$

The pseudo second-order kinetics curves were plotted in between t/C and time (min) and by equating the intercept of linearly fitted data points of the experimental results using the below relation the value of second order rate constant (K_2) can be calculated:

$$\frac{t}{C} = \frac{1}{K_2 {C_0}^2} + \frac{t}{C_0} \quad (4.4)$$

Figure 4.9 a represents the pseudo first order reaction kinetics for MB dye and N-phenol which is obtained by linear fitting the data points and kept in the intercept at zero. The valve of the first order rate constant K_1 is 0.1457 and 0.0894 min^{-1} while the quality of fitting (R^2) is 0.87 and 0.91 for MB dye and N-phenol, respectively. Similarly, figure 4.9 b show the pseudo

second order reaction kinetics which was plotted by linearly fitting of the obtained data points from the t/C and time curve but in this case the intercept was not at zero. Herein, the second order rate constant (K_2) values is 0.0432 and 0.4792 min^{-1}, R^2 is 0.96 and 0.97 for MB dye and N-phenol, respectively. To check the applicability of the model we check the quality of fitting. So, based on the quality of fitting (R^2), it has been observed that adsorption of MB dye and N-phenol followed pseudo second order kinetics i.e. chemisorption as shown in Figure 4.9 b.

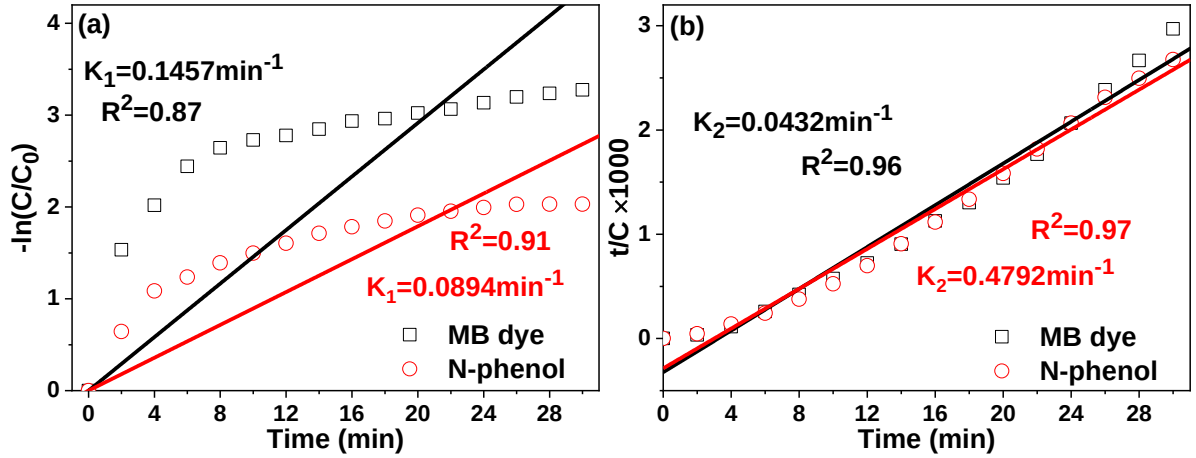

Figure 4.9: Adsorption kinetics of MB dye and N-phenol (a) pseudo first order and (b) pseudo second order reaction kinetics.

Thereafter, the photodegradation process was carried out in which both of the solutions were irradiated under CFL lamp and variation of their concentration was measured after each 30 min interval. Significant degradation percentage was calculated similarly to that of adsorption efficiency. The photodegradation of MB dye and N-phenol has been observed in time range of 120 min as shown in Figure 4.10 in which the MB dye was degraded about 49 % and N-phenol is around 42 %. The observed discoloration trend of both the organic effluents under visible radiations confirmed the photodegradation rather dye sensitization [16].

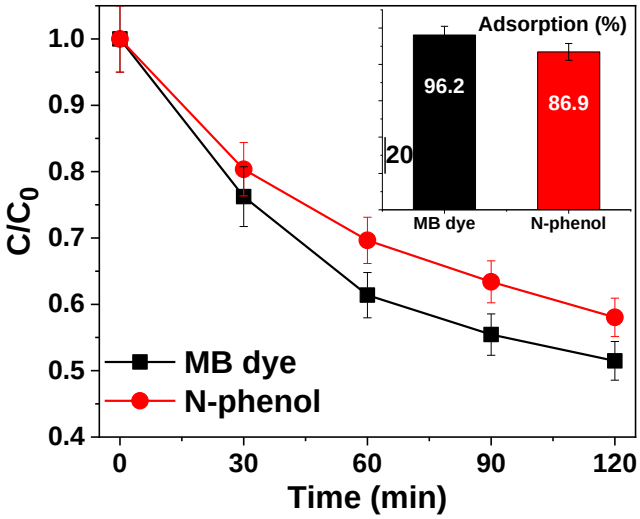

Figure 4.10: Photodegradation of MB dye and N-phenol: C/C_0 vs. time with adsorption of adsorbate on the synthesized catalyst (inset).

Figure 4.11 a show the pseudo first order reaction kinetics for MB dye and N-phenol. The valve of the first order rate constant K_1 for photodegradation is 0.0063 and 0.0049 min^{-1} and the quality of fitting (R^2) is 0.96 and 0.97 for MB dye and N-phenol, respectively. Similarly, figure 4.11 b show the pseudo second order reaction kinetics in which the value of the second order rate constant K_2 is 8.7413 and 9.7158 min^{-1}, R^2 is 0.98 and 0.98 for MB dye and N-phenol, respectively. Therefore, rate kinetics suggested the simultaneous action of pseudo first and second order law during the photodegradation of MB dye and N-phenol [17], respectively .

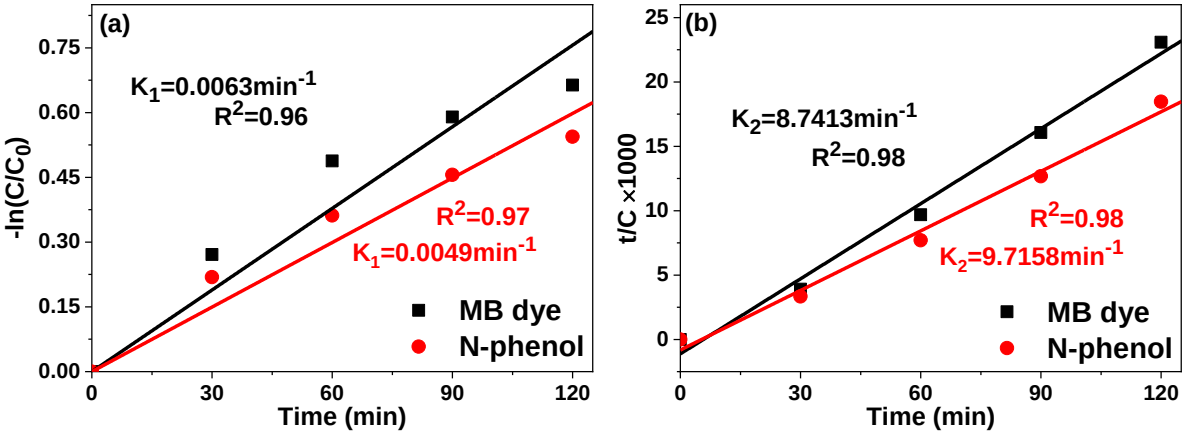

Figure 4.11: Photodegradation (a) pseudo first order and (b) pseudo second order reaction kinetics of MB dye and N-phenol.

Figure 4.12 represents the schematic diagram of photodegradation mechanism which is responsible for both MB dye and N-phenol. When the solution was exposed to light the electron get excited and jumps to conduction band. Photo excited electrons-holes participates in the formation of superoxide onion radical ($O_2^{\cdot -}$) and hydroxyl radical ($OH^{\cdot}$) at conduction and valance band, respectively. Thereafter, these newly generated hydroxyl radical and superoxide onion radical then decompose the toxic organic molecules efficiently and produce rather any non-toxic organic molecules or CO_2+H_2O.

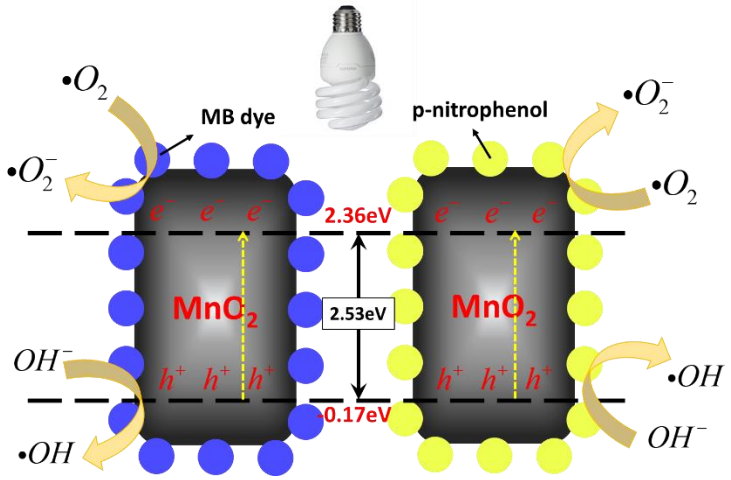

Figure 4.12: Schematic representation of photodegradation mechanism with MnO_2.

From the previous results, we can conclude that there is no sole effect of dye sensitization rather the dye molecules have been degraded by the excitation of photocatalyst under visible light irradiation. Further, the photo-chemical reaction kinetics has been understood considering MB dye with variable concentrations for adsorption and photodegradation which will be discussed as follows:

4.7 Effect of concentration on the adsorption and its kinetics

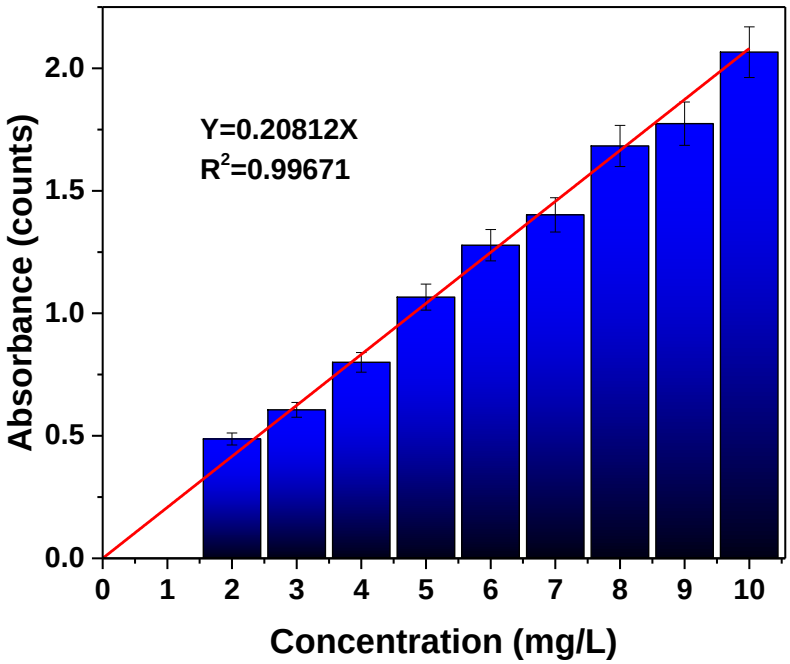

Figure 4.13: Calibration graph between the absorbance and concentration of MB dye.

In consideration to understand the involved kinetics in adsorption of MB dye on the surface of photocatalyst i.e. MnO_2, the photocatalytic adsorption process was observed with different concentration of MB dye (2.0, 3.0, 4.0, 5.0, 6.0, 7.0, 8.0, 9.0 and 10.0 mg/L) for 30 min with a sampling interval of 2.0 min. Here, initial dye solution was used for the determination of instrument response with respect to different concentration of solution. Prior to understand the adsorption process, figure 4.13 represents the calibration curve of the system in which absorbance (Y) varies linearly with respect to concentration (X) of dye solution which can be described as :

$$Y = 0.20812X \quad (4.5)$$

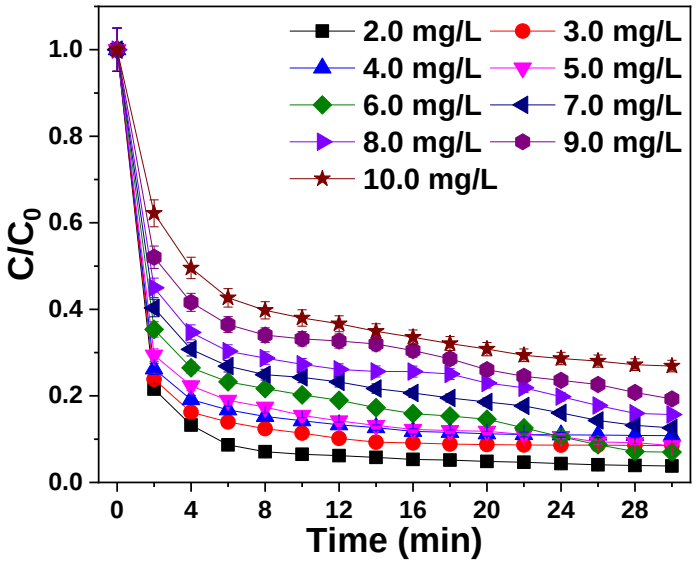

Figure 4.14: C/C_0 vs. reaction time graph for the adsorption of MB dye using as-synthesized MnO_2 at different dye concentration.

Thereafter, figure 4.14 represents the relative change in the concentration (C/C_0 vs. time) for the adsorption of MB dye on as-synthesized MnO_2 in dark chamber. The results exhibited that the absorbance efficiency was highly affected by the concentration of the dye solution. The adsorption effeciency first increase with the concentration to 96.2, 83.6, 86.0, 90.1 and 94.6 % by increasing the dye concentration from 2.0 - 6.0 mg/L (respectively) and then decreased gradually to 91.3, 90.6, 89.0, 68.8 % by increasing dye concentration to 7.0, 8.0, 9.0 and 10.0 mg/L, respectively. The observed decrement of the adsorption efficiency might be associated to the inter-molecular repulsion between dye molecules at higher concentration of dye solution which restricted the absorption capacity of the photocatalyst. The adsorption efficiency was calculated for each concentration as shown in figure 4.15 which results the maximum absorption rate at 2.0 mg/L (96.2 %) and then at 6.0 mg/L (94.6 %).

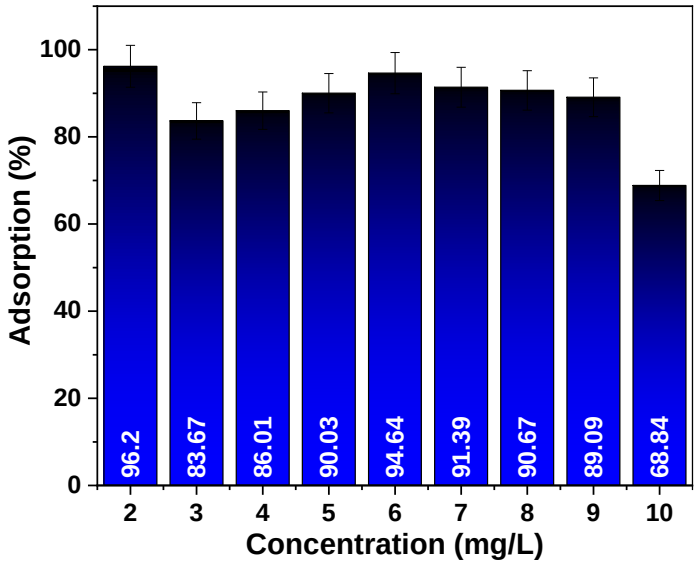

Figure 4.15: Histogram of adsorption efficiency of MB dye at different concentration.

Such a high adsorption of dye molecule (as observed previously) might be associated to different physical and chemical phenomenon which need to be understood prior to analyze photocatalytic degradation. Here, in order to understand the adsorption kinetics, different kinetic models were employed which have been discussed in following section.

4.7.1 Freundlich adsorption and langmuir adsorption model analysis

The freundlich and langmuir adsorption models are used to examine the obtained adsorption results for the adsorption of MB dye by MnO_2 catalyst. Freundlich adsorption model is an empirical relation between the concentration of the solute (MB dye) on the surface of the adsorbent (MnO_2) to the concentration of the solute in liquid with which it is adherent by multilayer adsorption [18]. While, to determine the equilibrium between the adsorbate (MB dye) and adsorbent (MnO_2), where the adsorbate adsorption is limited to monolayer adsorption, Langmuir adsorption isotherm is used [19]. To have better understanding about the nature of the interaction (adsorbent; MnO_2 and adsorbate; MB dye) and influence of dye concentration on adsorption process, the linearized forms of the Freundlich and Langmuir isotherms are used. The linearied form of freundlich and langmuir model are shown in equation (4.6) and (4.7), respectively,

$$\ln Q_e = \ln K_f + \frac{1}{n}\ln C_e \tag{4.6}$$

$$\frac{C_e}{Q_e} = \frac{1}{K_L} + \frac{\alpha_L}{K_L} C_e \tag{4.7}$$

where, C_e is the concentration (mg/L) of the dye solution, Q_e is amount of adsorbed dye at equilibrium (amount of adsorbed dye /mass of the catalyst; mg/g), K_f (freundlich constant) results the adsorption capacity,1/n is adsorption intensity, K_L and α_L are langmuir constants.

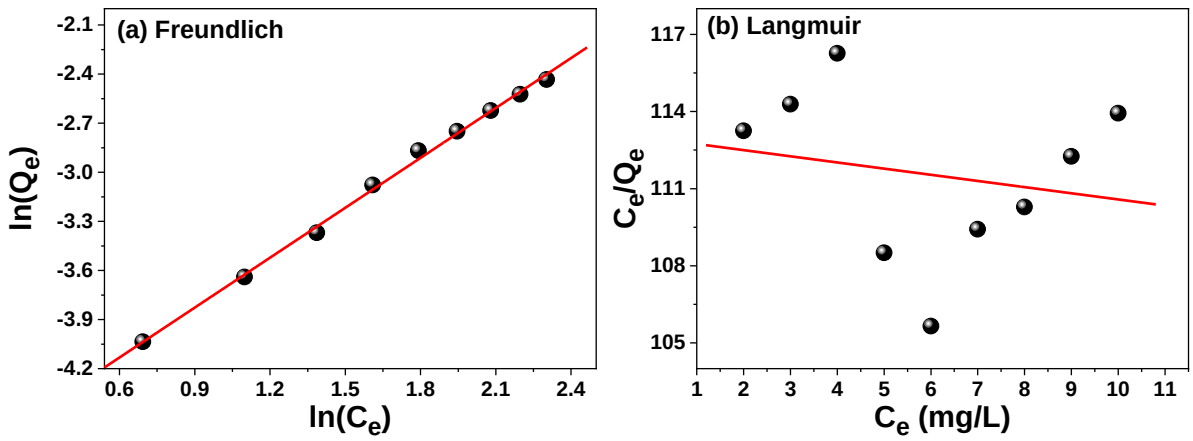

Figure 4.16: (a) Freundlich; and (b) Langmuir adsorption model.

A plot between $\ln(Q_e)$ and $\ln(C_e)$ is a straight line graph as shown in figure 4.16 (a), $\ln(K_f)$ and 1/n are the intercept and the slope of the graph and calculated values are shown in table 4.1. Figure 4.16 (b) represents a graph between C_e/Q_e and C_e for Langmuir adsorption model and the constant values are shown in table 5.1. From the obtained results, it can be illustrated that R^2 value of freundlich model is approaching to '1' (0.99) as compared to the langmuir model (0.09) which suggested that the adsorption process data is well fitted by freundlich adsorption model i.e. multi-layered adsorption of MB dye on the surface of MnO_2.

Table 4.1: Values of freundlich and langmuir constants.

Freundlich			**Langmuir**		
K_F	**1/n**	**R^2**	**K_L**	**α_L/K_L**	**R^2**
114.6724	1.01675	0.99684	0.0088	0.23976	0.09857

4.7.2 Pseudo first and second order kinetics analysis

For the adsorption kinetics study, the pseudo first and second order kinetic models were also fitted in experimental data points. Figure 4.17 (a) and (b) represent the pseudo first ($-\ln(C/C_0)$ vs. time) and second (t/C vs. time) order kinetics of adsorption with different concentration of MB dye on photocatalyst. The value of first and second order rate constants were calculated and tabulated in table 4.2 with the quality of fitting (R^2) and adsorption percentage. Therefore, for the kinetics study of adsorption of MB dye the reaction followed pseudo second order kinetics which indicates that the reaction is more inclined towards chemisorption as in this case the value of R^2 is closer to 1 than physisorption (pseudo first order kinetics). Basically, in case of physisorption the dye molecule is attached to the surface of the catalyst with weak vander waal force of attraction while in case of chemisorption, the strong chemical bond is formed between the dye molecule and the surface of the catalyst. Figure 4.18 (a) and (b) shows the trend of pseudo first and second order rate constant (K_1, K_2) for adsorption with varying concentration of the dye. The value of K_1 was decreasing almost linearly with the increase in the concentration while in case of K_2 there is no such kind of trend and show the highest value at 4.0 mg/L and lowest at 6.0 mg/L concentration.

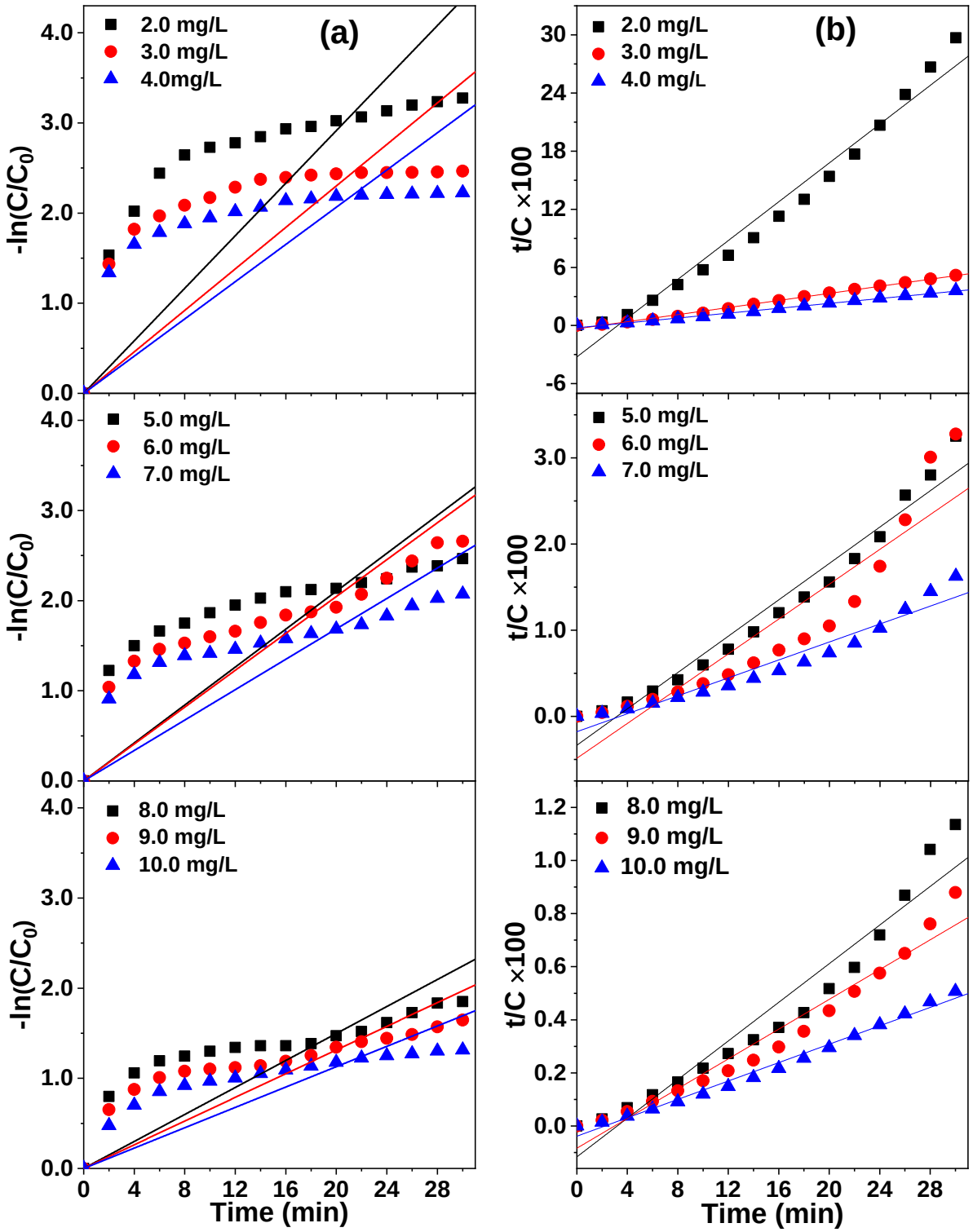

Figure 4.17: (a) Pseudo first order and (b) second order kinetics fitted graph of photocatalytic adsorption with different concentration of MB dye.

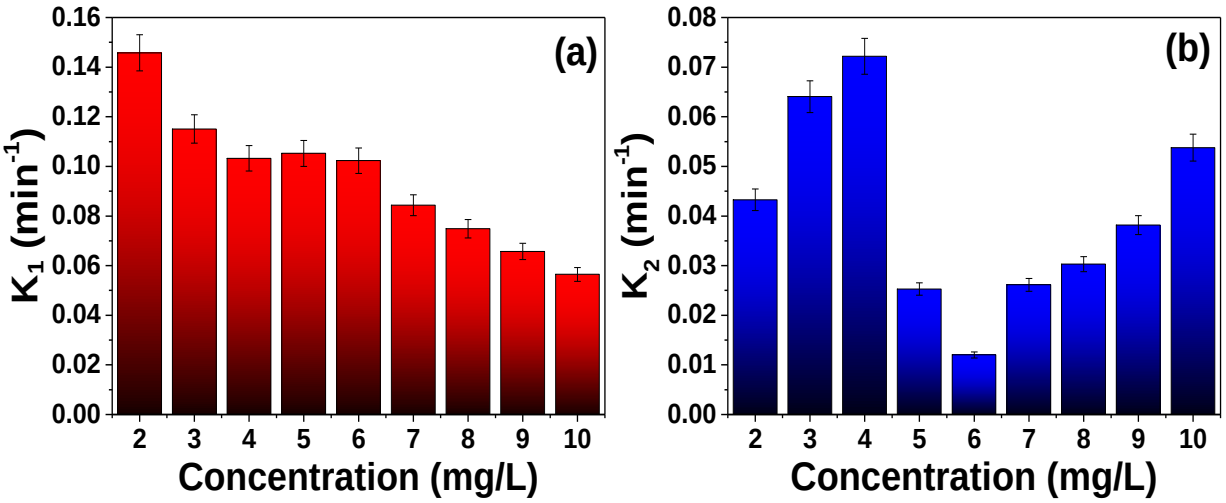

Figure 4.18: Comparative bar chart of rate constants ((a) K_1; and (b) K_2) with different dye concentration.

Table 4.2: Photocatalytic adsorption kinetic constants for MB dye on MnO_2 at different concentration of dye with adsorbed dye percentage.

Concentration (mg/L)	Adsorption %	First order		Second order	
		K_1 (min^{-1})	R^2	K_2 (min^{-1})	R^2
2.0	96.20	0.1457	0.8710	0.0432	0.9684
3.0	83.67	0.1150	0.8551	0.0640	0.9918
4.0	86.01	0.1032	0.8549	0.0721	0.9878
5.0	90.03	0.1052	0.8831	0.0252	0.9591
6.0	94.64	0.1022	0.9275	0.0119	0.8466
7.0	91.39	0.0843	0.9018	0.0261	0.9374
8.0	90.67	0.0748	0.8986	0.0302	0.9362
9.0	89.09	0.0657	0.9105	0.0381	0.9551
10.0	68.84	0.0564	0.9073	0.0537	0.9863

4.8 Effect of concentration on the photodegradation of MB dye and its kinetics

After the adsorption of the dye on the photocatalyst, the solution was exposed under visible light irradiation i.e. house-hold CFl lamp (85 W) for 120 min. Figure 4.19 represents the C/C_0 vs. irradiation time curve for the photodegradation of MB dye by as-synthesized MnO_2 nanopowder with different dye concentrations. The curve follow the same trend as that of adsorption i.e. the results show the highest degradation rate at 2.0 mg/L and lowest degradation rate at 10.0 mg/L as shown in figure 4.20.

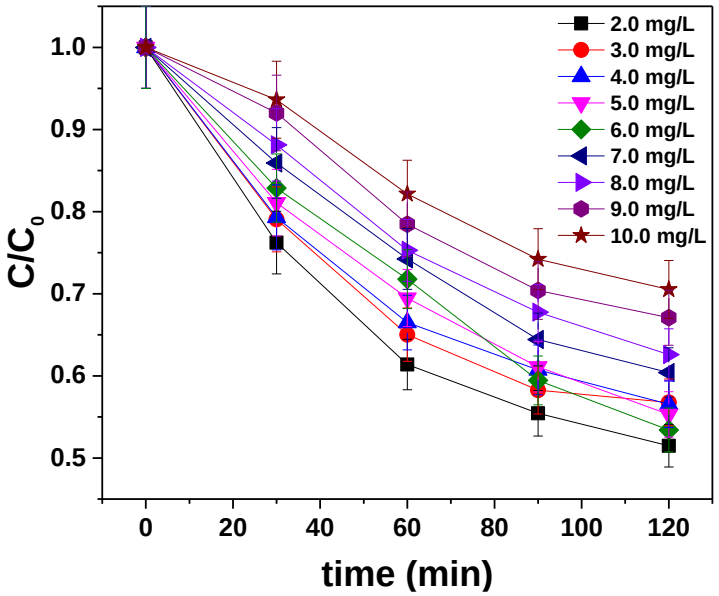

Figure 4.19: C/C_0 vs. reaction time graph of photocatalytic degradation of MB dye with prepared MnO_2 at different dye concentration (mg/L).

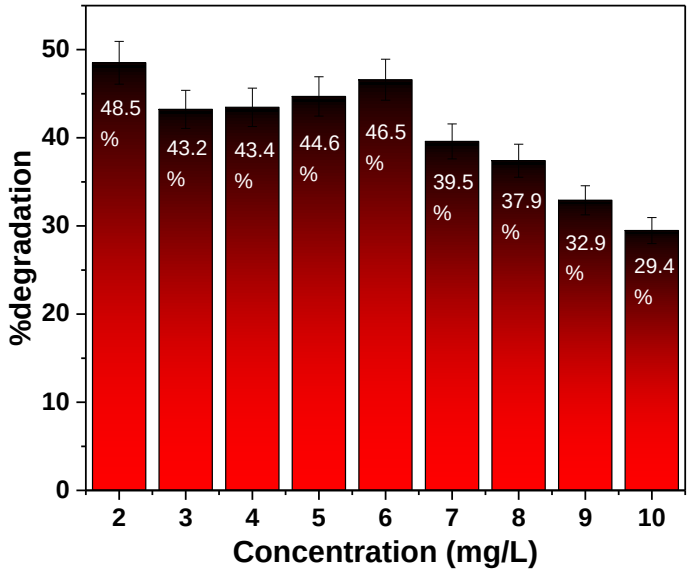

Figure 4.20: Photodegradation efficiency of MB dye on MnO_2 after 120 min.

Figure 4.20 represents the degradation (%) with the increase in the concentration of dye. No significant decrement of degradation efficiency has been observed by increasing the dye concentration (2.0 to 6.0 mg/L) and then decreased gradually to 39.5, 37.9, 32.9 and 29.4 % by increasing dye concentration to 7.0, 8.0, 9.0 and 10.0 mg/L, respectively. Such decrease in the photodegradation efficiency due to the increase in the dye concentration might be associated to the decreased adsorption of dye molecules and hinderance to light penetration throught the dye solution due to higher content of un-adsorbed dye. Also, the formation of hydroxyl radicals reduces with the increase in dye concentration as the dye molecule occupy the active sites of the catalysts [20,21].

4.8.1 Pseudo first and second order kinetics for photodegradation

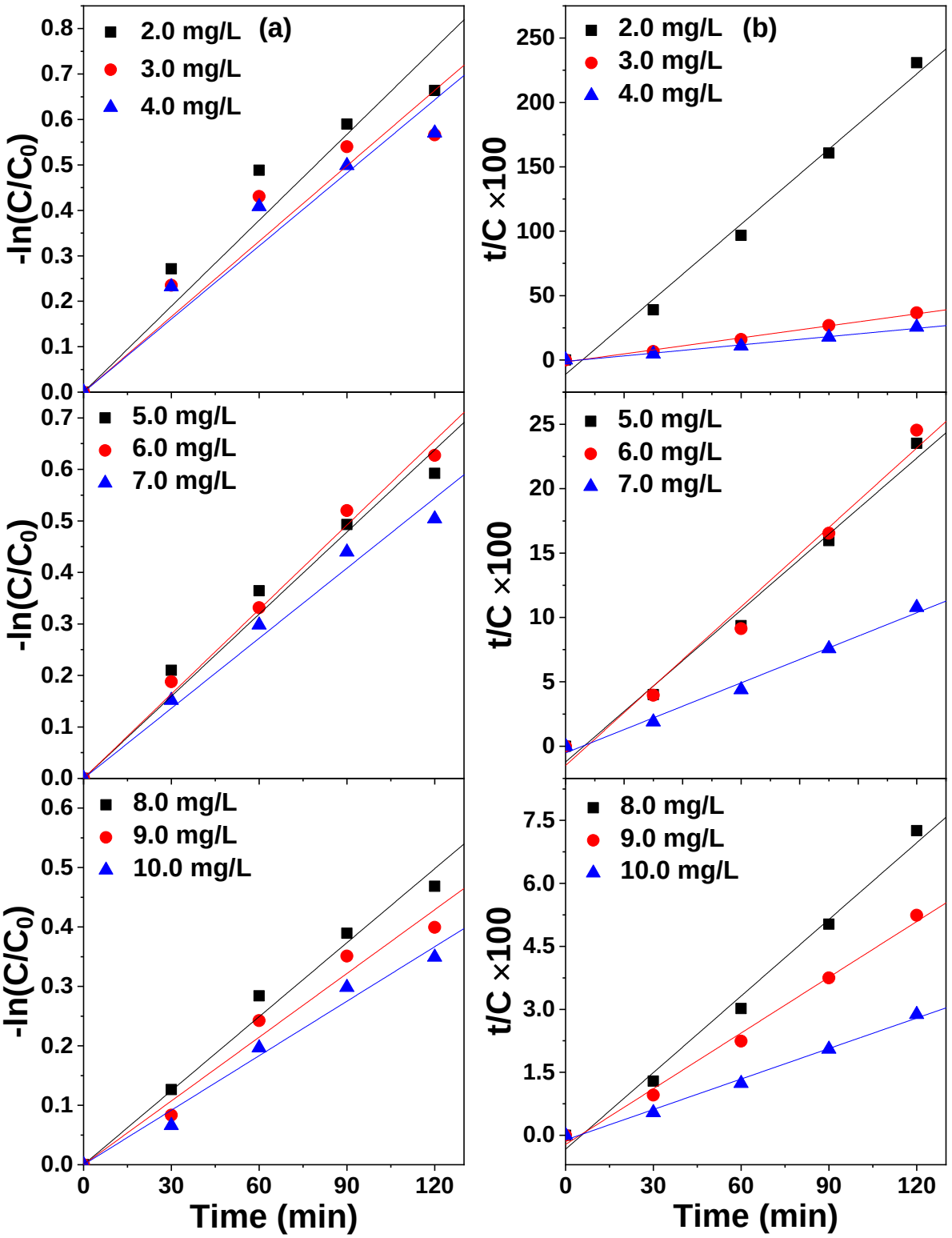

Figure 4.21: (a) Pseudo-first-order and (b) second order kinetics fitted graph of photocatalytic degradation with different concentration of MB dye, the same line indicates the line fitting for each concentration.

Further, the figure 4.21 represents the pseudo first and second order kinetics for photodegradation of MB dye and table 4.3 shows the rate constants with degradation percentage at different concentration which clearly indicates the simultaneous action of physisorption (pseudo first) and chemisorption (second order) during the photodegradation of MB dye. Figure 4.22 (a) and (b) show the varation of rate constants (K_1 and K_2) with the different concentration of MB dye in which both K_1 and K_2 vary lineraly with the increase in the concentration of MB dye.

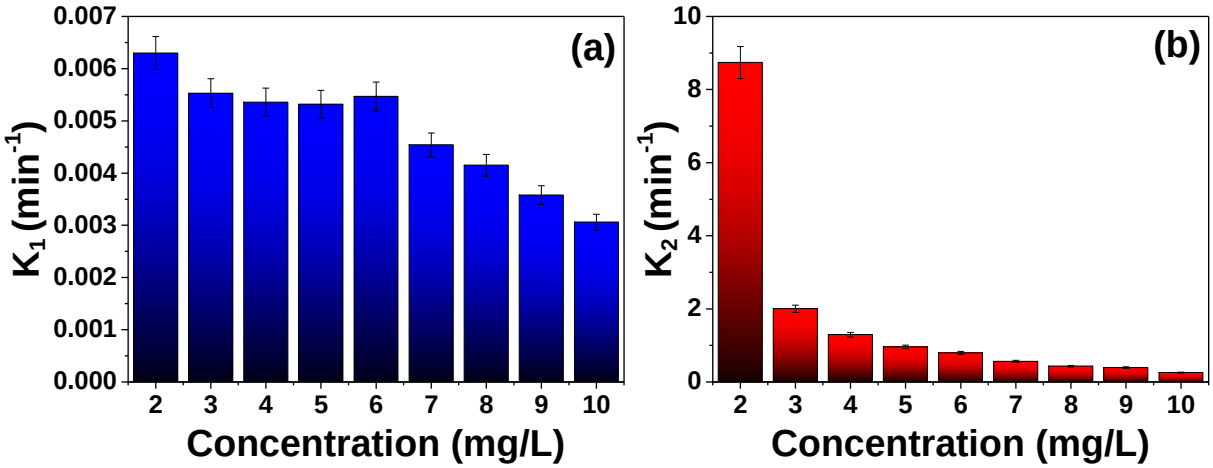

Figure 4.22: Comparison between rate constant of degradation with different concentration of MB dye (mg/L) (a) first order rate constant (K_1) vs. concentration, (b) second order rate constant (K_2) vs. concentration.

Table 4.3: Photodegradation kinetic constants for MB dye on as-synthesized MnO_2 at different concentration of dye with degraded dye percentage.

Concentration (mg/L)	Degradation %	First order		Second order	
		K_1 (min^{-1})	R^2	K_2 (min^{-1})	R^2
2.0	48.52	0.0063	0.9683	8.7403	0.9863
3.0	43.22	0.0055	0.9621	2.0025	0.9910
4.0	43.45	0.0053	0.9714	1.2942	0.9885
5.0	44.69	0.0053	0.9888	0.9577	0.9811
6.0	46.59	0.0054	0.9966	0.7950	0.9733
7.0	39.59	0.0045	0.9921	0.5646	0.9852
8.0	37.40	0.0041	0.9937	0.4307	0.9865
9.0	32.91	0.0035	0.9888	0.3939	0.9900
10.0	29.47	0.0030	0.9916	0.2559	0.9909

4.9 Effect of pH on the adsorption of MB dye on MnO_2

The effect of the pH for the adsorption of the MB dye on the surface of MnO_2 was studied using different concentration (2.0, 5.0, 7.0 and 10.0 mg/L) of dye solution with same amount of MnO_2 (10 g in 100 mL).

4.9.1 Low pH effect on adsorption of MB dye

In order to understand the effect of low pH, the normal pH of MB dye i.e. 5.0 was decreased by adding HCl to the MB dye solution till pH reaches to 2.0 and then the solution was kept in dark chamber for 30 min. Figure 4.23 represents the C/C_0 variation of adsorbed dye on the surface of MnO_2. After 30 min, 99.8% MB dye was absorbed on the surface of catalyst.

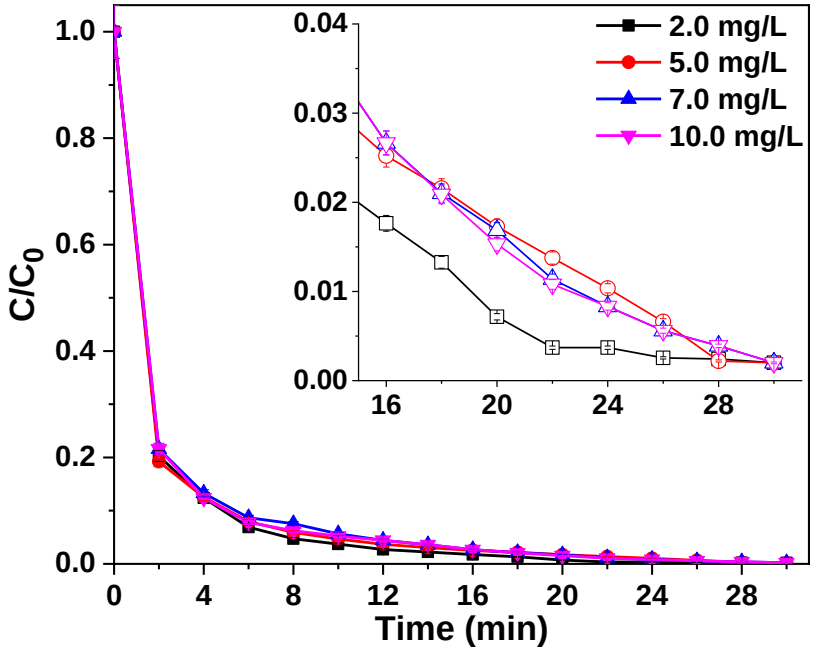

Figure 4.23: C/C_0 vs. reaction time graph for the adsorption of MB dye on MnO_2 at pH=2.0.

4.9.2 Pseudo first and second order kinetics for the adsorption of MB dye (low pH = 2.0)

Figure 4.24 represents the pseudo first and second order kinetics for the adsorption of MB dye on the surface of MnO_2 and the value of the constants for both the models are given in table 5.4. Based on the value of R^2, the experimental data for the low pH adsorption was best fitted with pseudo first order law suggesting the attachment of MB molecule to MnO_2 through weak Vander Waal forces (physisorption).

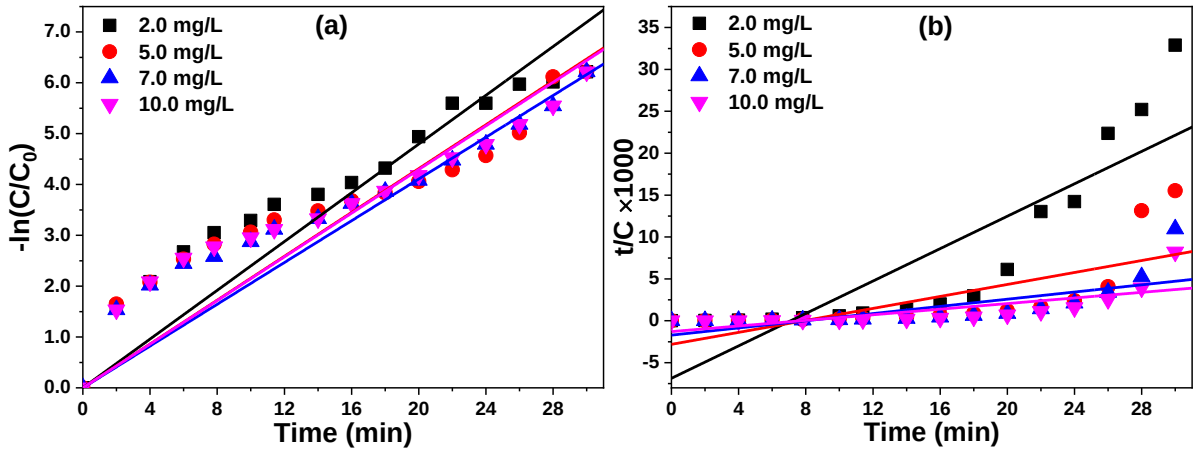

Figure 4.24: (a) Pseudo first; and (b) second order graph for adsorption of MB dye at pH=2.

4.9.3 High pH effect on adsorption of MB dye

Similarly, the effect of high pH was studied by adding NaOH solution (1M) to the dye solution till the pH of the solution reaches to 10.0 and then the solution was kept in dark chamber for 30 min. Figure 4.25 represents C/C_0 and reaction time graph for the absorbance at pH 10 which shows a decrease in the absorbance rate with the increase in concentration but the absorbance rate at each concentration is small then that of the natural pH of the MB dye.

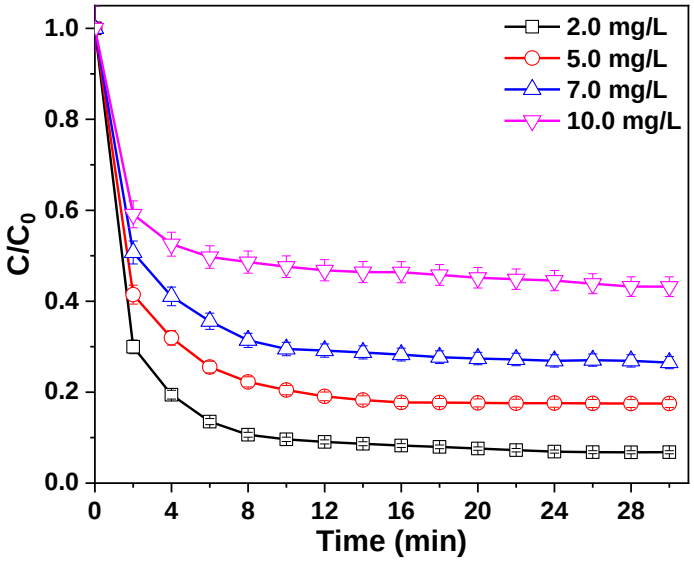

Figure 4.25: C/C_0 vs. reaction time graph for the adsorption of MB dye on MnO_2 at pH=10.

4.9.4 Pseudo first and second order kinetics for the high adsorption of MB dye

Pseudo first and second order kinetics models were also analyzed to understand the adsorption kinetics at high pH compared to the natural and low pH of MB dye solution. Figure 4.26 represents the pseudo first and second order kinetics models for the adsorption of MB dye on the surface of the catalyst and the value of the rate constants are listed in table 4.4 with adsorption percentage with varying concentration. Based on the fitting of the experimental datapoints, the results indicated that the data was well fitted with the pseudo second order

kinetics model i.e. chemisorption indicating the formation of chemical bonds between MnO_2 and MB molecule with higher rate and lower efficiency at higher (10.0 mg/L) concentration of dye solution.

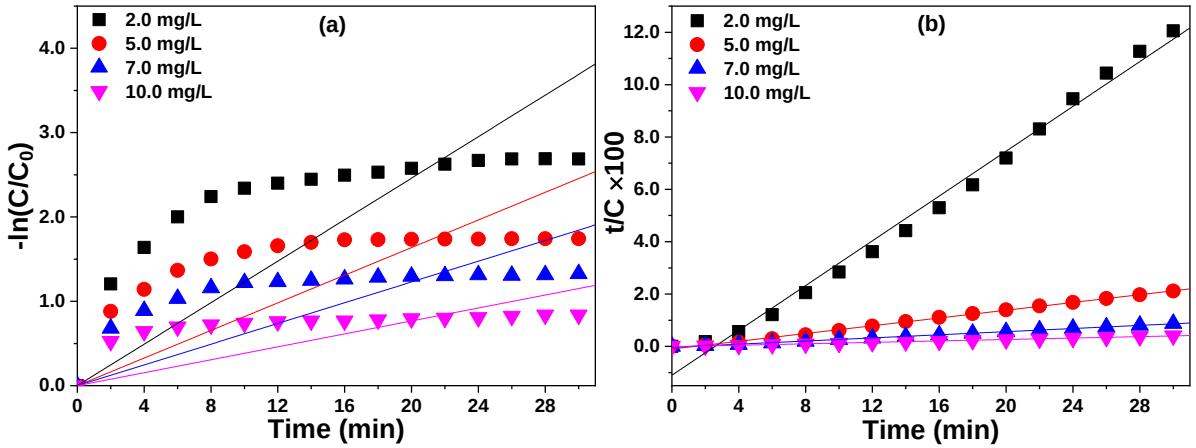

Figure 4.26: (a) Pseudo first order; and (b) pseudo second order kinetics for adsorption of MB dye on MnO_2 at pH=10.

Table 4.4: Adsorption kinetic constants at low and high pH for MB dye on as-synthesized MnO_2 at different concentration of dye with adsorbed dye percentage.

Concentration (mg/L)	Low pH (2)				
	Adsorption (%)	First order		Second order	
		K_1 (min^{-1})	R^2	K_2 (min^{-1})	R^2
2.0	99.5	0.2402	0.9678	0.0007	0.7295
5.0	99.7	0.2159	0.9614	0.0004	0.4811
7.0	99.8	0.2136	0.9702	0.0003	0.5051
10.0	99.8	0.2149	0.9666	0.0002	0.5092
	High pH (10)				
2.0	81.2	0.1229	0.8709	0.0678	0.9872
5.0	78.4	0.0818	0.8537	0.0944	0.9970
7.0	79.5	0.0614	0.8515	0.1733	0.9982
10.0	74.6	0.0383	0.8352	0.3205	0.9984

4.10 Effect of pH on the photodegradation of MB dye

After the establishment of adsorption-desorption equilibrium, the same solution was kept under visible light irradiation and the experiment was set for 120 min. Since, the adsorption of MB dye can be altered by varying the surface charge of dye molecule (pH of dye solution), it has been well-observed that the degradation efficiency can also be affected by the pH of the solution [22]. Here, nearly 100% dye has been adsorbed on the surface of catalyst at low pH i.e. 2.0. Therefore, the effect of high pH i.e. 10.0 on the photodegradation efficiency of MB dye was monitored.

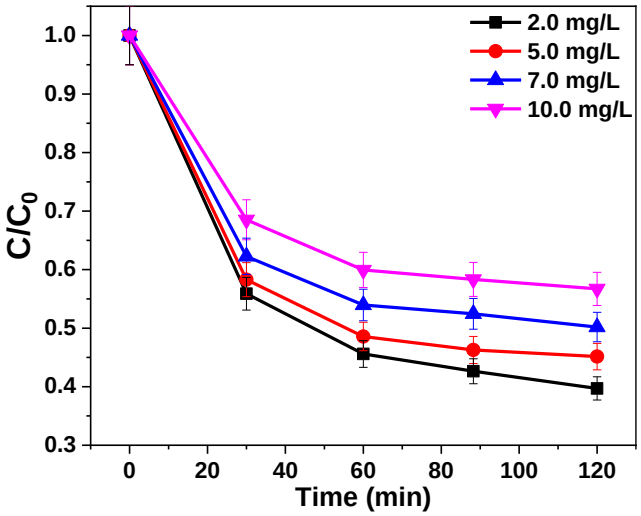

Figure 4.27: C/C_0 vs. reaction time graph for the degradation of MB dye on MnO_2 at pH=10.

Figure 4.27 represents the C/C_0 vs. reaction time graph for the degradation of the MB dye at pH 10 with varying concentration of MB dye. It illustrated the enhanced degradation efficiency of the system as compared to natural pH of dye solution even at relatively lower adsorption of MB molecule at pH = 10.0. Figure 4.28 represents the pseudo first and second order kinetics models for the degradation of MB dye on the surface of the catalyst, respectively and the value of the rate constants are mentioned in the table 4.5 with degradation percentage varying with concentration. It has been observed that chemisorption (pseudo second order kinetics) controlled the photodegradation of MB dye with higher rate constants as compared to natural pH of dye solution.

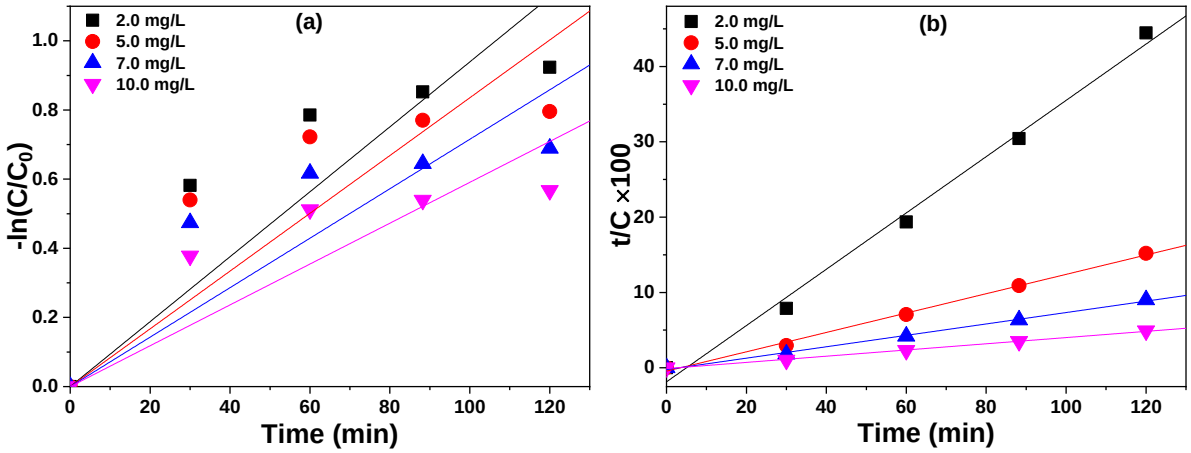

Figure 4.28: (a) Pseudo first order; and (b) pseudo second order kinetics for adsorption of MB dye on MnO_2 at pH=10.

Table 4.5: degradation kinetic constants at high pH for MB dye on as-synthesized MnO_2 at different concentration of dye with degraded dye percentage.

Concentration (mg/L)	pH 10				
	Degradation (%)	First order		Second order	
		K_1 (min^{-1})	R^2	K_2 (min^{-1})	R^2
2.0	60.2	0.0093	0.9106	1.1578	0.9873

5.0	59.8	0.0083	0.8910	0.7261	0.9954
7.0	49.8	0.0071	0.8904	0.5953	0.9959
10.0	43.2	0.0059	0.8949	0.4822	0.9972

Reference

[1] Q. Liu, S. Ji, Enhanced Cycleability of Amorphous MnO2 by Covering on α-MnO2 Needles in an Electrochemical Capacitor, Materials (Basel). 10 (2017) 988. doi:10.3390/ma10090988.

[2] H.Q. Wang, G.F. Yang, Q.Y. Li, X.X. Zhong, F.P. Wang, Z.S. Li, Y.H. Li, Porous nano-MnO2: Large scale synthesis via a facile quick-redox procedure and application in a supercapacitor, New J. Chem. 35 (2011) 469–475. doi:10.1039/c0nj00712a.

[3] C. Wan, L. Yuan, H. Shen, Effects of Electrode Mass-loading on the Electrochemical Properties of Porous MnO 2 for Electrochemical Supercapacitor, Int. J. Electrochem. Sci. 9 (2014) 4024–4038.

[4] S. Devaraj, N. Munichandraiah, Effect of crystallographic structure of MnO2 on its electrochemical capacitance properties, J. Phys. Chem. C. 112 (2008) 4406–4417. doi:10.1021/jp7108785.

[5] B. Gnana Sundara Raj, A.M. Asiri, A.H. Qusti, J.J. Wu, S. Anandan, Sonochemically synthesized MnO2nanoparticles as electrode material for supercapacitors, Ultrason. Sonochem. 21 (2014) 1933–1938. doi:10.1016/j.ultsonch.2013.11.018.

[6] N. Kaur, R.A. Mir, O.P. Pandey, Electrochemical and optical studies of facile synthesized molybdenum disulphide (MoS2) nano structures, J. Alloys Compd. 782 (2019) 119–131. doi:10.1016/j.jallcom.2018.12.145.

[7] X. Zhang, M. He, P. He, C. Li, H. Liu, X. Zhang, Y. Ma, Ultrafine nano-network structured bacterial cellulose as reductant and bridging ligands to fabricate ultrathin K-birnessite type MnO2nanosheets for supercapacitors, Appl. Surf. Sci. 433 (2018) 419–427. doi:10.1016/j.apsusc.2017.10.053.

[8] M.I. Said, A.H. Rageh, F.A.M. Abdel-Aal, Fabrication of novel electrochemical sensors based on modification with different polymorphs of MnO2nanoparticles. Application to furosemide analysis in pharmaceutical and urine samples, RSC Adv. 8 (2018) 18698–18713. doi:10.1039/c8ra02978d.

[9] P. Kolhe, R.M. Kannan, Improvement in ductility of chitosan through blending and copolymerization with PEG: FTIR investigation of molecular interactions, Biomacromolecules. 4 (2003) 173–180. doi:10.1021/bm025689+.

[10] G. Wang, Q. Tang, H. Bao, X. Li, G. Wang, Synthesis of hierarchical sulfonated graphene/MnO2/polyaniline ternary composite and its improved electrochemical performance, J. Power Sources. 241 (2013) 231–238. doi:10.1016/j.jpowsour.2013.04.122.

[11] A. Gupta, O.P. Pandey, Visible irradiation induced photodegradation by NbC/C nanocomposite derived from smoked cigarette litter (filters), Sol. Energy. 163 (2018) 167–176. doi:10.1016/j.solener.2017.12.033.

[12] A.S. Vig, A. Gupta, O.P. Pandey, Efficient photodegradation of methylene blue (MB) under solar radiation by ZrC nanoparticles, Adv. Powder Technol. 29 (2018) 2231–2242. doi:10.1016/j.apt.2018.06.007.

[13] C. Wang, F. Yu, M. Zhu, C. Tang, L. Dong, B. Dai, Synthesis of Both Powdered and Preformed MnOx − CeO2 − Al2O3 Catalysts by Self-Propagating High-Temperature Synthesis for the Selective Catalytic Reduction of NOx with NH3, ACS Omega. 3 (2018) 5692–5703. doi:10.1021/acsomega.7b01286.

[14] G. Definitions, Reporting Physisorption Data for Gas/Solid Systems, IUPAC Recommandations. 37 (2008) 1217–1230. doi:10.1002/9783527610044.hetcat0065.

[15] E. Saputra, S. Muhammad, H. Sun, H.M. Ang, M.O. Tade, S. Wang, Different Crystallographic One-dimensional MnO2 Nanomaterials and Their Superior Performance in Catalytic Phenol Degradation, Environ. Sci. Techonolgy. 47 (2013) 5882–5887. doi:10.1021/es400878c.

[16] J. Diaz-angulo, I. Gomez-bonilla, C. Jimenez-tohapanta, M. Mueses, M. Pinzon, F. Machuca-martinez, Visible-light activation of TiO2 by dye-sensitization for degradation of pharmaceutical compounds, Photochem. Photobiol. Sci. (2018). doi:10.1039/c8pp00270c.

[17] M. Mittal, M. Sharma, O.P. Pandey, UV-Visible light induced photocatalytic studies of Cu doped ZnO nanoparticles prepared by co-precipitation method, Sol. Energy. 110 (2014) 386–397. doi:10.1016/j.solener.2014.09.026.

[18] F. Kano, Fractal model for adsorption on activated carbon surfaces: Langmuir and Freundlich adsorption, Surf. Sci. 467 (2000) 131–138. doi:10.1016/S0039-6028(00)00730-5.

[19] B.E. Reed, M.R. Matsumoto, Modeling Cadmium Adsorption by Activated Carbon Using the Langmuir and Freundlich Isotherm Expressions, Sep. Sci. Technol. 28 (2006) 2179–2195. doi:10.1080/01496399308016742.

[20] K. Mamun, R. Asw, K. Fahmida, Parameters affecting the photocatalytic degradation of dyes using TiO 2 : a review, Appl. Water Sci. 7 (2015) 1569–1578. doi:10.1007/s13201-015-0367-y.

[21] T. Santhi, S. Manonmani, T. Smitha, REMOVAL OF METHYL RED FROM AQUEOUS SOLUTION BY ACTIVATED CARBON PREPARED FROM THE Annona squmosa SEED BY ADSORPTION, Chem. Eng. Res. Bull. 14 (2010) 11–18. doi:10.3329/cerb.v14i1.3767 1.

[22] P. Ji, J. Zhang, F. Chen, M. Anpo, Study of adsorption and degradation of acid orange 7 on the surface of CeO 2 under visible light irradiation, Appl. Catal. B Environ. 85 (2009) 148–154. doi:10.1016/j.apcatb.2008.07.004.

5. Conclusion

In this study, MnO_2 nanopowder has been synthesized through a facile single step sonochemical route through the reduction of $KMnO_4$ with PEG. XRD, UV–visible spectroscopy and TEM results confirmed the formation of nanocrystalline network of MnO_2 with ultra-small crystallites (∼2-3 nm) having 2.53 eV optical band gap which is calculated using tauc plot. FTIR spectroscopy suggested the presence of MnO_6 octahedra as basic constituent with different vibrating Mn-O functional groups and BET study revealed the mesoporous characteristics of prepared MnO_2 with high surface area about 104 m^2/g and total pore volume 0.3901 cm^3/g. Further, adsorption study revealed the adsorption of MB dye and p-nitrophenol has been saturated in 30 min with 96 and 86% efficiency (respectively) following chemisorption kinetics. Photodegradation of both the molecules under household CFL lamp has been observed with ∼50 and ∼42% efficiency through the simultaneous physi- and chemisorption kinetics. Further, adsorption and photodegradation of MB dye with prepared MnO_2 was also studied with varying concentration (2.0, 3.0, 4.0, 5.0, 6.0, 7.0, 8.0, 9.0 and 10.0 mg/L) and also at different pH values (2.0, 5.0, 7.0, 10.0 mg/L at 2.0 and 10.0 pH), it has been found that there is increase in the adsorption and degradation of MB dye from 3.0 to 6.0 mg/L and afterwards the adsorption and the degradation both started decreasing. Moreover, adsorption of MB dye was maneuvered by chemisorption phenomenon while, its degradation exhibited simultaneous effect of physisorption and chemisorption.

6. Future scope

MnO_2 nanoparticles can also be synthesized by using different manganese sources in which synthesized parameter like temperature, time and molar ratio can be optimized for different morphologies. In our study, we have studied photocatalytic performance of undoped MnO_2 nanoparticles but the effect of different doping of cationic/anionic elements can also be studied. MnO_2 nanoparticles can also be synthesized at different pH values to study their effect on photocatalytic as well as optical properties. Herein, we work on the adsorption and photodegradation of the MB dye with same concentration of the catalyst, similarly other dyes like methylene orange, rhodamine blue can also be used for used for degradation with different concentration the catalyst. MnO_2 is the potential candidate for photocatalytic and electrocatalytic applications, therefore its behavior can be studied for various HER, ORR, OER in acidic/basic medium and different photochemical reactions.

Physica B: Condensed Matter 564 (2019) 179–185

Contents lists available at ScienceDirect

Physica B: Condensed Matter

journal homepage: www.elsevier.com/locate/physb

Facile sono-chemical synthesis of nanocrystalline MnO_2 for catalytic and capacitive applications

Kajal Rajrana, Aayush Gupta, Rameez Ahmad Mir, O.P. Pandey*

Functional Materials Lab, School of Physics and Materials Science, Thapar Institute of Engineering and Technology, Patiala, 147004, India

ARTICLE INFO

Keywords:
MnO_2
Adsorption
Photodegradation
HER
EDLC

ABSTRACT

In this reported work, the potential application of MnO_2 nanopowder for photocatalytic and the electrocatalytic applications is explored. The MnO_2 nanopowder has been synthesized through sonochemical route using $KMnO_4$ and poly-ethylene glycol as the reducing agent. Structural and optical analysis (XRD, TEM, FTIR, XPS and UV–visible) confirmed the formation of nanocrystalline MnO_2 network. The adsorption and photocatalytic performance of synthesized MnO_2 was tested for degradation of methylene blue dye and p-nitrophenol (2 mg/L) under dark chamber and household CFL lamp exposure, respectively. The electrochemical studies in alkaline (0.5 M KOH) medium shows the electric double layer capacitance of 7.4 $mFcm^{-2}$ suggesting its potential application for energy storage devices. The synthesized compound exhibited excellent stability after 1000 CV cycles (~4% current loss) where Volmer reaction was observed as the rate determining step for the electrocatalytic hydrogen evolution reaction.

1. Introduction

The requirement of fresh and clean water is increasing continuously to cater the needs of society. At the same time, population pressure has led to development of many new industries. Among these industries like textile, pulp and paper, food leather, printing, etc. consume lot of fresh water and dispose of contaminated water into soil. In this process, every year about 800,000 tons of synthetic dyes (non-biodegradable, mutagenic and carcinogenic) are dumped into natural water resources causing severe damage to aquatic flora-fauna by depleting the dissolved oxygen in water. There are various physical, chemical and biological techniques to extract or degrade such organic effluents [1–6]. Among these, advanced oxidation process (AOP) is the most efficient degradation of organic pollutants and pesticides than other conventional techniques. The semiconductor photocatalysis is considered as a green approach and efficient process [7,8]. Due to photons-catalyst interaction, initially generated electron-hole pair participates in various photochemical reactions and generates highly reactive radicals ($\cdot OH^-$ and $\cdot O_2^-$) which further oxidize the pollutants to form mineral acids, CO_2 and H_2O [9,10].

Conventionally, semi-conducting and metallic compounds such as TiO_2, ZnO, CdS, ZnS, CeO_2 and ZrC are used for the same purpose as photocatalysts [11–16]. In recent years, a plateau has occurred in the field of applicability of ZnO and TiO_2 as photocatalyst and their excitation under UV-region (3% of solar spectrum) limits their usability. However, their applicability has been enhanced by tailoring the optical band gap of the photocatalyst by doping or forming a heterostructure, but their performance has some limitations [17–19]. Among all, MnO_2 exhibits non-toxicity, excellent ambient chemical and physical properties due to their polymorphic nature [17,20–25]. Conventionally, it is being used as cathode material as electrochemical capacitor in fuel cells due to its large initial capacity [17,24,26,27]. Its heterostructure with a variety of compounds such as CNTs [28], graphene [29], polyaniline [30], Ag/rGO [31] enhanced the charge storage capacity of MnO_2 due to better transfer of electrons [32].

Further, excitation in the visible light region and n-type semiconducting properties induce its applicability as a photocatalyst [27,33]. In MnO_2, it is attributed that d-d electronic transitions are known to occur because of partially filled d-orbitals during irradiation thus, it can work as an effective photocatalyst without any doping [34]. High specific surface area and sufficiently active sites of MnO_2 are the most important parameters for adsorption process [35]. With these properties, considerable redox activity of MnO_2 makes it suitable for photocatalytic degradation. In literature, various studies have shown the adsorption and catalytic ability of MnO_2 alone as well as support of the other compounds to enhance their performance. Gheju et al. [36] and Wakeel et al. [37] proposed the use of MnO_2 for the removal of Cr^{4+} and Pb^{2+} from contaminated water through adsorption. Some

* Corresponding author.
E-mail address: oppandey@thapar.edu (O.P. Pandey).

https://doi.org/10.1016/j.physb.2019.04.002
Received 22 February 2019; Received in revised form 30 March 2019; Accepted 1 April 2019
Available online 02 April 2019
0921-4526/

research groups have also studied the photocatalytic behavior of MnO_2 and its heterostructure for the removal of different organic effluents without sufficient kinetic analysis and responsible mechanism [38–40]. Being highly efficient photocatalyst, the electrocatalytic application of MnO_2 for water splitting through HER for the production of renewable and green energy fuel widens its research area. MnO_2 has been studied for its capacitive behavior with its variety of morphologies and combinations with other compounds, its applicability as photocatalyst and catalytic kinetics is yet to be explored.

Considering these aspects, in this wok we report a facile route to synthesize nano-crystalline MnO_2 through single step sonochemical route to understand its adsorption, photo- and electro- catalytic kinetics. The novelty of this work is the synthesis route followed here. The ultrasonication process provide additional- vibrational energy to enhance the rate of chemical reaction which facilitate the rapid nucleation of fine particles. Moreover, ultrasonic irradiation enhances the reduction of $KMnO_4$ yielding MnO_2 through the pyrolysis of poly ethylene glycol (PEG) [41]. The capacitive behavior of synthesized MnO_2 has also been studied to understand the effect of structured network on the charge storage capacity.

2. Experimental

2.1. Synthesis of MnO_2 and characterization

MnO_2 nanopowder were prepared by the reduction of $KMnO_4$ (SD-fine chem Ltd) with polyethylene glycol (PEG) (Lab. Reagents & Fine Chemicals) through ultrasonication. Typically, 0.5 g of $KMnO_4$ was dissolved in 60 ml of distilled water (DW) followed by the addition of 5.5 g PEG in the solution with continuous stirring for 10–15 min at 60 °C. Thereafter, brown colored precipitates were obtained by sonication (LABMAN Scientific Instruments; 50 W; 220 V; 40 kHz) after 30 min. Then the solution was filtered and washed several times with DW and ethanol alternatively and dried in a vacuum oven at 70 °C for 12 h.

The crystallographic information was obtained by X-ray diffraction (XRD) technique using Cu (K_α = 1.54 Å) radiations in the range of 20–80° (2θ) with 0.0120° step size on *PANalytical Xpert-Pro* diffractometer. Transmission electron microscopy (TEM) was performed on *JEOL 2100F* (200 kV) to understand the morphology of the prepared sample. The absorption spectra and emission spectra of the prepared sample were recorded by using Double beam UV–Visible spectrophotometer (*Hitachi U-3900H*) and Photoluminescence (PL) spectrometer (*G9800A*). Further, structural and chemical composition of the prepared sample were observed with the help of FTIR and X-ray photo spectroscopy (XPS). The presence of various functional groups and vibrational modes were observed using FTIR (*Perkin Elmer-Spectrum-RF-1*) in the range 400–2000 cm^{-1} at room temperature. XPS data was obtained on *PHI 5000 Versa Prob II, FEI Inc.* with the help of Al Kα radiation (1486.7 eV, C1s; 284.4 eV as calibration binding energy).

2.2. Adsorption and photocatalytic test

To understand the adsorption and photocatalytic performance of the prepared MnO_2 sample, methylene blue (MB) dye and N-phenol were taken as model organic compounds. For both the studies, 100 ml of 2.0 mg/L solution of both compounds was prepared and 10 mg of prepared MnO_2 catalyst was added to it. The prepared mixture was kept in the dark chamber for 30 min. An aliquot of 3 ml was extracted at an interval of 2 min and measure the absorption at 664 and 400 nm (characteristic absorption wavelength of MB dye and N-phenol, respectively) to calculate the amount of adsorbed dye on the surface of prepared catalyst. Thereafter, the solution was exposed to visible irradiation under household CFL lamp (85 W; 8900 lx) for 120 min in which sampling was carried out at an interval of 30 min and measured the absorption at same wavelengths. Further, kinetic studies for the photochemical reactions has been carried out based on our previous report [12].

2.3. Electrocatalytic test

The electrochemical activity of the as-prepared samples was investigated by *Bio-logic EC Lab SP300* standard setup. In the three-electrode system platinum was used as the counter electrode, saturated calomel electrode (SCE) as the reference electrode and the working electrode was prepared manually. For fabrication of the working electrode, 1 mg of the sample was dispersed in 250 µL of ethanol and the solution was sonicated for 25 min to achieve uniform dispersion of particles. The top surface of glassy carbon electrode (GCE) having a surface area of 0.070 cm^2 was drop-casted by10 µL of the above dispersed solution. A single drop of Nafion 117 solution (Sigma Aldrich) from 10 µL was put onto the GCE top and was dried overnight.

The three-electrodes were dipped in the working cell filled with basic electrolyte 0.5 M KOH. All the measurements were done for the reversible hydrogen electrode (RHE). The SCE measurements were converted to RHE by using eq. (1) [42]

$$\boldsymbol{RHE} = \boldsymbol{V_{SCE}} + 0.059 \times \boldsymbol{pH} + 0.243 \quad (1)$$

where V_{SCE} is the voltage with respect to SCE.

3. Results and discussion

3.1. XRD, UV–visible spectroscopy, FTIR and TEM microscopy

Fig. 1a represents the XRD pattern of synthesized MnO_2 sample, which exhibit nano-scale crystallites corresponding to broad peaks at 37° and 66° as reported by different research groups [26,27,41,43,44]. The formation of MnO_2 has also been observed with optical absorbance spectroscopy in which the calculated optical band gap was calculated to be 2.53 eV as shown in the inset of Fig. 1b [16]. Further, FTIR spectra (Fig. 1c) of as-synthesized MnO_2 sample confirmed the formation of MnO_2 where the broad transmittance bands were observed at 500–650, 1000–1100, 1346 and 1413 cm^{-1} are corresponding to the O−Mn−O, Mn−O (MnO_6 octahedra), Mn−OH, Mn=O and bending of Mn−OH, respectively [45–48]. Further, broad transmittance band around ~1585 cm^{-1} is associated to the weak stretching of OH bond [45]. Moreover, TEM micrographs have also supported the XRD results, which show a very large network like morphology of prepared sample as shown in Fig. 2. It suggests that the open porous network like

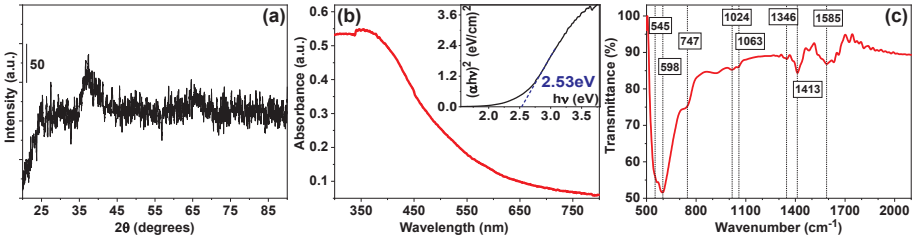

Fig. 1. (a) XRD, (b) optical absorption spectra (inset) and (c) FTIR spectra of nanocrystalline MnO_2.

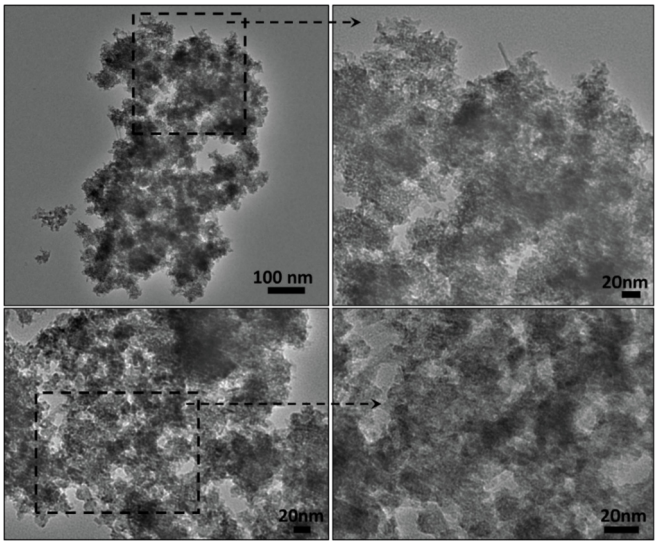

Fig. 2. TEM micrographs of MnO_2 nanopowder suggesting the open porous network.

structure consisting of very small crystallites as shown in Fig. 3 [27]. Further, SAED pattern exhibited diffused ring like pattern which is in tune to the peak observed at ~37° in XRD pattern [41]. HR-TEM images at different regions with lattice fringing have confirmed the formation of nanocrystalline MnO_2 as shown in Fig. 3a–f.

3.2. XPS spectroscopy

In order to estimates the chemical composition of synthesized MnO_2 samples on the surface, X-ray photoelectron spectroscopy (XPS) analysis was done. Fig. 4a confirmed the presence of Mn (2p, 3s and 3p) and O (1s) on the surface of the catalyst while, presence of carbon (1s) can be associated to the calibration element or adhesive tape. HR-XPS spectra of Mn2p (Fig. 4b) revealed the presence of multiple oxidation states of Mn in the form of Mn^{2+}, Mn^{3+} and Mn^{4+} associated to 641.1, 642.2 and 644.3 eV respectively [49,50]. The volume fraction of all these three oxidation states follows 33.65, 44.13 and 22.22%, respectively. Moreover, HR-XPS spectra of O1s (Fig. 4c) suggested the presence of lattice oxygen (529.3 eV; 28.18%) along with surface oxygen species (O_2^-, O^- *and* O_2^{2-}; 531.9 eV; 29.17%) and adsorbed water (532.5 eV; 42.64%) [50]. The higher volume fraction of adsorbed species than lattice oxygen may be associated to the porous network like morphology of the synthesized catalyst. Further, the valence band spectrum of the catalyst suggested the potential of the highest level of valence band (VBE), as −0.17 eV as shown in Fig. 4d. Hence, the position of power level of conduction band (CBE) can be calculated as 2.36 eV ($CBE = E_g + VBE$). The presence of various surface functional groups is responsible for the catalytic reactions that is discussed in subsequent sections 3.3 and 3.4.

3.3. Adsorption and photodegradation study

For the adsorption and photocatalytic study of synthesized MnO_2 nanopowder, two different organic effluents have been used (MB dye and N-phenol) which have excitation in visible and UV region (respectively) to eliminate the effect of dye sensitization. Prior to irradiation, photocatalyst was dispersed in the both solutions for 30 min and the decrease in the concentration of solution obtained during the establishment of adsorption-desorption equilibrium is shown in Fig. 5a. Fig. 5a suggest the saturation of adsorption of molecules (MB and N-phenol) on the surface of catalyst and Fig. 5b and c represent the pseudo first and second order reaction kinetics for MB dye and N-phenol. Based on the quality of fitting (R^2), it has been observed that the adsorption of MB dye and N-phenol followed pseudo second order kinetics i.e. chemisorption at the rate of 0.0432 and 0.4792 min^{-1} (respectively) as shown in Fig. 5c. The observed relationship might be asserted to the attachment of oxygen species (O_2^-, O^- *and* O_2^{2-}) to the effluent molecule as observed in XPS spectra (Fig. 4c).

As a result of adsorption study, 96.2% and 86.9% adsorption of MB dye and N-phenol (respectively) has been observed on the surface of synthesized MnO_2 nanopowder. Thereafter, solutions were irradiated under CFL lamp and variation in their concentration was measured and significant degradation (49%; MB dye and 42%; N-phenol) was observed in 120 min as shown in Fig. 6a. The observed discoloration trend confirmed the photodegradation of both the organic effluents under visible radiations rather dye sensitization [51]. Further, the rate kinetics suggested the simultaneous action of pseudo first and second order law during the photodegradation of MB dye and N-phenol as shown in Fig. 6b and c, respectively [12].

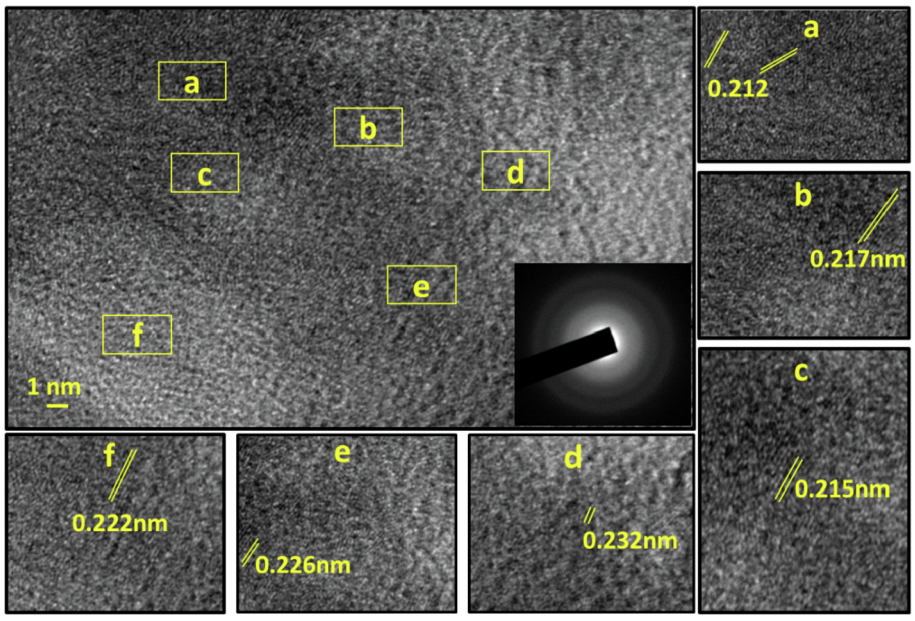

Fig. 3. HR-TEM micrograph of MnO_2 nanopowder suggesting the presence of nano-crystallites embedded in an amorphous network (SAED pattern).

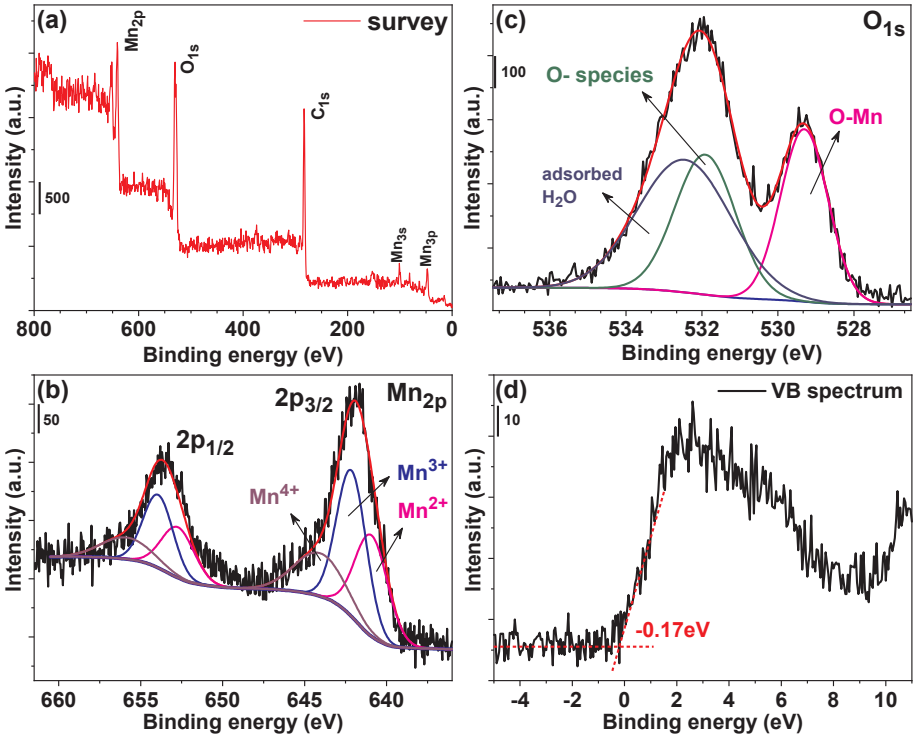

Fig. 4. XPS spectra of prepared MnO_2 sample. Survey spectrum (a); HR-XPS spectra of Mn_{2p} (b), O_{1s} (c) and valence band spectra (d).

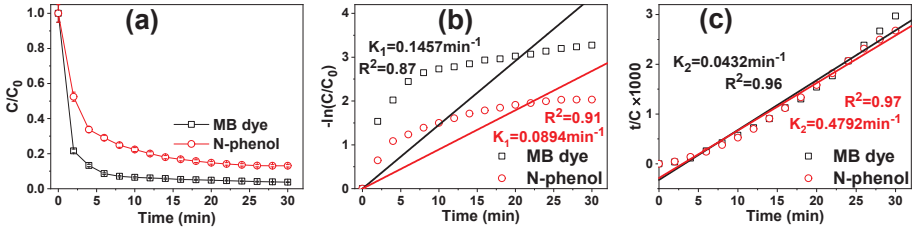

Fig. 5. Adsorption kinetics of MB dye and N-phenol (a) C/C_0 vs. time; (b) pseudo first order and (c) pseudo second order reaction kinetics.

Fig. 7 represents the schematic mechanism responsible for the photodegradation of both organic compounds. Photo excited electrons-holes participate in the formation of superoxide onion radical ($O_2^{\cdot-}$) and hydroxyl radical ($\cdot OH$) at conduction and valance band, respectively as mentioned below:

$$MnO_2 + photon \rightarrow MnO_2 + h^+ + e^- \quad (2)$$

$$OH^- + h^+ \rightarrow \cdot OH \quad (3)$$

$$O_2^{\cdot} + e^- \rightarrow O_2^{\cdot-} \quad (4)$$

$$O_2^{\cdot-} + H_2O \rightarrow \cdot OH + OH^- \quad (5)$$

$$MnO_2 + MB^* \rightarrow MB^{\cdot+} + MnO_2^- \quad (6)$$

$$MnO_2^- + O_2 \rightarrow MnO_2 + O_2^{\cdot-} \quad (7)$$

$$MnO_2^- + O_2^{\cdot-} + h^+ \rightarrow MnO_2 + HO_2^- \quad (8)$$

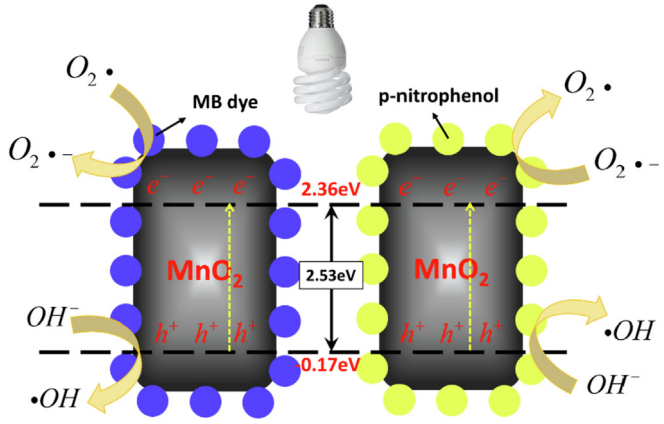

Fig. 7. Schematic representation of photodegradation mechanism with MnO_2.

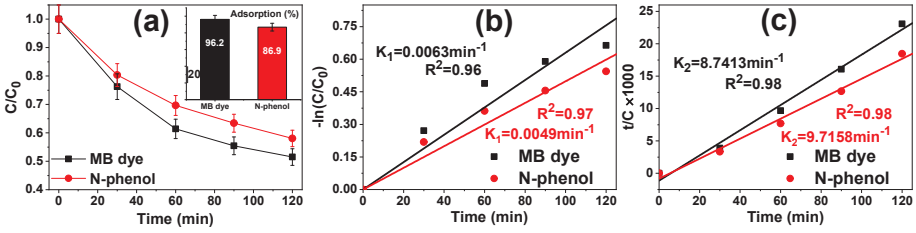

Fig. 6. Photodegradation kinetics of MB dye and N-phenol (a) C/C_0 vs. time with adsorption of adsorbate on the synthesized catalyst (inset); (b) pseudo first order and (c) pseudo second order reaction kinetics.

$$HO_2^- + h^+ \rightarrow H_2O_2 \quad (9)$$

$$H_2O_2 + e^- \rightarrow \cdot OH + OH^- \quad (10)$$

$$Mn^{4+} \overset{e^-}{\leftrightarrow} Mn^{3+} \overset{e^-}{\leftrightarrow} Mn^{2+} \quad (11)$$

$$Mn^{2+} \overset{h^+}{\leftrightarrow} Mn^{3+} \overset{h^+}{\leftrightarrow} Mn^{4+} \quad (12)$$

Direct photoexcitation of MnO_2 exhibited the degradation of both compounds following equations (2)–(5) through the transfer of charge carriers from catalyst to dye molecules resulting the formation of different radicals. While, in the case of MB dye, indirect excitation of the catalyst is also possible, which can be expressed with the help of equation (6)–(10), resulting in the photo-oxidation of MB dye [52]. Moreover, the presence of multiple oxidation states of Mn (as observed in XPS results) would further promote the photochemical reaction as charge trap center by delaying the recombination [15]. Thereafter, these reactive radicals would decompose the absorbed molecules during the visible exposure resulting either lighter non-toxic organic molecules or $CO_2 + H_2O$.

3.4. Electrocatalytic study

The capacitive performance of MnO_2 nanostructures is evaluated by CV analysis. Fig. 8a shows the CV curves of MnO_2 nanostructures at multiple scan rate of 20–200 $mVsec^{-1}$. The rectangular loop in the potential window (0.77–0.97 V) along the current-potential axis without any redox peak, indicates the non-faradic capacitive behavior synthesized nano structures [53]. The calculated electric double layer capacitance (EDLC, C_{dl}; Fig. 8b) and specific capacitance (SC) is 7.9 $mFcm^{-2}$ and 13.8 Fg^{-1}, respectively. The C_{dl} value exhibited the large electrochemically active surface area of these synthesized MnO_2 nanostructures and revealed the enhanced capacitance in basic electrolyte. The enhancement in the charge storage capacity is mainly due to the smaller crystallite size as determined from TEM. The porous network exhibited by TEM also improves the charge kinetic rate on the surface [44]. The higher C_{dl} and SC of the synthesized MnO_2 nanostructures shows the enhancement in charge storage capacity with respect to the reported and developed capacitor materials [42,54,55]. Furthermore, MnO_2 nanostructures have excellent long duration cycle stability for 2000 CV cycles as shown in Fig. 8c. The only distortion observed is with respect to first CV cycle, which remains constant thereafter for all the corresponding cycles. The specific capacitance retention (%) with respect to CV cycle number is shown in Fig. 8d. The curve reveals the only loss of retention by 13% for 2000 cycles, which is higher than the other synthesized capacitance electrode materials [29,41,42,54,56,57]. The higher stability of the synthesized MnO_2 structure might correspond to its poor crystallinity and unique morphological characteristics which inhibit the poisoning of cathode during charging and discharging. The EDLC utilizes surface characteristics for reversible ion adsorption at the surface or inside pores to improve the capacitance performance as well as retention to store charge. The mechanism of energy storage by MnO_2 materials having nearly amorphous nature and showing non redox reversible redox CV curves is generally based on surface adsorption/desorption of H^+ at the surface [55,56,58]. This phenomenon is responsible for the EDLC behavior of synthesized nanostructures, which is in agreement with the CV curve as also predicted by Lukatskaya et al. [59]. The lattice defects introduced during the synthesis due to lattice defects or oxygen vacancies improve the charge storage performance [60]. The results reveal the potential application of synthesized MnO_2 phase for double layer capacitor applications.

To understand the adsorption/desorption kinetics of the synthesized material and its potential use as electrocatalyst for water splitting through hydrogen evolution reaction (HER), the linear sweep voltammetry (LSV) and Tafel analysis studies were done as shown in Fig. 8e and f, respectively. The Tafel slope of 120.7 $mVdec^{-1}$ determines the Volmer reaction as the rate determining step for HER [42,53,54]. Volmer reaction studies also predict the lower adsorption/desorption kinetics of the synthesized MnO_2 due to low crystallinity and uneven wide pore size distribution in porous network. The same mechanism is also responsible for charge storage in low crystalline MnO_2 based capacitors. The surface characteristics need to be modified to enhance the charge transfer kinetics for enhancement in HER and storage ability. The current density value of 30 $mAcm^{-2}$ initially show the higher electron transfer rate of MnO_2 nanostructures. The lower crystallite size and open porous network like morphology enhances the charge transfer rate and improves the current density value in the given voltage. The continuous network like morphology exhibited by synthesized MnO_2 provides more active sites available for the electrocatalytic activity and enhance current density. The stability is an important parameter for the commercial application of the synthesized material for HER. The stability was tested via CV analysis performed in voltage window −0.2 to −0.9 V at a scan rate of 100 $mVsec^{-1}$ for 1000 cycles. The LSV plot performed after 1000 CV cycles shows the loss of current density by ~4% as shown in Fig. 8e. The results predict the synthesized material as potential electrocatalyst for HER in basic electrolyte with higher stability. The stability can be enhanced by changing the oxygen species present on the surface to improve the corrosion resistance of synthesized MnO_2 in basic electrolyte. The higher content of O-species (observed in XPS results) on the surface exhibited the enhanced corrosion resistance and stability. The results reveal the use of synthesized material for charge storage devices and also as the stable electrocatalyst for green/hydrogen energy production.

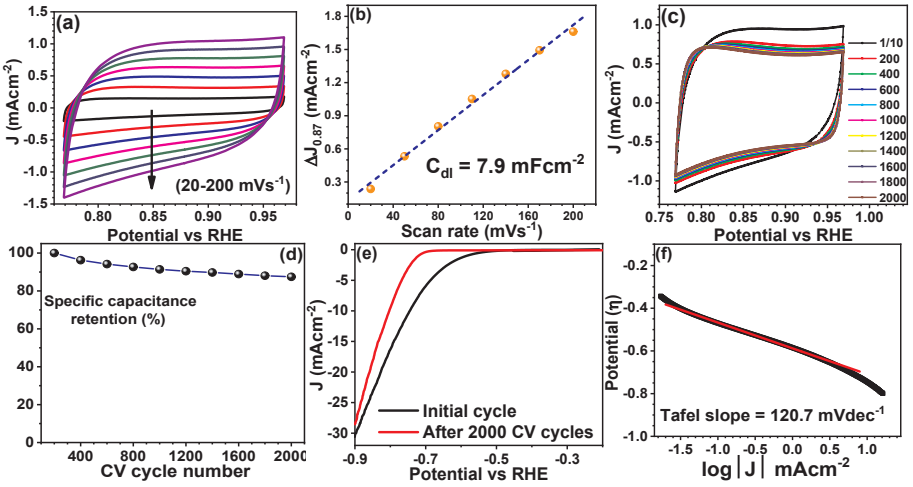

Fig. 8. (a) cyclic voltammetry (CV) curve with variable scan rate; (b) electric double layer capacitance (EDLC); (c) CV plots representing the stability upto 2000 cycles in basic medium; (d) specific capacitance retention vs. number of cycles; (e) linear sweep voltammetry (LSV) in basic medium (0.5 M KOH) and (f) Tarek slope in basic medium for the synthesized MnO_2 nanopowder.

4. Conclusion

MnO_2 nanopowder has been synthesized through a facile single step sonochemical route through the reduction of $KMnO_4$ with PEG. XRD, UV–visible spectroscopy and TEM results confirmed the formation of nanocrystalline network of MnO_2 with ultra-small crystallites (~2–3 nm) having 2.53 eV optical band gap. FTIR spectroscopy suggested the presence of MnO_6 octahedra as basic constituent with different vibrating Mn−O functional groups and XPS confirmed the presence of Mn in multiple oxidation states (2+, 3 + and 4+). Further, adsorption study revealed the adsorption of MB dye and p-nitrophenol has been saturated in 30min with 96 and 86% efficiency (respectively) following chemisorption kinetics. Further, photodegradation of both the molecules under household CFL lamp has been observed with ~50 and ~42% efficiency through the simultaneous physi- and chemisorption kinetics. Electrocatalytic results confirmed the excellent stability of synthesized MnO_2 up to 2000 cycles in alkaline medium (0.5 M KOH) with Volmer reaction as the rate determining step. The potential application of MnO_2 as capacitor with durability and excellent stability for HER widens the research area for the electrocatalytic water splitting.

References

[1] H. Huang, J. Liu, P. Zhang, D. Zhang, F. Gao, Investigation on the simultaneous removal of fluoride, ammonia nitrogen and phosphate from semiconductor wastewater using chemical precipitation, Chem. Eng. J. 307 (2017) 696–706, https://doi.org/10.1016/j.cej.2016.08.134.

[2] V. Colla, T.A. Branca, F. Rosito, C. Lucca, B.P. Vivas, V.M. Delmiro, Sustainable Reverse Osmosis application for wastewater treatment in the steel industry, J. Clean. Prod. 130 (2016) 103–115, https://doi.org/10.1016/j.jclepro.2015.09.025.

[3] C.Y. Teh, P.M. Budiman, K.P.Y. Shak, T.Y. Wu, Recent advancement of coagulation-flocculation and its application in wastewater treatment, Ind. Eng. Chem. Res. 55 (2016) 4363–4389, https://doi.org/10.1021/acs.iecr.5b04703.

[4] S. De Gisi, G. Lofrano, M. Grassi, M. Notarnicola, Characteristics and adsorption capacities of low-cost sorbents for wastewater treatment: a review, Sustain. Mater. Technol. 9 (2016) 10–40, https://doi.org/10.1016/j.susmat.2016.06.002.

[5] M. Mehrjouei, S. Müller, D. Möller, A review on photocatalytic ozonation used for the treatment of water and wastewater, Chem. Eng. J. 263 (2015) 209–219, https://doi.org/10.1016/j.cej.2014.10.112.

[6] Y. Feng, L. Yang, J. Liu, B.E. Logan, Electrochemical technologies for wastewater treatment and resource reclamation, Environ. Sci. Water Res. Technol. 2 (2016) 800–831, https://doi.org/10.1039/c5ew00289c.

[7] S. Dong, J. Feng, M. Fan, Y. Pi, L. Hu, X. Han, M. Liu, J. Sun, J. Sun, Recent developments in heterogeneous photocatalytic water treatment using visible light-responsive photocatalysts: a review, RSC Adv. 5 (2015) 14610–14630, https://doi.org/10.1039/c4ra13734e.

[8] P.A.K. Reddy, P.V.L. Reddy, E. Kwon, K.H. Kim, T. Akter, S. Kalagara, Recent advances in photocatalytic treatment of pollutants in aqueous media, Environ. Int. 91 (2016) 94–103, https://doi.org/10.1016/j.envint.2016.02.012.

[9] J. Xiao, Y. Xie, H. Cao, Organic pollutants removal in wastewater by heterogeneous photocatalytic ozonation, Chemosphere 121 (2015) 1–17, https://doi.org/10.1016/j.chemosphere.2014.10.072.

[10] S. Teixeira, R. Gurke, H. Eckert, K. Kühn, J. Fauler, G. Cuniberti, Photocatalytic degradation of pharmaceuticals present in conventional treated wastewater by nanoparticle suspensions, J. Environ. Chem. Eng. 4 (2016) 287–292, https://doi.org/10.1016/j.jece.2015.10.045.

[11] P. Singla, M. Sharma, O.P. Pandey, K. Singh, Photocatalytic degradation of azo dyes using Zn-doped and undoped TiO2 nanoparticles, Appl. Phys. A. 116 (2014) 371–378, https://doi.org/10.1007/s00339-013-8135-z.

[12] M. Mittal, M. Sharma, O.P. Pandey, UV – visible light induced photocatalytic studies of Cu doped ZnO nanoparticles prepared by co-precipitation method, Sol. Energy 110 (2014) 386–397, https://doi.org/10.1016/j.solener.2014.09.026.

[13] M. Kaur, O.P. Pandey, M. Sharma, Synthesis and characterization of Mn doped ZnCdS core shell nanostructures QDs using a chemical precipitation route, AIP Conf. Proc. 1724 (2016), https://doi.org/10.1063/1.4945177.

[14] J. Kaur, A. Gupta, O.P. Pandey, Photocatalytic study of ZnS-Ag2S nanocomposites-effect of thioglycerol, Sol. Energy 176 (2018) 678–687, https://doi.org/10.1016/j.solener.2018.10.077.

[15] M. Mittal, A. Gupta, O.P. Pandey, Role of oxygen vacancies in Ag/Au doped CeO2 nanoparticles for fast photocatalysis, Sol. Energy 165 (2018) 206–216, https://doi.org/10.1016/j.solener.2018.03.033.

[16] A. Singh Vig, A. Gupta, O.P. Pandey, Efficient photodegradation of methylene blue (MB) under solar radiation by ZrC nanoparticles, Adv. Powder Technol. 29 (2018) 2231–2242, https://doi.org/10.1016/j.apt.2018.06.007.

[17] J.G. Wang, F. Kang, B. Wei, Engineering of MnO2-based nanocomposites for high-performance supercapacitors, Prog. Mater. Sci. 74 (2015) 51–124, https://doi.org/10.1016/j.pmatsci.2015.04.003.

[18] M.A. Barakat, M.H. Ramadan, M.A. Alghamdi, S.S. Algarny, H.L. Woodcock, J.N. Kuhn, Remediation of Cu(II), Ni(II), and Cr(III) ions from simulated wastewater by dendrimer/titania composites, J. Environ. Manag. 117 (2013) 50–57, https://doi.org/10.1016/j.jenvman.2012.12.025.

[19] K.M. Lee, C.W. Lai, K.S. Ngai, J.C. Juan, Recent developments of zinc oxide based photocatalyst in water treatment technology: a review, Water Res. 88 (2016) 428–448, https://doi.org/10.1016/j.watres.2015.09.045.

[20] Z. Dai, X. Yu, C. Huang, M. Li, J. Su, Y. Guo, H. Xu, Q. Ke, Nanocrystalline MnO2 on an activated carbon fiber for catalytic formaldehyde removal, RSC Adv. 6 (2016) 97022–97029, https://doi.org/10.1039/c6ra15463h.

[21] S. Guan, W. Li, J. Ma, Y. Lei, Y. Zhu, Q. Huang, X. Dou, A review of the preparation and applications of MnO2 composites in formaldehyde oxidation, J. Ind. Eng. Chem. 66 (2018) 126–140, https://doi.org/10.1016/j.jiec.2018.05.023.

[22] S. Das, A. Samanta, S. Jana, Light-Assisted synthesis of hierarchical flower-like MnO2Nanocomposites with solar light induced enhanced photocatalytic activity, ACS Sustain. Chem. Eng. 5 (2017) 9086–9094, https://doi.org/10.1021/acssuschemeng.7b02003.

[23] I. Khan, M. Sadiq, I. Khan, K. Saeed, Manganese Dioxide Nanoparticles/Activated Carbon Composite as Efficient UV Manganese Dioxide Nanoparticles/Activated Carbon Composite as Efficient UV and Visible-Light Photocatalyst, (2019), https://doi.org/10.1007/s11356-018-4055-y.

[24] J. Zhao, Z. Tao, J. Liang, J. Chen, Facile synthesis of nanoporous γ-MnO2 structures and their application in rechargeable Li-ion batteries, Cryst. Growth Des. 8 (2008) 2799–2805, https://doi.org/10.1021/cg701044b.

[25] M. Xu, L. Kong, W. Zhou, H. Li, Hydrothermal synthesis and pseudocapacitance properties of α-MnO 2 hollow spheres and hollow urchins, J. Phys. Chem. C 111 (2007) 19141–19147, https://doi.org/10.1021/jp076730b.

[26] Q. Liu, S. Ji, J. Yang, H. Wang, B.G. Pollet, R. Wang, Enhanced cycleability of amorphous MnO2 by covering on α-MnO2 needles in an electrochemical capacitor, Materials (Basel) 10 (2017) 1–10, https://doi.org/10.3390/ma10090988.

[27] H.Q. Wang, G.F. Yang, Q.Y. Li, X.X. Zhong, F.P. Wang, Z.S. Li, Y.H. Li, Porous nano-MnO2: large scale synthesis via a facile quick-redox procedure and application in a supercapacitor, New J. Chem. 35 (2011) 469–475, https://doi.org/10.1039/c0nj00712a.

[28] L. Li, Z.A. Hu, N. An, Y.Y. Yang, Z.M. Li, H.Y. Wu, Facile synthesis of MnO2/CNTs composite for supercapacitor electrodes with long cycle stability, J. Phys. Chem. C 118 (2014) 22865–22872, https://doi.org/10.1021/jp505744p.

[29] Y. Xiong, M. Zhou, H. Chen, L. Feng, Z. Wang, X. Yan, S. Guan, Synthesis of honeycomb MnO2 nanospheres/carbon nanoparticles/graphene composites as electrode materials for supercapacitors, Appl. Surf. Sci. 357 (2015) 1024–1030, https://doi.org/10.1016/j.apsusc.2015.09.111.

[30] Y. Zhao, C.A. Wang, Nano-network MnO2/polyaniline composites with enhanced electrochemical properties for supercapacitors, Mater. Des. 97 (2016) 512–518, https://doi.org/10.1016/j.matdes.2016.02.120.

[31] L. Ma, X. Shen, Z. Ji, G. Zhu, H. Zhou, Ag nanoparticles decorated MnO2/reduced graphene oxide as advanced electrode materials for supercapacitors, Chem. Eng. J. 252 (2014) 95–103, https://doi.org/10.1016/j.cej.2014.04.093.

[32] F. Cheng, Y. Su, J. Liang, Z. Tao, J. Chen, MnO2-based nanostructures as catalysts for electrochemical oxygen reduction in alkaline media, Chem. Mater. 22 (2010) 898–905, https://doi.org/10.1021/cm901698s.

[33] Y.L. Chan, S.Y. Pung, S. Sreekantan, F.Y. Yeoh, Photocatalytic activity of β-MnO2 nanotubes grown on PET fibre under visible light irradiation, J. Exp. Nanosci. 11 (2016) 603–618, https://doi.org/10.1080/17458080.2015.1102342.

[34] A. Iyer, H. Galindo, S. Sithambaram, C. King'ondu, C.H. Chen, S.L. Suib, Nanoscale manganese oxide octahedral molecular sieves (OMS-2) as efficient photocatalysts in 2-propanol oxidation, Appl. Catal. A Gen. 375 (2010) 295–302, https://doi.org/10.1016/j.apcata.2010.01.012.

[35] M. Sharma, D. Choudhury, S. Hazra, S. Basu, Effective removal of metal ions from aqueous solution by mesoporous MnO2 and TiO2 monoliths: kinetic and equilibrium modelling, J. Alloy. Comp. 720 (2017) 221–229, https://doi.org/10.1016/j.jallcom.2017.05.260.

[36] M. Gheju, I. Balcu, G. Mosoarca, Removal of Cr(VI) from aqueous solutions by adsorption on MnO2, J. Hazard Mater. 310 (2016) 270–277, https://doi.org/10.1016/j.jhazmat.2016.02.042.

[37] S.T. El-Wakeel, R.S. El-Tawil, H.A.M. Abuzeid, A.E. Abdel-Ghany, A.M. Hashem, Synthesis and structural properties of MnO2 as adsorbent for the removal of lead (Pb2+) from aqueous solution, J. Taiwan Inst. Chem. Eng. 72 (2017) 95–103, https://doi.org/10.1016/j.jtice.2017.01.008.

[38] M.X. Zhu, Z. Wang, S.H. Xu, T. Li, Decolorization of methylene blue by δ-MnO2-coated montmorillonite complexes: emphasizing redox reactivity of Mn-oxide coatings, J. Hazard Mater. 181 (2010) 57–64, https://doi.org/10.1016/j.jhazmat.2010.04.080.

[39] Y. He, D. Bin Jiang, J. Chen, D.Y. Jiang, Y.X. Zhang, Synthesis of MnO2 nanosheets on montmorillonite for oxidative degradation and adsorption of methylene blue, J. Colloid Interface Sci. 510 (2018) 207–220, https://doi.org/10.1016/j.jcis.2017.09.066.

[40] A. Gagrani, J. Zhou, T. Tsuzuki, Solvent free mechanochemical synthesis of MnO2for the efficient degradation of Rhodamine-B, Ceram. Int. 44 (2018) 4694–4698, https://doi.org/10.1016/j.ceramint.2017.12.050.

[41] B. Gnana Sundara Raj, A.M. Asiri, A.H. Qusti, J.J. Wu, S. Anandan, Sonochemically synthesized MnO2 nanoparticles as electrode material for supercapacitors, Ultrason. Sonochem. 21 (2014) 1933–1938, https://doi.org/10.1016/j.ultsonch.2013.11.018.

[42] N. Kaur, R.A. Mir, O.P. Pandey, Electrochemical and optical studies of facile synthesized molybdenum disulphide (MoS2) nano structures, J. Alloy. Comp. 782 (2019) 119–131, https://doi.org/10.1016/j.jallcom.2018.12.145.

[43] C. Wan, L. Yuan, H. Shen, Effects of electrode mass-loading on the electrochemical properties of porous MnO2 for electrochemical supercapacitor, Int. J. Electrochem. Sci. 9 (2014) 4024–4038.
[44] S. Devaraj, N. Munichandraiah, Effect of crystallographic structure of MnO2 on its electrochemical capacitance properties, J. Phys. Chem. C 112 (2008) 4406–4417, https://doi.org/10.1021/jp7108785.
[45] S.A. Alzahrani, S.A. Al-Thabaiti, W.S. Al-Arjan, M.A. Malik, Z. Khan, Preparation of ultra long α-MnO2 and Ag@MnO2 nanoparticles by seedless approach and their photocatalytic performance, J. Mol. Struct. 1137 (2017) 495–505, https://doi.org/10.1016/j.molstruc.2017.02.068.
[46] K.S. Prasad, A. Patra, Green synthesis of MnO2 nanorods using Phyllanthus amarus plant extract and their fluorescence studies, Green Process. Synth. 6 (2017) 549–554, https://doi.org/10.1515/gps-2016-0166.
[47] X. Zhang, M. He, P. He, C. Li, H. Liu, X. Zhang, Y. Ma, Ultrafine nano-network structured bacterial cellulose as reductant and bridging ligands to fabricate ultra-thin K-birnessite type MnO2 nanosheets for supercapacitors, Appl. Surf. Sci. 433 (2018) 419–427, https://doi.org/10.1016/j.apsusc.2017.10.053.
[48] S. Saha, A. Pal, Microporous assembly of MnO2 nanosheets for malachite green degradation, Separ. Purif. Technol. 134 (2014) 26–36, https://doi.org/10.1016/j.seppur.2014.07.021.
[49] B. Liu, I.M. Mosa, W. Song, H. Zheng, C.-H. Kuo, J.F. Rusling, S.L. Suib, J. He, Unconventional structural and morphological transitions of nanosheets, nanoflakes and nanorods of AuNP@MnO2, J. Mater. Chem. A. 4 (2016) 6447–6455, https://doi.org/10.1039/C6TA02017H.
[50] W. Tang, X. Wu, D. Li, Z. Wang, G. LIu, H. Liu, Y. Chen, Oxalate route for promoting activity of manganese oxide catalysts in total VOCs' oxidation : effect of calcination temperature and preparation method, J. Mater. Chem. A. 2 (2014) 2544–2554, https://doi.org/10.1039/c3ta13847j.
[51] J. Diaz-Angulo, I. Gomez-Bonilla, C. Jimenez-Tohapanta, M. Mueses, M. Pinzon, F. Machuca-Martinez, Visible-light activation of TiO2 by dye-sensitization for degradation of pharmaceutical compounds, Photochem. Photobiol. Sci. (2019), https://doi.org/10.1039/C8PP00270C.
[52] P. Wilhelm, D. Stephan, Photodegradation of rhodamine B in aqueous solution via SiO2@TiO2 nano-spheres, J. Photochem. Photobiol. A Chem. 185 (2007) 19–25, https://doi.org/10.1016/j.jphotochem.2006.05.003.
[53] R.A. Mir, O.P. Pandey, Influence of graphitic/amorphous coated carbon on HER activity of low temperature synthesized β-Mo2C@C nanocomposites, Chem. Eng. J. 348 (2018) 1037–1048 https://doi.org/10.1016/j.cej.2018.05.041.
[54] L.K. Brar, A. Gupta, O.P. Pandey, Influence of carbon content of nano-TaC powders on the electrocatalytic and photocatalytic properties, Catal. Today 325 (2018) 98–108, https://doi.org/10.1016/j.cattod.2018.07.053.
[55] S.K. Meher, G.R. Rao, Enhanced activity of microwave synthesized hierarchical MnO2 for high performance supercapacitor applications, J. Power Sources 215 (2012) 317–328, https://doi.org/10.1016/j.jpowsour.2012.04.104.
[56] Y. Zhang, C. Sun, P. Lu, K. Li, S. Song, D. Xue, Crystallization design of MnO2 towards better supercapacitance, CrystEngComm 14 (2012) 5892–5897, https://doi.org/10.1039/c2ce25610j.
[57] B. Zhao, M. Lu, Z. Wang, Z. Jiao, P. Hu, Q. Gao, Y. Jiang, L. Cheng, Self-assembly of ultrathin MnO2/graphene with three-dimension hierarchical structure by ultrasonic-assisted co-precipitation method, J. Alloy. Comp. 663 (2016) 180–186, https://doi.org/10.1016/j.jallcom.2015.12.018.
[58] X. Zhao, Y. Hou, Y. Wang, L. Yang, L. Zhu, R. Cao, Z. Sha, Prepared MnO2 with different crystal forms as electrode materials for supercapacitors: experimental research from hydrothermal crystallization process to electrochemical performances, RSC Adv. 7 (2017) 40286–40294, https://doi.org/10.1039/c7ra06369e.
[59] M.R. Lukatskaya, B. Dunn, Y. Gogotsi, Multidimensional materials and device architectures for future hybrid energy storage, Nat. Commun. 7 (2016), https://doi.org/10.1038/ncomms12647.
[60] M.-K. Song, S. Cheng, H. CHen, W. Qin, K.-W. Nam, S. Xu, Z.-Q. Yang, A. Bongiorno, J. Lee, J. Bai, T.A. Tyson, J. Cho, M. Liu, Anomalous pseudocapacitive behavior of a nanostructured, mixed- valent manganese oxide film for electrical energy storage, Nano Lett. 12 (2018) 3483–3490, https://doi.org/10.1021/nl300984y.

turnitin Turnitin Originality Report

kajal-thesis by Kajal Rajrana

From MSc Thesis 2019 (MSc Thesis 2019)

- Processed on 12-Jun-2019 21:55 +0530
- ID: 1142962387
- Word Count: 12802

Similarity Index
15%
Similarity by Source

Internet Sources:
5%
Publications:
8%
Student Papers:
10%

sources:
1

1% match (student papers from 16-Jul-2018)

Class: MSc Thesis 2018
Assignment: MSc Thesis 2018
Paper ID: 982814956
2

1% match (publications)

Rasyidah Alrozi, Norashikin Ahmad Zamanhuri, Mohamed Syazwan Osman. "Removal of methylene blue from aqueous solution by adsorption onto NaOH-treated rambutan peel", 2012 IEEE Business, Engineering & Industrial Applications Colloquium (BEIAC), 2012
3

1% match (student papers from 16-Jul-2017)

Class: MSc Thesis 2017
Assignment: MSc Thesis 2017
Paper ID: 831095694
4

1% match (Internet from 17-Feb-2019)

https://epdf.tips/recent-progress-in-mesostructured-materials-volume-165-proceedings-of-the-5th-in.html
5

< 1% match (Internet from 05-Mar-2014)

http://www.faqs.org/patents/app/20100192253